

## University of Southampton Research Repository

Copyright © and Moral Rights for this thesis and, where applicable, any accompanying data are retained by the author and/or other copyright owners. A copy can be downloaded for personal non-commercial research or study, without prior permission or charge. This thesis and the accompanying data cannot be reproduced or quoted extensively from without first obtaining permission in writing from the copyright holder/s. The content of the thesis and accompanying research data (where applicable) must not be changed in any way or sold commercially in any format or medium without the formal permission of the copyright holder/s.

When referring to this thesis and any accompanying data, full bibliographic details must be given, e.g.

Thesis: Author (Year of Submission) "Full thesis title", University of Southampton, name of the University Faculty or School or Department, PhD Thesis, pagination.

Data: Author (Year) Title. URI [dataset]

**UNIVERSITY OF SOUTHAMPTON**

FACULTY OF ENGINEERING AND ENVIRONMENT

INSTITUTE OF SOUND AND VIBRATION RESEARCH

Signal Processing and Controls Group

**Nonlinear damping in energy harvesters**

by

**Luigi Simeone**

Thesis for the degree of Doctor of Philosophy

March 2017

Supervisors:

Dr M. Ghandchi Tehrani

Prof S. Elliott

**UNIVERSITY OF SOUTHAMPTON**

# **ABSTRACT**

**FACULTY OF ENGINEERING AND ENVIRONMENT**

Institute of Sound and Vibration Research

**Thesis for the degree of Doctor of Philosophy**

## **NONLINEAR DAMPING IN ENERGY HARVESTERS**

Luigi Simeone

Energy harvesting from ambient vibration has become an attractive topic in the recent years. Initial studies aimed to maximise the performance of small linear device for different excitation scenarios. These devices were assumed to be located in hostile and inaccessible environments and be able to provide energy for low powered sensors. Due to the limited size of the energy harvesters, however, the amount of power produced was small.

More recently, many researchers have considered using nonlinear stiffness to improve the performance of these devices. This thesis, however, focuses on the use of nonlinear damping in energy harvesters. Nonlinear damping may be unwanted and introduced as the mechanism of the harvester, but can also be deliberately introduced to improve the dynamic range of the harvester.

Typically ambient vibration generates a relative displacement between the suspended mass and the base in an energy harvester, which induces an electromotive force (EMF) in a circuit that is used to harvest electrical energy. It is possible to introduce nonlinear mechanical damping by having a circuit with a nonlinear resistance. Specifically, a load, in which the current is a third-power function of the voltage is compared with an equivalent linear load for three kinds of excitation such as harmonic, random white noise and random bandlimited noise. According to the numerical and analytical results, the cubic load provides more harvested power at resonance at low levels when compared to an equivalent linear load at the same level of excitation. As the frequency bandwidth of a random excitation becomes wider, to the limit of white noise, as the power generated by the cubic converges to the linear case. Electromagnetic transducer energy harvesters usually adopt a conversion mechanism of motion, such as ball screw or rack and pinion, which introduce a source of loss such as friction. Static friction is then added to the model and this is shown to affect the harvested power at low input levels.

Another proposed strategy consists of adjusting the electric load according to the input level, which can also enlarge the dynamic range of performance of energy harvested compared to a device with constant load.

To demonstrate the effectiveness of the level-dependent load, an energy harvesting device was designed and manufactured, which comprised of an oscillating beam sprung to the base, and attached to a generator. Across the terminals of the generator, an electric resistance is mounted and the voltage measured is used to compute the harvested power.

Experiments are conducted by exciting the harvested with a harmonic input at resonance via a shaker. A level-dependent load and a constant load were separately tested; with results that are in good agreement with the simulations, it is shown that by adjusting the load according to the input level, the harvested power is increased compared to a linear constant load.

*An expert is a person who has made all the mistakes that can be made in a very narrow field. (Niels Bohr)*

*If you want to find the secrets of the universe, think in terms of energy, frequency and vibration. (Nikola Tesla)*



# Table of Contents

Table of Contents .....	i
List of Tables.....	iv
List of Figures .....	v
DECLARATION OF AUTHORSHIP .....	xiii
Acknowledgements .....	xiv
Definitions and Abbreviations .....	xv
Chapter 1: Introduction.....	1
<b>1.1 Motivation.....</b>	<b>1</b>
<b>1.2 Novel contributions.....</b>	<b>2</b>
<b>1.3 Structure of the thesis.....</b>	<b>2</b>
Chapter 2: Literature review .....	4
<b>2.1 Introduction.....</b>	<b>4</b>
<b>2.2 Types of energy harvesting .....</b>	<b>4</b>
<b>2.3 Vibrating energy harvesting .....</b>	<b>5</b>
<b>2.3.1 Piezoelectric harvesters .....</b>	<b>5</b>
<b>2.3.2 Electrostatic harvesters .....</b>	<b>5</b>
<b>2.3.3 Electromagnetic harvesters.....</b>	<b>5</b>
<b>2.4 Linear vibrating energy harvesting.....</b>	<b>5</b>
<b>2.5 Nonlinear vibrating energy harvesting .....</b>	<b>9</b>
<b>2.5.1 Energy harvesting with nonlinear stiffness .....</b>	<b>12</b>
<b>2.5.2 Energy harvesting with nonlinear damping.....</b>	<b>14</b>
<b>2.5.3 Random excitation .....</b>	<b>17</b>
<b>2.6 Application of electromagnetic harvesting to marine environment.....</b>	<b>19</b>
<b>2.7 Summary.....</b>	<b>21</b>
Chapter 3: Nonlinear damping in harmonically-excited energy harvesting device ..	22
<b>3.1 Introduction.....</b>	<b>22</b>
<b>3.2 Electromechanical model .....</b>	<b>22</b>
<b>3.3 Harmonic balance method .....</b>	<b>24</b>
<b>3.4 Equivalent linearisation .....</b>	<b>26</b>
<b>3.5 Optimum load resistance.....</b>	<b>32</b>

3.6	Benefit of the cubic load resistance .....	33
3.7	Effect of parasitic friction .....	36
3.8	An alternative approach: the level-dependent load .....	39
3.9	Summary .....	43
Chapter 4: Nonlinear damping in randomly-excited energy harvesting device.....		44
4.1	Introduction .....	44
4.2	Theory of random processes.....	44
4.3	Statistical moments.....	45
4.4	Gaussian white noise .....	47
4.5	Equivalent linearization method .....	48
4.6	Constraint on the probability of the response .....	53
4.7	Upper bound and optimum load on the harvested power .....	60
4.8	Variation of the input level: level curves .....	62
4.9	Ambient excitation: Gaussian coloured noise .....	65
4.10	Numerical linearisation.....	67
4.11	Variation of the input level: level curve .....	70
4.12	An alternative approach: the level-dependent load .....	72
4.13	Summary .....	74
Chapter 5: Design of an electromagnetic transducer energy harvester .....		75
5.1	Introduction .....	75
5.2	Ball screw based energy harvesting device .....	75
5.3	System dynamics.....	82
5.4	Design process .....	85
5.4.1	Characteristics of the excitation.....	85
5.4.2	Mechanical damping of gearbox and generator .....	86
5.4.3	Analytical parametrical analysis.....	89
5.5	Manufacturing process .....	94
5.6	Optimum load of the harvesting device.....	96
5.7	Summary .....	100
Chapter 6: Experimental tests on the energy harvesting device .....		101
6.1	Introduction .....	101
6.2	Experimental set up.....	101



<b>6.3</b>	<b>Detection of nonlinearity in the open circuit .....</b>	<b>105</b>
<b>6.4</b>	<b>Electrical coupling: optimum load .....</b>	<b>107</b>
<b>6.5</b>	<b>Variation of the input level.....</b>	<b>112</b>
<b>6.6</b>	<b>Maximisation of the harvested power via variable shunt load .....</b>	<b>114</b>
<b>6.7</b>	<b>Summary .....</b>	<b>117</b>
Chapter 7:	Conclusions and future work .....	118
<b>7.1</b>	<b>Conclusions.....</b>	<b>118</b>
<b>7.2</b>	<b>Suggestions for future works .....</b>	<b>120</b>
<b>7.2.1</b>	<b>Modelling .....</b>	<b>120</b>
<b>7.2.2</b>	<b>Experiments.....</b>	<b>121</b>
Publications .....		121
Appendix I – Variance of linear systems (Lyapunov equation) .....		123
Appendix II – Gaussian integral .....		124
Appendix III – Equivalent non-linearisation.....		125
Appendix III – Drawings .....		128
Appendix IV – Generator and gearbox .....		133
List of References .....		135

# List of Tables

Table 1: Harvested power density for different applications (originally published in [8]) .....	4
Table 2: Parameters of the equivalent linear energy harvester .....	27
Table 3: Parameters of the energy harvester .....	54
Table 4: Parameters of the second order filter .....	66
Table 5: Equivalent load as a function of the filter damping ratio .....	67
Table 6: Input parameters of the ball screw harvester .....	78
Table 7: Input parameters .....	90
Table 8: Lower and upper bounds of the variable parameters .....	90
Table 9: Results of the parametrical analysis for different 'Case' .....	92
Table 10: Static and dynamic deflection for different 'Case' .....	92
Table 11: Lee Spring specifications .....	93
Table 12: Analytical and manufacturing set of parameters .....	94
Table 13: Equipment used for the measurements .....	101
Table 14: Electrical quantities for the three operative conditions .....	105

# List of Figures

Figure 1: Schematic diagram of the generator (originally published in [20]).....	6
Figure 2: Schematic diagram of a linear (left) and a rotational (right) energy harvesting system (originally published in [26]).....	8
Figure 3: Example of fixed-point solution.....	9
Figure 4: Stable limit cycle of Van der Pol's equation.....	10
Figure 5: Chaotic attractor of Duffing equation (originally published in [29]) .....	10
Figure 6: Example of asymptotically stable (left), stable (centred), unstable (right) systems .....	11
Figure 7: Bifurcation diagram - the system parameter $r$ influences the attractor $x$ .....	11
Figure 8: Example of frequency response function of a Duffing oscillator with hardening spring - increasing the amplitude of the input force the nonlinear behaviour is stronger	12
Figure 9: Bistable magnetic repulsion harvester (a), magnetic attraction harvester (b), buckled beam harvester (c), spring force potential (d) – $r$ is the tuning parameter and $\delta$ is the ratio between the nonlinear and the linear stiffness (originally published in [36]) .....	13
Figure 10: Cantilever beam with parametric stiffness (originally published in [38]) .....	14
Figure 11: Single degree-of-freedom, base excited, energy harvesting system with nonlinear damper and an enclosure that restricts the maximum throw (originally published in [39]) .....	15
Figure 12: Relative displacement (left) and harvested power (right) for the linear system and nonlinear system with cubic damping, together with the theoretical limit of a highly nonlinear system, the solid line for the nonlinear case is calculated using the harmonic balance method and the dots are the results from time domain simulations (originally published in [39]).....	16
Figure 13: Passive, optimised and arbitrary harvester with the same transmissibility at resonance: average power (left) and relative transmissibility (right), (originally published in [40]) .....	17
Figure 14: Power absorbed as a function of the cut off frequency of the excitation. The various curves correspond to different configurations of the damper and the spring: (a) nonlinear spring and linear damper, (b) nonlinear spring and nonlinear damper,	

(c) linear spring and linear damper, (d) linear spring and nonlinear damper.	
Dashed line: upper bound, (originally published in [41]) .....	18
Figure 15: Photographs showing the testing configuration: (a) compressor base, (b) fan belt cage, (c) and (d) accelerometer (small black square) and Faraday cage containing the energy harvester (rectangular box) mounted for testing. (e) Faraday cage with lid removed to expose contents .....	19
Figure 16: Pierson-Moskowitz spectrum (originally published in [39]) .....	20
Figure 17: Schematic of the electromagnetic-transducer energy harvester – the mechanical system on the right is coupled with an electric circuitry on the left by means a generator .....	23
Figure 18: Examples of the dissipating (left) and harvesting force (right) for $c_m=1Ns/m$ , $f_s = 1N$ , $R_{nl}=1.4V^3/A$ .....	24
Figure 19: Discriminant of the cubic equation as a function of the frequency - one real solution and two complex conjugate solutions are obtained.....	29
Figure 20: Relative transmissibility as a function of the frequency for linear (solid black line) and cubic (dash black line) energy harvesters where $m=1kg$ , $k=4\pi^2$ , $c_m=0.2Ns/m$ , $R_{l,eq}=0.185Ns/m$ , $R_{nl}=1.37V^3/A$ , $Y_{max}=0.246m$ – dashed dotted line with star markers is referred to the analytical solution obtained by the harmonic balance method.....	29
Figure 21: FFT of the relative displacement at resonance for $Y=Y_{max}$ - harmonic balance (solid black line) and ode45 (solid black line with circle markers). It is evident the presence of a third harmonic component in numerical solution (in the zoomed plot), which, instead, is not present in the analytical solution.....	30
Figure 22: Average harvested power as a function of the frequency for linear (solid red line) and cubic (dashed red line) energy harvesters where $m=1kg$ , $k=4\pi^2$ , $c_m=0.2Ns/m$ , $R_{l,eq}=0.185Ns/m$ , $R_{nl}=1.37V^3/A$ , $Y_{max}=0.246m$ – dashed dot line with star markers is referred to the analytical solution obtained by the harmonic balance method.....	31
Figure 23: Average harvested power (solid red line) and relative displacement (solid black line) as a function of the equivalent viscous damping at the natural frequency for $Y=Y_{max}$ - the black dashed dotted line represents the constraint on the maximum displacement $Z_{max}$ while the red dashed dotted line yields the value of the maximum harvested power $P_{max}$ and equivalent damping $R_{l,eq}$ corresponding to	

$Z_{max}$ . As shown, the energy harvester does not work at the optimum conditions  
 $(R_{l,opt}, P_{opt})$  .....33

Figure 24: Relative transmissibility (left) and average harvested power (right) as a function of the frequency for linear (solid line) and cubic (dashed line) energy harvesters where  $m=1kg$ ,  $k=4\pi^2$ ,  $c_m=0.2Ns/m$ ,  $R_{l,eq}=0.185Ns/m$ ,  $R_{nl}=1.37V^3/A$ ,  $Y=0.049m$  – dashed-dotted line with star markers is referred to the analytical solution obtained by the harmonic balance method .....34

Figure 25: Level curves of the relative displacement  $Z$  (left) for linear (solid line) and cubic (dashed line) energy harvesters as a function of the normalised input amplitude  $Y/Y_{max}$  and time history of the relative displacement (right) for  $Y/Y_{max}=0.68$ , where  $m=1kg$ ,  $k=4\pi^2$ ,  $c_m=0.2Ns/m$ ,  $R_{l,eq}=0.185Ns/m$ ,  $R_{nl}=1.37V^3/A$ ,  $Y_{max}=0.246m$  .....35

Figure 26: Level curves of the average harvested power  $P_{ave}$  for linear (solid line) and cubic (dashed line) energy harvesters as a function of the normalised input amplitude  $Y/Y_{max}$  .....36

Figure 27: Equivalent load  $R_{l,eq}$  as a function of the relative displacement  $Z$  at resonance - the black dotted line is referred to the cubic damping, the black solid line with x markers is referred to the combination of cubic and friction .....37

Figure 28: Relative transmissibility (left) and average harvested power (right) as a function of the frequency for linear (solid black line) and cubic (dash black line) energy harvesters where  $m=1kg$ ,  $k=4\pi^2$ ,  $c_m=0.2Ns/m$ ,  $f_s=1N$ ,  $R_{l,eq}=0.185Ns/m$ ,  $R_{nl}=1.37V^3/A$ ,  $Y_{max}=0.246m$  – dashed dotted line with star markers is referred to the analytical solution obtained by the harmonic balance method .....38

Figure 29: Level curves of the relative displacement (left) and average harvested power for (right) linear (solid line) and cubic (dashed line) energy harvesters as a function of the normalised input amplitude  $Y/Y_{max}$  where  $m=1kg$ ,  $k=4\pi^2$ ,  $c_m=0.2Ns/m$ ,  $f_s=1N$ ,  $R_{l,eq}=0.185Ns/m$ ,  $R_{nl}=1.37V^3/A$ ,  $Y_{max}=0.246m$  – dashed-dotted line with star markers is referred to the analytical solution obtained by the harmonic balance method .....39

Figure 30: Shunt load  $R_l$  as a function of the normalised input amplitude  $Y/Y_{max}$  at resonance - the blue dashed line is referred to the linear device, the red solid line is referred to the level-dependent load – the load  $R_l$  reduces linearly with  $Y/Y_{max}$  until the optimum value is achieved .....41

Figure 31: Ratio between the amplitude of the shunt damping force and the amplitude of the relative velocity as a function of the amplitude of the relative velocity .....41

Figure 32: Level curves of the relative displacement $Z$ for linear (solid line), cubic (dashed line) and level-dependent load (dotted line) energy harvesters as a function of the normalised input amplitude $Y/Y_{max}$ where $m=1kg$ , $k=4\pi^2$ , $c_m=0.2Ns/m$ , $R_{l,eq}=0.185Ns/m$ , $R_{nl}=1.37V^3/A$ , $Y_{max}=0.246m$ – dashed-dotted line with star markers is referred to the analytical solution obtained by the harmonic balance method.....	42
Figure 33: Level curves of the average harvested power $P_{ave}$ for linear (solid line), cubic (dashed line) and level-dependent load (dotted line) energy harvesters as a function of the normalised input amplitude $Y/Y_{max}$ .....	42
Figure 34: Example of a <i>PDF</i> of a Gaussian white input.....	47
Figure 35: Examples of <i>PSDs</i> of Gaussian white (solid black line) and coloured (red dash line) noise .....	48
Figure 36: Equivalent linear load as a function of the nonlinear load – analytical result.....	52
Figure 37: Equivalent electric load as a function of the power spectral density of the input acceleration–analytical result .....	52
Figure 38: Displacement obtained from Simulink and $C$ (left) and error (right) in time domain, where $m=1kg$ , $c_m=0.2Ns/m$ , $k=4\pi^2$ , $K_t=0N/A$ , $R_{nl}=0V^3/A$ (a), $S_w=10 (m/s^2)^2/Hz$ (b) .....	53
Figure 39: Input acceleration (left) and its <i>PSD</i> (right) used to obtain the equivalent load. For such an input the equivalent load is computed so that the mean square (or the probability that $Z \leq Im$ ) of the linear and the nonlinear system is the same .....	54
Figure 40: Harvesting force for the equivalent linear load (solid blue line) and cubic load (starred red markers) for $S_w=S_{w,max}$ .....	55
Figure 41: Probability function (left) of the displacement $z$ and probability density function (right) for the simulation parameters indicated in Table 3 – the vertical dashed line indicate the constraint on the amplitude of $z$ , the horizontal dotted line (left) indicate the lower and the upper limit of the probability such that the 95% of the sample satisfies the constraint .....	56
Figure 42: Power spectra of displacement (left) and velocity (right) for the cubic and the equivalent linear load where $m=1kg$ , $c_m=0.2Ns/m$ , $k=4\pi^2$ , $K_t=1.1N/A$ , $R_{nl}=11V^3/A$ , $R_{l,eq}=0.34\Omega$ , $S_w=S_{w,max}$ .....	57

- Figure 43: Cross spectrum of force and velocity for the cubic and the equivalent linear load where  
 $m=1kg$ ,  $c_m=0.2Ns/m$ ,  $k=4\pi^2$ ,  $K_t=1.1N/A$ ,  $R_{nl}=11V^3/A$ ,  $R_{l,eq}=0.34\Omega$ ,  $S_w=S_{w,max}$  60
- Figure 44: Average harvested power as a function of the electric load. The upper bound derived is indicated in blue solid line and assumes that all the input power is converted into harvested power; the solid dash dot line is the current case of study, in which a source of mechanical damping is introduced. If the electric load is zero, Langley's results are achieved.....61
- Figure 45: Average harvested power as a function of the electric load. Dashed red line is referred to the case  $R_t=0$  and dashed dotted red line is referred to the case  $R_t=0.1\Omega$ .....62
- Figure 46: Power spectra of displacement (left) and velocity (right) for the cubic and the equivalent linear load where  $m=1kg$ ,  $c_m=0.2Ns/m$ ,  $k=4\pi^2$ ,  $K_t=1.1N/A$ ,  $R_{nl}=11V^3/A$ ,  $R_{l,eq}=0.34\Omega$ ,  $S_w=S_{w,max}/5$  .....63
- Figure 47: Cross spectrum of force and velocity for the cubic and the equivalent linear load where  
 $m=1kg$ ,  $c_m=0.2Ns/m$ ,  $k=4\pi^2$ ,  $K_t=1.1N/A$ ,  $R_{nl}=11V^3/A$ ,  $R_{l,eq}=0.34\Omega$ ,  $S_w=S_{w,max}/564$
- Figure 48: Level curves of the variance of velocity (left) and average harvested power (right) where  
 $m=1kg$ ,  $c_m=0.2Ns/m$ ,  $k=4\pi^2$ ,  $K_t=1.1N/A$ ,  $R_{nl}=11V^3/A$ ,  $R_{l,eq}=0.34\Omega$  .....64
- Figure 49: Pierson-Moskowitz spectrum. The amplitude of the spectrum increases as the wind speed rises.....65
- Figure 50: Output spectra of the filter for two damping ratios –  $\zeta_f=0.01$  (solid line),  $\zeta_f=0.4$  (dash line).....67
- Figure 51: Harvesting force for the equivalent linear load (solid line) and cubic load (star markers) for  $S_w=S_{w,max}$ , and two values of damping of the filter  $\zeta_f=0.01$  (left) and  $\zeta_f=0.4$  (right) .....68
- Figure 52: Average harvested power as a function of the electric load for  $\zeta_f=0.01$  (left) and  $\zeta_f=0.4$  (right) .....69
- Figure 53: Power spectra of velocity (blue line, top) and cross spectrum of force and velocity (red line, bottom) for two values of the damping of the filter  $\zeta_f=0.01$ (left) and  $\zeta_f=0.4$ (right) - equivalent linear load (solid line) cubic load (dash dotted line) for  $S_w=S_{w,max}$  .....70
- Figure 54: Power spectra of velocity (blue line, top) and cross spectrum of force and velocity (red line, bottom) for two values of the damping of the filter  $\zeta_f=0.01$ (left) and

$\zeta_f=0.4$ (right) - equivalent linear load (solid line) cubic load (dash dotted line) for $S_w=S_{w,max}/5$ .....	71
Figure 55: Level curves of the variance of velocity (black line, top) and average harvested power (red line, bottom) for two values of the damping of the filter $\zeta_f=0.01$ (left) and $\zeta_f=0.4$ (right) - equivalent linear load (solid line) cubic load (dash dotted line).....	72
Figure 56: Shunt load as a function of the normalised input $S_w/S_{w,max}$ - the red solid line is referred to the variable load, the blue dashed line is referred to the constant load .....	73
Figure 57: Level curves of the variance of velocity (left) and average harvested power (right) as a function of the normalised input $S_w/S_{w,max}$ – equivalent linear load (solid line), cubic load (dash dotted line) and level-dependent load (dotted line).....	73
Figure 58: Energy harvester for boat's vertical motion (left) and free body diagram (right) .....	77
Figure 59: Average harvested power as a function of the load resistance - Experimental (dash red line) and numerical (blue solid line) results .....	79
Figure 60: Experimental set up.....	80
Figure 61 Relative transmissibility in frequency domain: open circuit (left) and load circuit (right) .....	81
Figure 62: Average harvested power in frequency domain for $R_l=0.5\Omega$ .....	81
Figure 63: A schematic representation of the proposed energy harvesting device consisting of an oscillating beam connected to a DC generator through a gearbox – Frontal view (left), top view (right).....	82
Figure 64: Set up for the measure of the viscous damping.....	87
Figure 65: Absolute value of the output voltage vs time - free oscillations .....	87
Figure 66: Exponential fitting of the relative maxima of the output voltage - experimental data (blue star markers) and numerical fitting (red dash line) .....	88
Figure 67: Output voltage vs time - experimental data (blue solid line) and numerical fitting (red dashed line) with an equivalent damping ratio of 0.83 .....	89
Figure 68: A schematic representation of the energy harvesting with tension spring .....	93
Figure 69: CAD model – isometric view (left) and upper view (right) .....	95
Figure 70: FEM of the energy harvester - the model shows that the parameters obtained from the design produces a first resonant frequency at 7.5 Hz .....	95



Figure 71: Manufactured device – isometric view (left), front view (right) .....	96
Figure 72: Average harvested power as a function of the shunt load when the input displacement is maximum .....	97
Figure 73: Angular displacement in load circuit as a function of the shunt load when the input displacement is maximum – by reducing the constraint on the maximum angular displacement from $3.6deg$ to $2.8deg$ , it can be noticed that the shunt load has to decrease up to $0.12\Omega$ .....	98
Figure 74: Shunt load as a function of the normalised input amplitude $Y/Y_{max}$ - constant shunt (dashed blue line) and a level-dependent shunt (solid red line).....	99
Figure 75: Level curves of the angular displacement $\theta_{LC}$ (left) and average harvested power $P_{ave}$ (right) for a constant (solid line), and a variable (dotted line) load as a function of the normalised input amplitude $Y/Y_{max}$ .....	99
Figure 76: Accelerometer 1 attached onto the base (left) and accelerometer 2 attached onto the lumped mass (right) .....	102
Figure 77: Schematic representation of the set up .....	103
Figure 78: Load circuit condition, the terminals of the generator are connected to a digital potentiometer .....	103
Figure 79: Open circuit condition (left), the terminals are not connected and short circuit (right) condition, a crocodile connects the terminals .....	104
Figure 80: Absolute transmissibility (left) and phase (right) as a function of frequency for different input voltage levels - Presence of friction can be detected at low levels.....	106
Figure 81: Spring as it appears before (left) and after (central) the modifications and zoom of the welded coil (right) - the holes through the disc allow the fastening with screws .....	107
Figure 82: Acceleration $\ddot{y}$ (top, left and right), acceleration $\ddot{x}$ (central, left and right) and output voltage (bottom, left and right) in time and frequency domains for a fixed input voltage level ( $2.4V$ ) and different operative conditions (short circuit, load circuit, open circuit).....	109
Figure 83: Linear relative displacement $Z$ (left) and the angular displacement $\theta$ (right) in frequency domain for a fixed input voltage level ( $2.4V$ ) and different operative conditions (short circuit, load circuit, open circuit) .....	110

Figure 84: Amplitude of the angular displacement (left) and output voltage (right) as a function of the electric load – harmonic excitation at the natural frequency with input voltage at $2.4V$ .....	111
Figure 85: Average harvested power as a function of the electric load – harmonic excitation at the natural frequency with input voltage at $2.4V$ .....	111
Figure 86: Level curves of the angular displacement $\theta$ for different loads such as short circuit (solid line), $R_l=0.35\Omega$ (dotted line), $R_l=1.3\Omega$ (dashed line), and open circuit (dash dot line) as a function of the normalised input amplitude $Y/Y_{max}$ .....	112
Figure 87: Level curves of the output voltage for different loads such as $R_l=0.35\Omega$ (dotted line), $R_l=1.3\Omega$ (dashed line), and open circuit (dash dot line) as a function of the normalised input amplitude $Y/Y_{max}$ – the short circuit is not reported as the output voltage is zero.....	113
Figure 88: Level curves of the average harvested power for different loads such as $R_l=0.35\Omega$ (dotted line), $R_l=1.3\Omega$ (dashed line) as a function of the normalised input amplitude $Y/Y_{max}$ – the short circuit and the open circuit are not reported as the power is zero .....	114
Figure 89: Level curves of the angular displacement $\theta$ for a constant (dotted line), and a variable (dotted line) load as a function of the normalised input amplitude $Y/Y_{max}$ ....	115
Figure 90: Shunt load as a function of the normalised input amplitude $Y/Y_{max}$ at resonance - the magenta solid line is referred to the constant load, the magenta dash line is referred to the variable load – the load increases when the input reduces until the optimum load is achieved.....	115
Figure 91: Level curves of the output voltage for a constant (dotted line), and a variable (dotted line) load as a function of the normalised input amplitude $Y/Y_{max}$ .....	116
Figure 92: Level curves of average harvested power for a constant (dotted line), and a variable (dotted line) load as a function of the normalised input amplitude $Y/Y_{max}$ ....	116

# DECLARATION OF AUTHORSHIP

I, **Luigi Simeone** declare that this thesis and the work presented in it are my own and has been generated by me as the result of my own original research.

## **Nonlinear damping in energy harvesters**

I confirm that:

1. This work was done wholly or mainly while in candidature for a research degree at this University;
2. Where any part of this thesis has previously been submitted for a degree or any other qualification at this University or any other institution, this has been clearly stated;
3. Where I have consulted the published work of others, this is always clearly attributed;
4. Where I have quoted from the work of others, the source is always given. With the exception of such quotations, this thesis is entirely my own work;
5. I have acknowledged all main sources of help;
6. Where the thesis is based on work done by myself jointly with others, I have made clear exactly what was done by others and what I have contributed myself;
7. Parts of this work have been published as indicated in the section Publications

Signed: Luigi Simeone

Date: 3/04/2017

# Acknowledgements

First and foremost, I would like to acknowledge my supervisors Prof. Maryam Ghandchi Tehrani and Prof. Steve Elliott, for giving me initially the opportunity to live this experience, for their guidance and support throughout this almost-four-year period at the Institute of Sound and Vibration Research. For all the meetings and suggestions, they provided me in order to complete my work.

This is for my beloved family who silently has always supported and believed in me. I wish they could be proud of me.

This is for my best friends; in particular, for those who shared this wonderful experience with me.

I just want to name (in alphabetic order) a few of them who were special to me: Dario, Giulia, Michele Iodice, Michele Zilletti, Viviana. I will always remember of you and I hope you will do the same with me.

These last four years have been among the best of my life and because of this, I will always be thankful.

# Definitions and Abbreviations

SDOF: single degree of freedom

$k$ : stiffness

$m$ : suspended mass

$c_m$ : linear viscous damping

$\omega$ : excitation frequency in rad/s

$\omega_n$ : natural frequency in rad/s

$f_n$ : natural frequency in Hz

$f_s$ : static friction coefficient

$y$ : sinusoidal base displacement

$K_t$ : transduction coefficient

$R_i$ : electrical internal resistance

$R_l$ : linear electric load

$z$ : relative displacement

$x$ : mass displacement

$i$ : current

$g$ : gravity

$R_{nl}$ : nonlinear electric load

$R_{l,eq}$ : equivalent linear load

$v$ : voltage

$Y$ : amplitude of the base displacement

$Y_{max}$ : maximum amplitude of the relative displacement

$Y_{acc}$ : amplitude of the base acceleration

$\varphi$ : phase

$t$ : time

$X$ : amplitude of the mass displacement  
 $X_{max}$ : maximum amplitude of the mass displacement  
 $Z$ : amplitude of the relative displacement  
 $Z_{max}$ : maximum amplitude of the relative displacement  
 $HB$ : harmonic balance method  
 $FFT$ : fast Fourier transform  
 $E[\cdot]$ : operator expectation  
 $P_{ave}$ : average harvested power  
 $R_{l,opt}$ : optimum electric load  
 $P_{opt}$ : average harvested power referred to the optimum load  
 $R_l(Y)$ : level dependent load  
 $R_w(x,t)$ : autocorrelation function  
 $\xi$ : random experiment  
 $\tau$ : the time lag  
 $S(j\omega)$ : power spectral density (PSD)  
 $k$ : k-realisation  
 $P(x)$ : probability distribution function  
 $p(x)$ : probability density function (PDF)  
 $p(x_1, x_2)$ : joint probability density function  
 $\mu_x$ : mean value  
 $\sigma^2$ : variance  
 $\sigma$ : standard deviation  
 $C_{x1x2}$ : covariance function  
 $\rho_{x1x2}$ : correlation coefficient  
 $\delta(\tau)$ : delta Dirac function

$e$ : error function  
 $f_{RI}$ : harvesting force  
 $H_{eq}$ : transfer function of the equivalent linear system  
 $P_{ub}$ : upper bound of the harvested power  
 $\zeta_m$ : mechanical damping ratio  
 $m_f$ : mass (referred to the second-order filter transfer function)  
 $k_f$ : stiffness (referred to the second-order filter transfer function)  
 $c_f$ : damping (referred to the second-order filter transfer function)  
 CAD: computer aided design  
 $O$ : origin of the inertial reference system  
 $l$ : length of the beam  
 $L$ : characteristic length of the lumped mass  
 $M$ : lumped mass  
 $l_m$ : position of the spring with respect to  $O$   
 $x_{CM,O}$ : x-coordinate of the centre of mass with respect to  $O$   
 $r_{CM}$ : position of the centre of mass with respect to  $O$   
 $\theta$ : angular displacement of the beam  
 $T$ : kinetic energy  
 $J_{CM}$ : moment of inertia  
 $m_{DC}$ : mass of the generator  
 $m_{extra}$ : mass of the flange and the base  
 $L_f$ : Lagrangian function  
 $b$ : height of the beam  
 $V$ : potential energy  
 $R$ : Rayleigh function

$M_{tot}$ : total mass  
 $c_{gb}$ : viscous damping of the gearbox  
 $c_{DC}$ : viscous damping of the gearbox  
 $v_{out}$ : output voltage  
 $G$ : gear ratio  
 $\omega_d$ : damped frequency in rad/s  
 $a$ : depth of the beam  
 $\rho$ : density of the beam and the lumped mass  
 $\theta_{OC}$ : amplitude of the angular displacement in open circuit  
 $\theta_{LC}$ : amplitude of the angular displacement in load circuit  
 $\theta_{LC,max}$ : maximum amplitude of the angular displacement in load circuit  
 $\delta_{st}$ : static deflection  
 $\delta_{dyn}$ : dynamic deflection  
 $c_e$ : electrical damping  
FEM: finite element model  
 $X/Y$ : absolute transmissibility  
 $Z/Y$ : relative transmissibility  
 $f_r$ : maximum-peak frequency



# Chapter 1: Introduction

## 1.1 Motivation

Energy harvesting (also known as energy scavenging) is a technology that allows one to capture ambient energy, such as solar, temperature gradients, strain, vibration, and transform it into electrical energy, which can be stored and employed to drive sensors or, in general, electronic devices. It represents a good solution for those systems that otherwise would rely on battery power.

The beneficial effects of energy harvesting are evident. Their use allows us to reduce the dependency on the battery power, which results in a reduction of the environmental impact and increase the operational lifecycle of autonomous and standalone applications, as well as the installation and the maintenance costs. Also, in hazardous environments, the harvester can enable sensing and actuation on a continuous basis, and, in theory, these self-powered devices remain functional as long as the ambient energy is available.

Wireless sensor nodes, for example, are used in several different applications such as automotive [1,2], healthcare [3] and computer science [4]. However when fitted with a battery, these sensors have a limited lifetime, and therefore, they need an external source of energy to operate. This hindrance has been overcome with energy harvesting, especially using MEMS (microelectromechanical systems) based devices [5,6].

Vibrating energy harvesting represents one of the possible solutions to feed low self-powered sensors. The physical principles, which drive this technology, can be of different kinds such as piezoelectric, electrostatic and electromagnetic, but the general goals are to use the ambient vibration, or in other words, the kinetic energy from the vibration source, to harvest power, and perhaps at the same time to suppress or damp the vibration of the source [7]. However, this second goal is related to the size of the harvester, which has to be comparable to the size of the host structure. More details about different technologies will be given in Chapter 2.

The amount of power harvested by these devices, is generally small with respect to other technologies, and therefore, researchers have begun to investigate different strategies to try to increase their performance. One trend has been to deliberately introduce nonlinearity into the system, which, depending on the type of nonlinearity, is a potential strategy to improve the performance, as discussed in Chapter 2.

The thesis is in the general area of nonlinear energy harvesting. The main motivation is to improve the performance of the vibrating energy harvesting device using nonlinear arrangements, in particular, focusing on the damping of the electromechanical system. The results obtained in the

following chapters allow us to draw important conclusions, which in turn, open new prospective for future research.

## 1.2 Novel contributions

The novel contributions of the thesis are:

- To propose an implementation of a cubic damping nonlinearity which can show a beneficial effect on the harvested power and can increase the dynamic range of performance;
- To study the effect of the parasitic friction on the harvested power in a vibrating energy harvester;
- To investigate the dynamics of a vibrating energy harvester with nonlinear cubic damping with Gaussian random noise excitation, of different bandwidths;
- To propose a new design of an electromagnetic transducer vibrating energy harvester;
- To demonstrate that a level-dependent load represents an advantageous strategy to increase the harvester power in electromagnetic transducer energy harvester;

## 1.3 Structure of the thesis

The thesis is organised in seven chapters.

Chapter 2 presents the literature relevant to the thesis. Starting from the general concept of energy harvesting, this chapter develops through a deeper description of vibrating energy harvesting with nonlinear damping for both harmonic and random excitations.

Chapter 3 introduces the dynamic model of a single-degree-of-freedom energy harvester with nonlinear damping. The system is assumed to be harmonically base excited. Three types of nonlinearity are included into the model, which are a cubic electric load, friction and a level-dependent load. The effect of these nonlinearities are analysed with particular interest to the harvested power. An analytical formulation is derived by using the harmonic balance method and compared with time domain simulations. The presence of friction can introduce nonlinearity into the damping force, which is especially relevant at low amplitudes of the input. On the other hand, the effect of a cubic electric load and a level-dependent load is promising and helps to increase the dynamic range of performance of the energy harvester when compared with linear devices, especially at low amplitudes of the input.

Chapter 4 begins with the assumption that the excitation is of a stochastic nature. By using numerical and analytical approaches, such as the equivalent linearization, it is shown that when the input is a Gaussian white noise, the harvested power does not depend on the damping nonlinearity, but only on the mass of the system for any given input acceleration. Also, the probability density function is analytically computed and used to evaluate how the cubic nonlinearity affects the response. A more

realistic and practical input is then analysed. A bandlimited input with a second order dynamics is employed, and it is demonstrated that this input represents a condition in between harmonic and white noise excitation.

In Chapter 5, an example of energy harvester for marine application is described from literature. In the following, a new design for a demonstrator of linear vibrating energy harvester with electromagnetic transduction is presented. The electromagnetic transduction is obtained by using a generator, which is coupled with a gearbox. The harvester is designed to be base excited by a specific shaker. Therefore, a set of constraints are taken into account, such as the maximum displacement of the oscillating mass and the natural frequency, which depend on the characteristics of the shaker. An analytical approach is used to derive all the parameters, such that the oscillating mass is able to resonate at a specific frequency with a certain input amplitude of the acceleration without violating the constraints.

Chapter 6 presents the experiments carried out on the energy harvester designed in Chapter 5. Firstly, the linear behaviour of the harvester is highlighted. The experimental results are supported by the analytical formulation, and they show good agreement with the theory. The mass displacement and the harvested power vary linearly and in a quadratic manner, respectively, with the input, and show a dramatic reduction only at low input, due to the presence of friction due to the gearbox. Then, a strategy to improve the harvested power is presented. It consists of varying the passive electric load, in other words the damping, with the excitation level. The results demonstrate that the harvested power is increased at low excitation levels compared with a linear device.

Finally, Chapter 7 summarises the findings of the thesis and presents suggestions for future work.

## Chapter 2: Literature review

### 2.1 Introduction

This chapter discusses the existing literature on energy harvesting relevant to this work. The first part of this chapter is dedicated to the energy harvesting technologies and to the concept of linear vibrating energy harvesting from a sinusoidal source. Following this, the discussion moves to those devices that are characterised by nonlinear dynamic behaviour, driven by harmonic or random ambient excitation.

### 2.2 Types of energy harvesting

Although, throughout this thesis, the term energy harvesting will be used to refer to the vibrational type only, it is worth to mention that there are other forms of energy harvesting which are classified on the basis of the energy they use. In Table 1, some of the main applications are classified in terms of the power density [8].

Table 1: Harvested power density for different applications (originally published in [8])

<i>Harvesting Technology</i>	<i>Power Density</i> $\left[ \frac{\mu W}{cm^3} \right]$
<i>Solar (outdoors)</i>	15000(Direct Sun), 150(Cloudy day)
<i>Solar (indoors)</i>	6(Office desk)
<i>Vibrations (piezoelectric conversion)</i>	250
<i>Vibrations (Electrostatic conversion)</i>	50
<i>Thermoelectric</i>	15 with 10°C temperature gradient

Photo-voltaic panels are one of the most popular energy harvesting devices. They use the photo-voltaic effect to convert light into electrical energy. For locations where the availability of light is guaranteed, and the usage of batteries is not feasible and expensive, this technology represents a convenient solution because of the large power density they can provide [9,10]. Another type of technology, which is being rapidly developed, relies on the Seebeck effect. The so-called thermoelectric energy harvesting utilises a temperature gradient to produce electrical energy to drive micro devices and sensors for space and terrestrial applications [11]. As aforementioned, this thesis focuses on the vibrating energy harvesting, which converts the oscillating motion of a mass into electrical energy. The technologies adopted to enhance this conversion are of three types: piezoelectric, electrostatic and electromagnetic. The electromagnetic transducer energy harvesting is the main subject of this thesis, but a brief description of the other two mechanisms will be given in section 2.3.

## 2.3 Vibrating energy harvesting

Energy harvesting from ambient vibration has attracted significant attention in recent years. In the last decades, many studies have been published, which deal with a wide variety of devices and applications. It is clear that, in case of vibrating energy harvesting, a mechanism is necessary to transform the mechanical vibration into electrical energy. This conversion can be achieved using three different mechanisms: piezoelectric, electrostatic and electromagnetic.

### 2.3.1 Piezoelectric harvesters

A piezoelectric harvesting device uses the electromechanical properties that some materials have. When these materials are subjected to a mechanical strain, they react producing an electrical current. For example, in [12] a piezo-generator was shown to achieve a maximum efficiency of 35%, which is about three times higher than what obtained from a solar cell due to a different kind of efficiency. Usually this type of technology is used as a layer in cantilever beam [6,13,14]. Piezoelectric devices can be modelled as electric circuits that act as high pass filters. This is the main reason why in applications where the dynamics involve low frequencies this mechanism is not suitable.

### 2.3.2 Electrostatic harvesters

Electrostatic energy harvesters are formed of two parallel conductive plates separated by a dielectric or air. When these plates are subjected to vibration, they move relative to each other, and this relative motion causes a variation in the capacitance, which in turn, produces an electromotive force induced into the device. The physical principles and their applications are discussed in [15,16].

### 2.3.3 Electromagnetic harvesters

Electromagnetic energy harvesting counts on the effect of the Faraday's law of induction. The variation of the magnetic flux, usually generated by a permanent magnet, which moves into a coil, induces an electromotive force (EMF) into the circuit. The electromotive force generates, in turn, a voltage across the terminals of the coil and, therefore, power harvested is produced. Many examples of this type of technology can be found in the literature, in particular for applications such as vibration dampers [17], vehicle suspension [1,18] and ocean waves [19]. This type of mechanism is suitable for low frequency excitation because an electromagnetic device can be modelled as a series of inductors and resistors, which act as a low pass filter.

## 2.4 Linear vibrating energy harvesting

The earliest studies on energy harvesting were focused on single-degree-of-freedom systems subjected to single-frequency excitation. In one of the most pioneering articles [20], a generator,

which consists of a seismic mass  $m$  on a spring  $k$ , is vibrated, and the out-of-phase motion between the generator housing and the seismic mass drives an electromagnetic transducer to generate electrical energy, which is represented by the damper  $d$ . It is assumed that no other form of damping exists in the system.

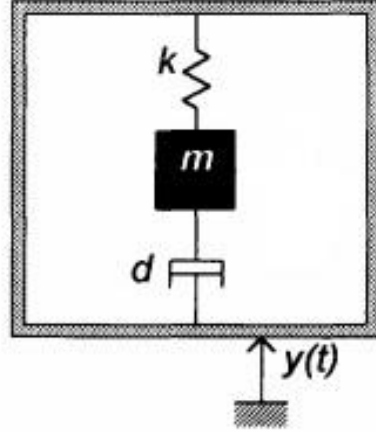


Figure 1: Schematic diagram of the generator (originally published in [20])

Assuming the generator to be harmonically excited at the angular frequency  $\omega$  with a displacement law of motion  $y(t)=Y\cos(\omega t)$ , as shown in Figure 1, the power generated can be written as,

$$P = \frac{m\zeta_l Y^2 \left(\frac{\omega}{\omega_n}\right)^3 \omega^3}{\left[1 - \left(\frac{\omega}{\omega_n}\right)^2\right]^2 + \left[2\zeta_l \frac{\omega}{\omega_n}\right]^2} \quad (2.1)$$

, where  $\zeta_l = c_l/2m\omega_n$  is the transducer damping factor,  $\omega_n = \sqrt{k/m}$  is the resonant angular frequency and  $Y$  is the amplitude of the input displacement. According to equation (2.1), the maximum power is achieved at resonance and depends on the damping factor. In fact, for structures whose response is very sharp and narrow, a low damping factor increases the generated power, while for structures with broader response, a higher damping is a better choice as it widens the frequency bandwidth. Moreover, this first result shows that the generated power is proportional to the cube of the vibration frequency, and, as a consequence, the generator performs better when is placed in an environment with a high frequency of vibration.

If the frequency of the external vibration matches with the natural frequency of the generator, equation (2.1) becomes:

$$P = \frac{mY^2 \omega_n^3}{4\zeta_l} \quad (2.2)$$

Theoretically, the maximum power is achieved when the transducer damping factor is equal to zero. A zero damping factor implies a dynamic response that is unlimited at resonance, however, and this is practically impossible since the maximum displacement the mass can oscillate is limited by the size and the geometry of the device. As a consequence, there exists a finite value of the damping factor so that the power output is finite.

So far, the damping is assumed to be all due to the harvester, but if mechanical damping is also present, the generated power is also constrained by the mechanical damping ratio  $\zeta_m$ . Assuming the dissipation to be in form of mechanical viscous damping, the generated power is of [20]

$$P = \frac{\zeta_l}{4(\zeta_l + \zeta_m)^2} mY^2 \omega_n^3 \quad (2.3)$$

These results allowed the authors to draw some guidelines to be generated, which can be considered as references when designing an energy harvesting device.

- The size of the mass should be as large as possible according to the available volume [20–24];
- The mass should move efficiently to use all the limited available space [20–23];
- The spring should be designed so that the resonant frequency of the device matches the vibration frequency of the application [20–25];
- The frequency bandwidth, over which the device works efficiently, can be enlarged by increasing the damping [6,21–23];
- The “unwanted damping” should be reduced so as not to unduly affect the generated power [20,23,24];

However, these guidelines assume a sinusoidal displacement excitation. In [8], it is stated that if one assumes that the amplitude of the input acceleration, rather than the amplitude of the input displacement, is independent of the excitation frequency, so that  $\ddot{y}(t) = Y_{acc} \cos \omega t$ , then all the considerations on the generated power change. Indeed, the generated power can be written, at the natural frequency, as:

$$P = \frac{mY_{acc}}{4\zeta_l \omega_n} \quad (2.4)$$

, where  $Y_{acc}$  is the amplitude of the input acceleration. This result is in contradiction with what shown in [20] and states the power is inversely proportional to the vibration frequency, and that an energy harvesting device should be designed to perform at low frequency.

The importance of the electrical damping for the maximum delivered power was raised in [21]. In this article, it was demonstrated that the electrical damping has a fundamental influence on the

delivery of the maximum harvested power to the electric load. In particular, the author shows that, in case of electromagnetic transducer energy harvesting, there exists an optimum value of the electric load for which the power delivered to the load is maximised. Nevertheless, since electromagnetic transduction is mainly used for large scale energy harvesting, the engineers usually have to deal with physical constraints such as, for example, the maximum displacement of the oscillating mass. Because of this, the author demonstrates that the electric load should be part of the design process for the constrained energy harvesting device, and not only a posteriori parameter, as it is when the device is unconstrained. In constrained energy harvesting devices, the maximum output power delivered to the load was found to be achieved when the electric load is set up equal to the internal dissipation of the coil.

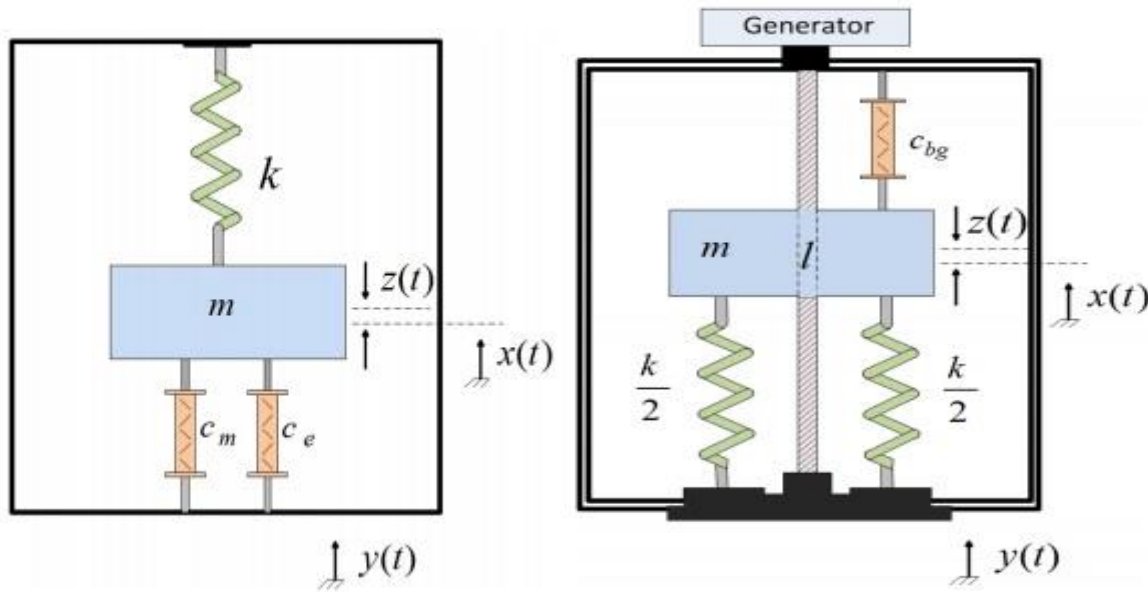


Figure 2: Schematic diagram of a linear (left) and a rotational (right) energy harvesting system (originally published in [26])

An important study related to the architecture of the harvester was conducted in [23,26]. The authors compared the output power and the efficiency of a linear and a rotational energy harvesting devices, as shown in Figure 2. With the term ‘linear’ is meant that the suspended mass translates, while in a ‘rotational’ device, the translation of the suspended mass is transformed into a rotational motion by mean a ball screw, which is coupled with a generator, as can be seen in Figure 2 (right). By defining the efficiency as the ratio between the output power delivered to the load and the input power from the vibration source, the article demonstrates that, the optimum load, for which the power is maximised is different from the optimum load for which the efficiency is maximised. However, this happens only for linear energy harvesters, while for rotational energy harvesters they coincide.

The superiority of the rotational harvester is due to the presence of the ball screw, which can be considered as a further variable parameter to optimise but such mechanisms of conversion of motion (ball screw, rack and pinion) do also introduce other types of nonlinear dissipation [27].



## 2.5 Nonlinear vibrating energy harvesting

The thesis is primarily focused on the effect that nonlinearities can have in energy harvesting devices. Before moving to the application though, it is worth briefly describing how nonlinear systems can be classified in terms of the type of solutions they manifest. A complete and analytical description is given in [28–31].

In the last decades, the advent of computers helped to solve nonlinear problems, which were previously considered unsolvable. This possibility led to a completely different perspective on dynamical systems and to a new language about dynamical systems in which the terminology is more geometrically oriented. Instead of quantitative solutions (which can be obtained only numerically in almost all cases), the qualitative behaviour is of larger interest, for instance the type of solutions, its stability, and the bifurcation of new solutions. Nonlinear dynamics became also popular because of the possibility of having irregular solutions even though the equations of motion are deterministic like in deterministic chaos. This behaviour is a characteristic of certain nonlinear systems (linear systems can never exhibit chaotic behaviour) which are extremely sensitive to initial conditions. Outside the scientific community, nonlinear dynamics is often confused with chaos theory, even though not all nonlinear systems behave in a chaotic manner.

Considering only a deterministic system, there exist different types of solutions depending on how they behave in the phase space.

The first type of solution is called fixed points. They are stationary solutions, which are obtained in unforced systems. These solutions can be stable or unstable. For example a pendulum has two fixed points, one at  $\theta=0deg$  (stable) and one at  $\theta=180deg$  (unstable). A typical phase space plot of such a solution is shown in Figure 3.

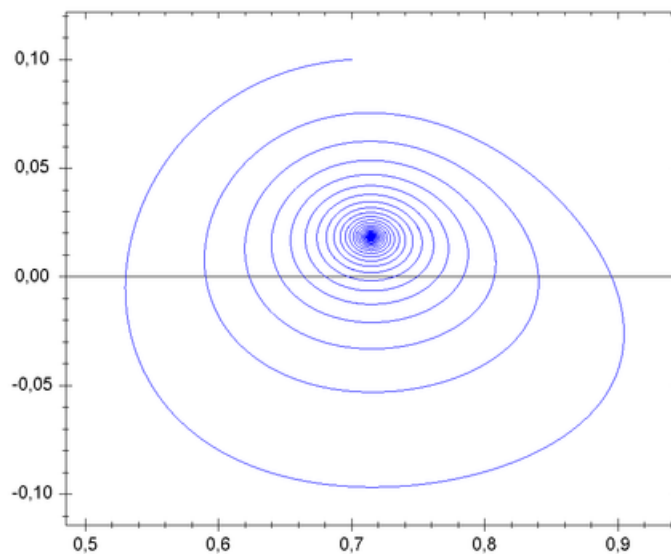


Figure 3: example of fixed-point solution

The second type of solution is termed limit cycle. These periodic solutions have closed trajectories in the phase space having the property that at least one other trajectory spirals into it either as time approaches infinity or as time approaches negative infinity. This behaviour is found in Van der Pol's equation as show in Figure 4.

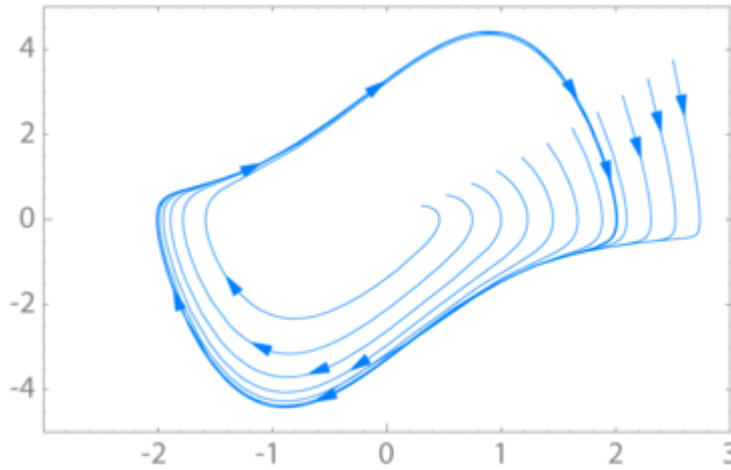


Figure 4: Stable limit cycle of Van der Pol's equation

The third type of solution is referred as quasi-periodic solutions. The peculiarity of these solutions is that the ratio between two frequencies (at least) is an irrational number. A typical example is a forced undamped pendulum.

The last type of solution is named as chaotic orbits. These solutions are generated by nonlinear systems which are strongly sensitive to initial conditions. An example is a double rod pendulum and a Duffing's oscillator, which can manifest chaotic behaviour when the parameters assume specific values, as shown in Figure 5.

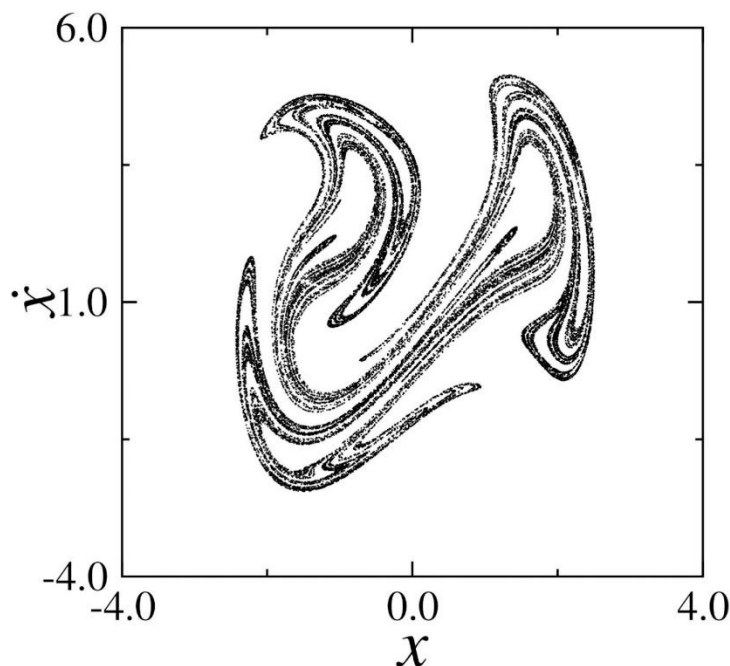


Figure 5: Chaotic attractor of Duffing equation (originally published in [29])

All the aforementioned solutions can then be stable or unstable. In particular, the stability can still be divided into asymptotical and marginal stability as shown in Figure 6. Asymptotically stable solutions are also called attractors

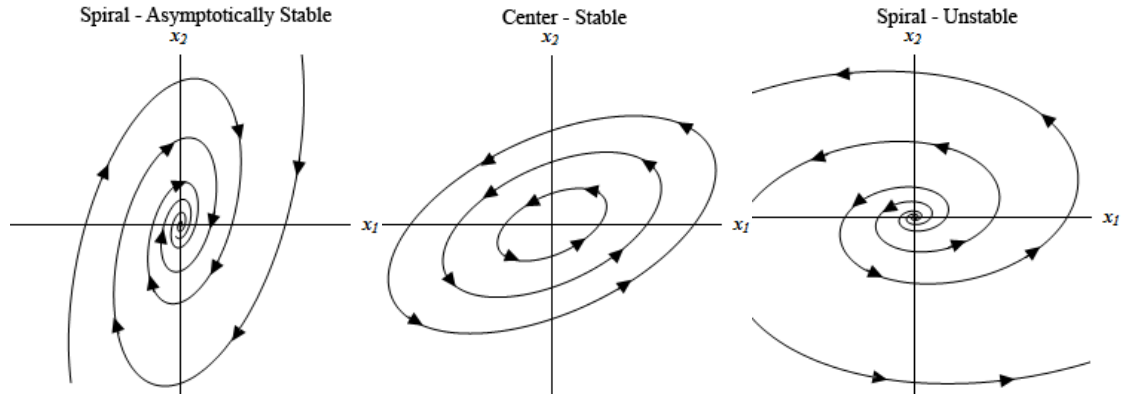


Figure 6: Example of asymptotically stable (left), stable (centred), unstable (right) systems

The number of attractors in a nonlinear system can change when a system parameter is varied. This change is called bifurcation and it is often accompanied by a variation of the stability of the solution. Bifurcation can be classified as local or global. In local bifurcation a parameter change causes the stability of an equilibrium (or fixed point) to change. In continuous systems, this corresponds to the real part of an eigenvalue of an equilibrium passing through zero. Global bifurcation instead causes changes in the topology of the trajectories in the phase space, which cannot be confined to a small neighbourhood, as is the case with local bifurcations. An example of bifurcation diagram is shown in Figure 7.

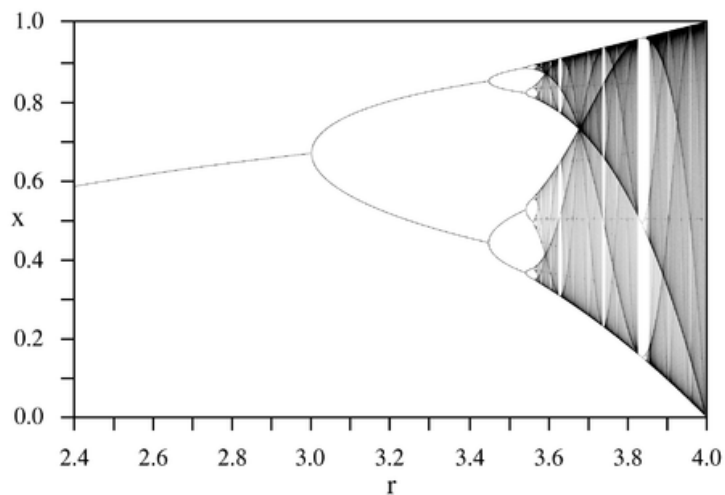


Figure 7: Bifurcation diagram - the system parameter  $r$  influences the attractor  $x$

In the last decade, researchers realised that the deliberate introduction of nonlinearity into energy harvesting devices can be beneficial. These benefits are of different type depending of the type of

nonlinearity. It is clear that the environmental excitation is the main aspect to consider when choosing the kind of nonlinearity, and, one can distinguish energy harvesting with nonlinear stiffness from energy harvesting with nonlinear damping.

Although the work shown hereafter primarily focuses on the second type, thus nonlinear damping, it is instructive to briefly discuss also the first type.

### 2.5.1 Energy harvesting with nonlinear stiffness

It is well-known that underdamped linear structures have a narrow frequency bandwidth over which the response is large. It was previously seen that one of the possible solutions to enlarge the frequency bandwidth is to increase the damping factor. However, this implies the response will reduce, and as a consequence, the generated power decreases. One of the possible solutions the researchers proposed is to introduce a nonlinearity in the stiffness, usually in the form of Duffing oscillator, which would allow the response to be larger than linear devices over a wider frequency bandwidth. A system characterised by a nonlinear spring exhibits the frequency response function, in Figure 8, which is caused by one solution or three different mathematical solutions at a singular frequency. However, practically only one is physical as the other ones are not stable equilibrium points.

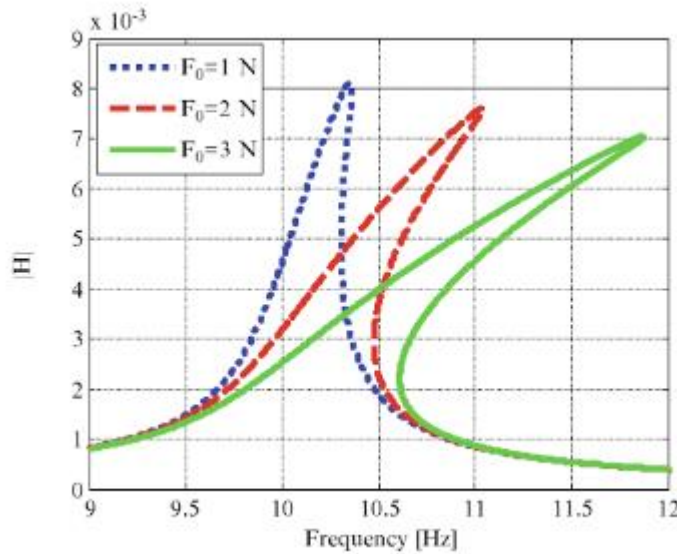


Figure 8: Example of frequency response function of a Duffing oscillator with hardening spring - increasing the amplitude of the input force the nonlinear behaviour is stronger

The majority of the studies conducted on this topic are focused on three types of design: impact [32,33], monostable [22,34,35], and bistable [22,36] energy harvesters. Impact devices use low-frequency ambient vibrations to impulsively excite otherwise linear harvesters so that they resonate at much lower frequencies than the natural frequency. Monostable harvesters can enlarge the frequency bandwidth over the resonant frequency. This broadening effect is a function of the strength of the nonlinearity and the input amplitude of the excitation. The term 'monostable' is referred to the

number of equilibrium points. In this case, it is only one equilibrium point. Bistable harvesters present two equilibrium points. In particular, this type of oscillator has a double-well restoring force potential, which provides three different steady-state conditions depending on the input-amplitude level.

A review of the recent research in bistable energy harvesters was published in [36]. Three designs of harvester are taken into account, as shown in Figure 9.

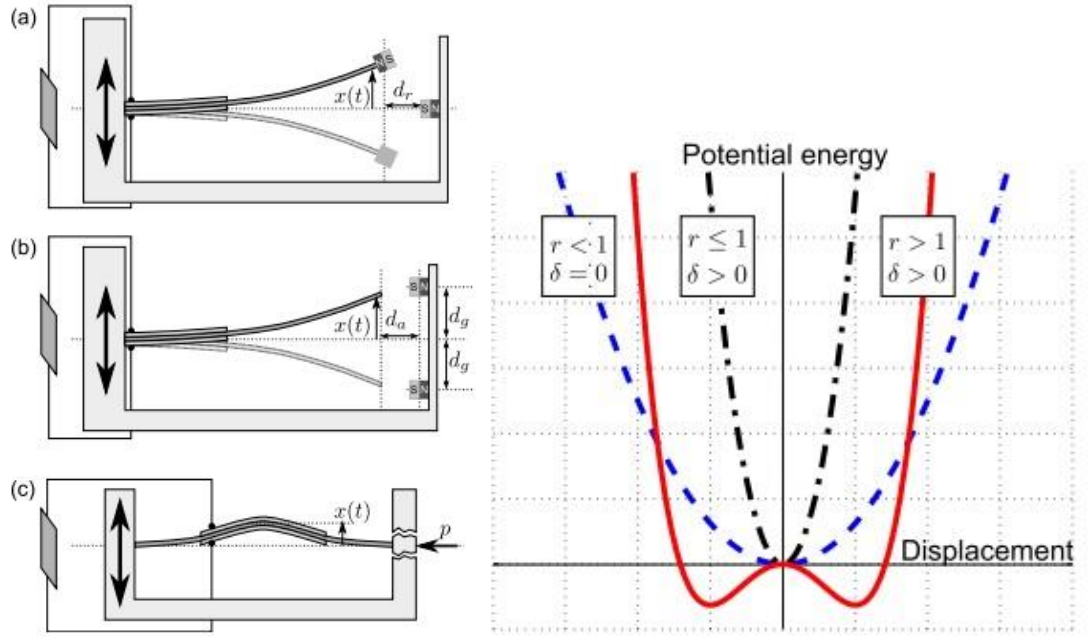


Figure 9: Bistable magnetic repulsion harvester (a), magnetic attraction harvester (b), buckled beam harvester (c), spring force potential (d) –  $r$  is the tuning parameter and  $\delta$  is the ratio between the nonlinear and the linear stiffness (originally published in [36])

In each case, a piezo patch is attached to the beam and connected to the harvesting circuitry (shown as parallelograms). The external frame is harmonically base excited and the relative motion between the beam and the base generates a strain that the piezo transforms into current. By increasing the input level of the excitation, the harvester may exhibit periodic oscillations within one well or aperiodic/chaotic oscillations between wells. The authors showed that by varying some parameters ( $r$  and  $\delta$ ), such as the distance between the beam and the magnet (a), the distance between the magnets (b) or the load condition such as the buckling force (c), the harvester moves from monostable to bistable behaviour, or vice versa. However, this work was mainly concentrated on the bistable behaviour and it was concluded that in this type of harvesters, the harvested power improves when compared linear harvesters.

In [37], a monostable and bistable were compared. It was concluded that the bistable harvesters was effective only if the chaotic behaviour was activated. However, this chaotic region is very sensitive to the input level and therefore, is hard to be achieved.

Several works were also conducted on randomly excited mono- and bistable energy harvesters [22,35]. The results showed that no significant improvements were achieved when a nonlinearity on the stiffness force was deliberately introduced into the harvesting devices.

To sum up, nonlinear stiffness can be useful strategy to enlarge the frequency bandwidth over which the harvested power is high. However, from the practical point of view there are some disadvantages. Experimentally, the identification of the jump point in the frequency response is hard as it is sensitive to small variations of the frequency of the input. In addition, a control has usually to be designed so that the harvester only work at the maximum amplitude region without jumping down to the lower branch of the frequency response. Another characteristic of system with nonlinear stiffness is that the response changes as you sweep up or down the excitation frequency. Therefore, also the 'direction' (up or down) the excitation frequency is varied is fundamental.

Another solution to broadening the bandwidth is to consider time-variant stiffness. In [38], the author modelled a SDOF system with parametric stiffness in order to generate a parametric resonance behaviour, described by the Mathieu equation.

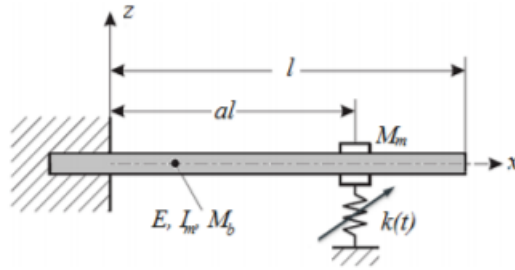


Figure 10: Cantilever beam with parametric stiffness (originally published in [38])

The system, in Figure 10, consists of a cantilever beam which has a periodic stiffness attached along its length. Experimentally, this effect was achieved by using a permanent magnet which moves relatively to two fixed outer electromagnetic coils. First, an analytical study was carried out in order to detect the stability regions of the parametric harvester and compared it with experimental results. Successfully, a piezoelectric sensor is attached onto the beam in order to generate harvested power. Numerical simulations and experiments showed that a periodic stiffness coefficient can be a valid solution to increase the output power compared to linear time-invariant system. In particular, the improvement is larger when the system is designed to work close at the instability region, because a higher amplitude of the response is produced, and when the harvester is excited at twice of its natural frequency.

### 2.5.2 Energy harvesting with nonlinear damping

Previously, it was highlighted that the introduction of nonlinear arrangements on the stiffness can have beneficial effects on the harvested power. It has to be pointed out that these arrangements are

active on the mechanics of the harvester, and they do not involve the electrical circuit, which is assumed to be linear. Moreover, nonlinear stiffness's can also provoke undesired effects, because the jumping phenomenon is hard to track. If the nonlinearity involves the damping force, then no multiple solutions appear, the system does not present unstable equilibrium point and it is not affected by the 'direction' the frequency of the external force is applied.

A typical example of nonlinear mechanical damping is represented by the friction, which will be discussed in more detail in Chapter 3. However, throughout this work, the introduction of nonlinear damping, to improve the performance of the harvester, relies on the possibility to synthesise a nonlinear electrical load, which can be beneficial for the harvested power, even though the typical source of dissipations (linear viscous damping, friction, electrical dissipations) take place.

A fundamental contribution to this topic is given in [39]. The authors considered a single-degree-of-freedom electromagnetic-transducer energy harvester subjected to a harmonic base excitation, as shown in Figure 11.

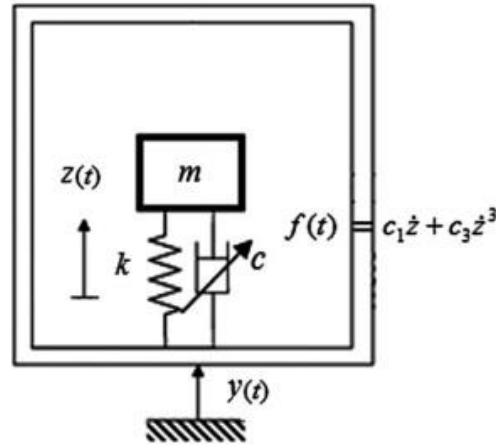


Figure 11: Single degree-of-freedom, base excited, energy harvesting system with nonlinear damper and an enclosure that restricts the maximum throw (originally published in [39])

Assuming the vibration frequency matches the natural frequency of the harvester, and that the internal resistance of the coil was zero, they demonstrate that a cubic damper can increase the dynamic range of performance with respect to the linear counterpart. In detail, to compare the linear and the nonlinear devices, the authors considered the two harvester to respond with the same relative displacement  $Z_{max}$  when excited at resonance for the maximum input level  $Y_{max}$ .

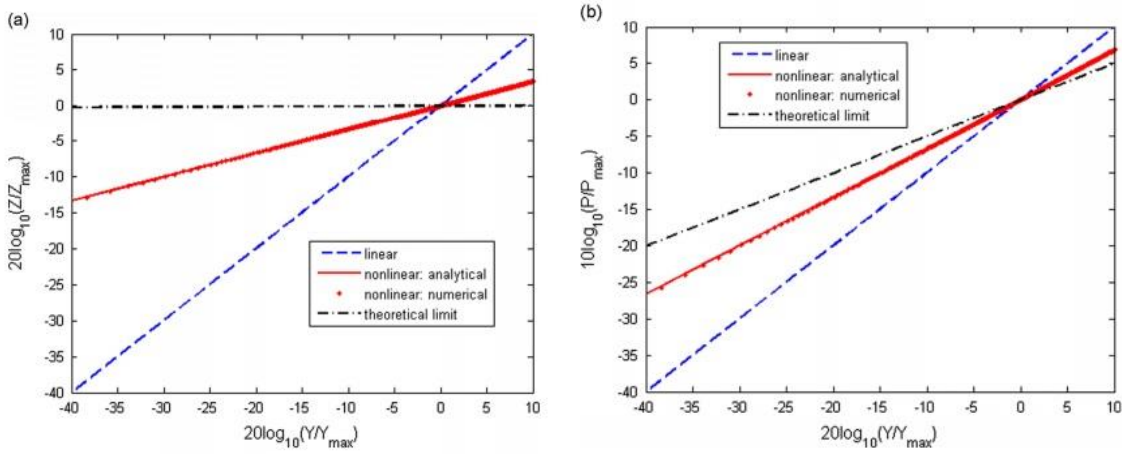


Figure 12: Relative displacement (left) and harvested power (right) for the linear system and nonlinear system with cubic damping, together with the theoretical limit of a highly nonlinear system, the solid line for the nonlinear case is calculated using the harmonic balance method and the dots are the results from time domain simulations (originally published in [39])

Due to the cubic-type nonlinearity, when the input level decreases, the force acting on the nonlinear damper is smaller than the force acting on the linear damper, and therefore, the relative displacement  $Z$  is larger, as seen in Figure 12(left). Also, it was demonstrated analytically that an increase of relative displacement  $Z$  has a direct effect on the harvested power, which improves as well when compared to the linear harvester, as shown in Figure 12(right). The results obtained in this article will cover part of Chapter 3.

Due to this promising results, the authors proposed an energy harvester in which the oscillating mass drives an electromechanical device, such as a generator, and the nonlinearity can be implemented using a nonlinear electrical load shunting this device.

In the case of a time-variant system an interesting study was conducted in [40]. The authors presented a semi-active control for optimising the average harvested power in electromagnetic devices. A time-variant damper is considered and expressed as Fourier series. The coefficients of the Fourier series are optimised at a specific frequency to obtain the maximum power. By tuning the semi-active harvester to have the same transmissibility at resonance of a passive device, it was shown that a time-variant damper can provide more harvested power than a passive one at any non-resonant frequency. In addition, as shown in Figure 13(left), assuming to have an arbitrary periodic damper, which has the same transmissibility at resonance of the optimised one, it was demonstrated that the optimised periodic damper provides more power off-resonance than an arbitrary periodic damper.



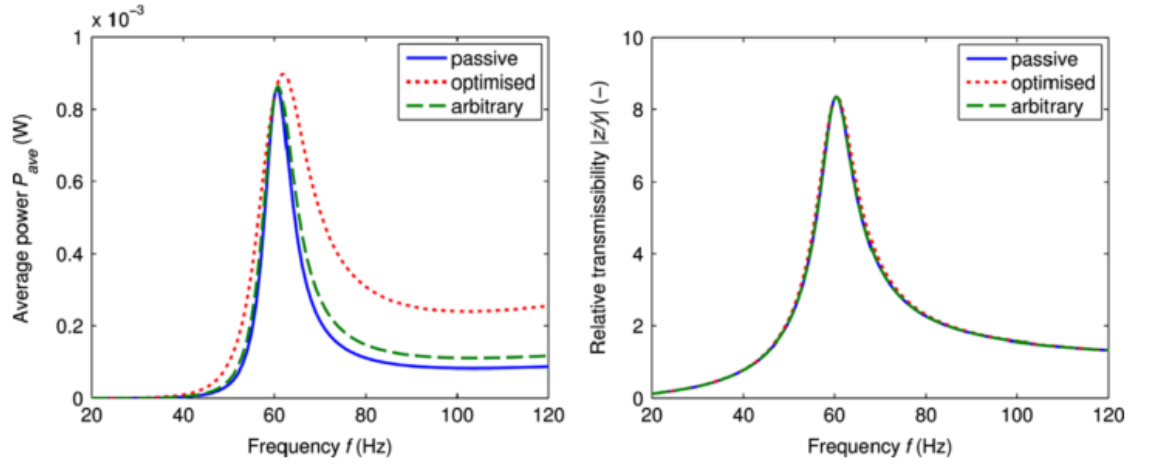


Figure 13: Passive, optimised and arbitrary harvester with the same transmissibility at resonance: average power (left) and relative transmissibility (right), (originally published in [40])

### 2.5.3 Random excitation

The assumption of harmonic excitation can be found valid in some applications, where the input is very narrow, such as ocean waves [19]. However, for other applications where the input is broader, such as the signal produced by a rough road, it is necessary to study the dynamics assuming random inputs, usually in the form of Gaussian white noise.

In [41], one of the most illuminating results was achieved. In case of Gaussian white noise input, if it is assumed that all the input power is delivered to the load or, in other words, that the input power is wholly transformed into harvested power, it was analytically and numerically found that the harvested power assumes the form of:

$$P = \frac{\pi M S_0}{2} \quad (2.5)$$

, where  $S_0$  is the one-sided power spectral density of the input acceleration, and  $M$  is the total mass of the system. This result represents an upper limit for the energy harvesting, because the maximum amount of power that can be harvested, which is equal to the input power according to the assumption, depends only on the mass of the harvester for any given white noise input. This limit, as indicated in (2.5), does not depend on the damping of the device, as one could expect. The upper bound can be theoretically achieved if the input is white noise and decreases if the frequency bandwidth of the input reduces, as shown in Figure 14.

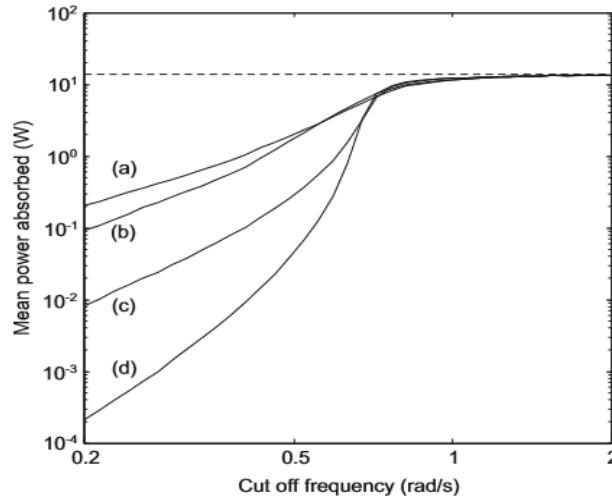


Figure 14: Power absorbed as a function of the cut off frequency of the excitation. The various curves correspond to different configurations of the damper and the spring: (a) nonlinear spring and linear damper, (b) nonlinear spring and nonlinear damper, (c) linear spring and linear damper, (d) linear spring and nonlinear damper. Dashed line: upper bound, (originally published in [41])

Nevertheless, this result has some limitations due to the assumption of white noise. First, the upper bound is not measurable; first because, in reality, a white noise input can never be generated; second because, even if a white noise input can be obtained, the total output power cannot be measured. Another paradoxical consequence of this result is that, in theory, if the oscillating mass is anchored to a fixed point, then the absorbed power is infinity because a fixed point can be seen as an infinite mass. The importance of this result relies on its general validity, as it holds for both linear and nonlinear systems, for both single and multi-degree of freedom (where  $M$  is mass matrix and  $S_0$  is a column vector). This result will form part of Chapter 4.

To design an energy harvesting solution, the nature of the ambient vibration has to be analysed in more detail. An important experimental survey was conducted in [42]. The authors extracted the power harvested from a piezoelectric vibration transducer, subjected to both laboratory shaker excitation and ambient excitation in a machine room of a large building. The study was focuses on the challenge of designing an energy harvesting device with low resonant frequency, which can operate within a real broadband excitation. The study was not aimed to optimize the harvested power. The main frequency of the input acceleration were within the range of  $35\text{-}235\text{Hz}$ , which is the same range the micro-device are set up. In Figure 15, the set up for the ambient measurements is shown.

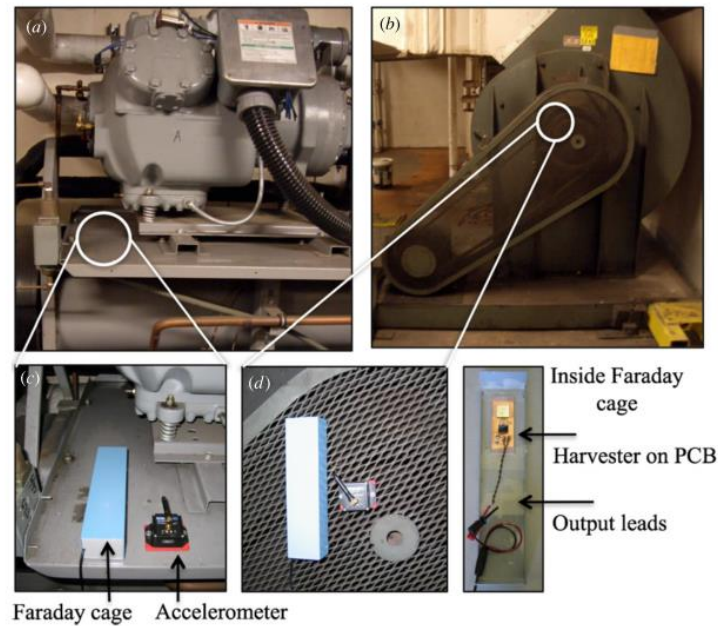


Figure 15: Photographs showing the testing configuration: (a) compressor base, (b) fan belt cage, (c) and (d) accelerometer (small black square) and Faraday cage containing the energy harvester (rectangular box) mounted for testing. (e) Faraday cage with lid removed to expose contents

The devices were characterised by using a shaker at low acceleration ( $0.03$ - $0.7g$ ) and then placed in the machine room. By mounting the MEMS device in a real environment the harvested power was lower ( $202\text{ pW}$  at  $32\text{ Hz}$  and  $0.15g$ ), then what obtained from the shaker measurement ( $1.72\text{ nW}$  at  $232\text{ Hz}$  and  $0.29g$ ). Due to the interaction of different resonant frequencies of different acceleration amplitudes, the maximum power was not obtained at the same frequency for the shaker and the machine room. However, by tuning the harvester to work in the same frequency bandwidth, output power can still be absorbed. The authors announced that future work should be focused on tuning the frequency bandwidth as well as optimising the maximum harvested power.

## 2.6 Application of electromagnetic harvesting to marine environment

The marine environment is one of the applications where large-scale energy harvesting can play an important role. Power requirement for lighting, navigation equipment and for automatic steering systems is typically in the range of 10 to 50 watts. To supply such an amount of power a 12-volt lead acid storage battery is commonly used, which is charged by the engine, in particular for short range cruising conditions. However, the request of utilising a renewable source of energy to charge the battery is taking place especially in the racing and long range cruising environments, which would prefer to avoid using the engine to charge the battery. For these applications, energy harvesting with electromagnetic transduction represents an attractive solution. However, in some existing energy harvesting applications, the maximum displacement of the seismic mass is constrained. This aspect limits the performance because the optimum load conditions cannot be achieved. In addition, the

presence of springs, which can behave in a nonlinear manner when over-extended, and the limited size of the energy harvesting device are other parameters which need to be considered. On the other hand, other types of transduction methods are limited in terms of geometry and allowable deformations; therefore, the electromagnetic transduction is the more convenient choice for large-scale applications. An important contribution to this topic was presented in [23] by M. Hendijanizadeh, where the author designed a linear large-scale electromagnetic-transducer energy harvester for marine applications. A description of the main aspects of this research will be given at the beginning of Chapter 5. Hendijanizadeh's research can be considered as a starting point for the design of the energy harvester proposed in Chapter 5. Even though the design rules are the same, the aim of the harvester proposed here is to demonstrate the benefits that a nonlinearity can produce into these kinds of devices, rather than being considered as a new prototype of energy harvester for real application, as was done in [23].

An important study on the nature of the ocean waves was conducted in [43]. The authors defined an empirical relationship between the power spectral density and the frequency within the ocean. This empirical model, developed in 1964, is one of the simplest descriptions of this phenomenon and assumes that if the wind blows steadily over a large area for a long time, then an equilibrium condition is achieved between the waves and the wind. At this condition, the sea is termed fully developed. To develop the model, the authors performed measurement in the North Atlantic, and used the acquired data to create the relationship between power distribution and wind.

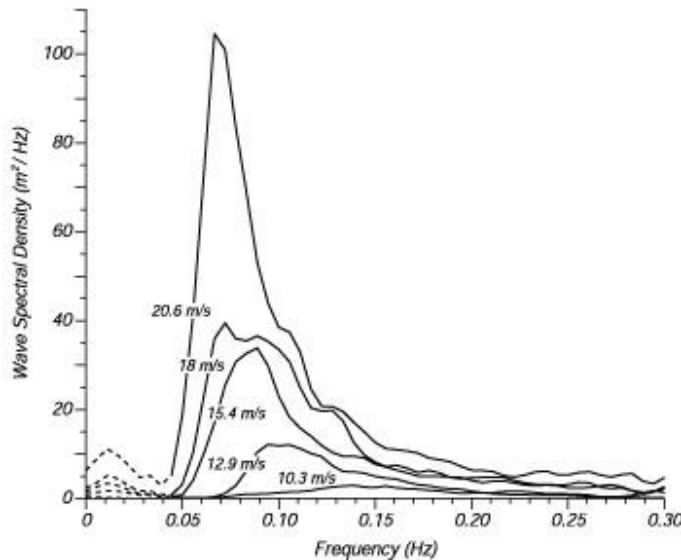


Figure 16: Pierson-Moskowitz spectrum (originally published in [39])

In Figure 16, the power spectral density of the displacement measured is shown as a function of the frequency for different values of wind speed. It can be noticed that the wind affects both the resonance frequency, the amplitude and the bandwidth. If the wind speed is low, the PSD is broader (and more damped) and the resonance is around 0.15Hz. By increasing the wind speed, the PSD becomes narrower (underdamped), the amplitude becomes larger and the resonance frequency reduces. In Chapter 4, for simplicity, the effect of such a spectrum on the harvested power will be

investigated partially. Although the resonant frequency will be maintained as a constant and equal to the resonance of the energy harvester, the amplitude and the bandwidth will not be constant but a variable parameter that depend on the damping ratio of a second-order function used to simulate the spectrum shown in Figure 16.

It is of primary importance to understand the characteristics of the environment before beginning the design process. As it will be demonstrated in Chapters 3 and 4, the harvester manifests an optimum value of the load for which the power is maximised. Nevertheless, this optimum depends on type of excitation.

## **2.7 Summary**

In this chapter, a review of the energy harvesting literature relevant to the work presented in this thesis has been carried out. More detailed information was given to those articles, which deal with nonlinear damping in energy harvesting, which can be considered as a starting point for this thesis work and, in particular, to those which presents electromagnetic transduction. In the following chapters, some of the studies presented in the literature will be recalled, and new results on the electromagnetic-transducer energy harvesting with nonlinear damping will be shown with particular attention to different types of excitation, such as harmonic, Gaussian white noise and Gaussian coloured noise.

## Chapter 3: Nonlinear damping in harmonically-excited energy harvesting device

### 3.1 Introduction

This chapter discusses the effect of a nonlinear electric load on the output power generated by a single-degree-of-freedom (SDOF) harmonically-excited energy harvesting device. In Chapter 2, it was pointed out that many forms of ambient excitation are stochastic in nature. Nevertheless, in some applications, the excitation is characterised by a very narrow frequency bandwidth and, therefore, the assumption of harmonic input can be adopted. Reciprocating machines and unbalanced rotating shafts are examples, in which the excitation can be assumed as sinusoidal. In addition, the majority of mechanical systems are also affected by parasitic dissipations. Hereafter, a simplification of this phenomenon is introduced in the form of Coulomb friction to take into account the static friction, which represents the main sources of energy losses in many mechanisms such as ball screw, rack and pinion and gearbox, as will be demonstrated in the experimental work in Chapter 6.

### 3.2 Electromechanical model

In this section, the modelling of an energy harvesting device is described. The mechanical system is composed by a suspended mass  $m$ , a spring of stiffness  $k$ , a linear viscous damping  $c_m$  and a static friction coefficient  $f_s$ . The mechanical system, subjected to a sinusoidal acceleration  $\ddot{y}$  at the base, is assumed to be coupled with an electromagnetic generator with transduction coefficient  $K_t = Bl_0$ , where  $B$  is the magnetic flux density and  $l_0$  is the length of the wire in the coil. The electrical internal resistance  $R_i$ , which causes dissipations by Joules effect, is neglected. Consequently, the harvested power is the amount of power delivered to an electric load  $R_l$ , which is attached across the terminals of the generator, as shown in Figure 17.

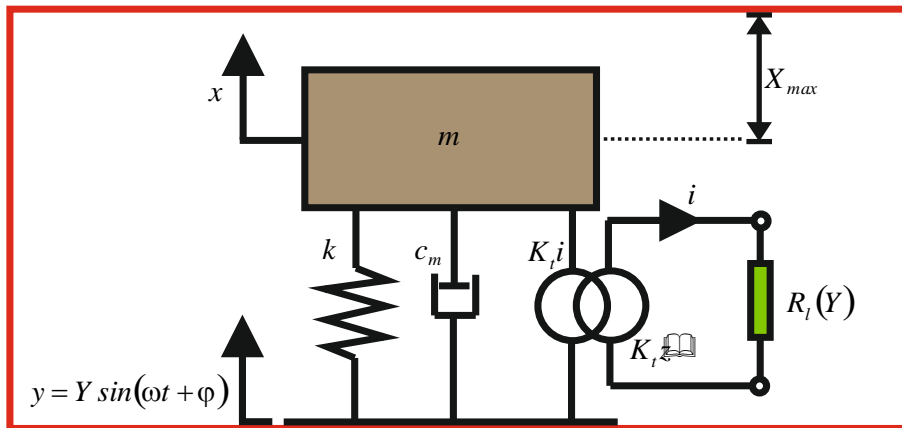


Figure 17: Schematic of the electromagnetic-transducer energy harvester – the mechanical system on the right is coupled with an electric circuitry on the left by means a generator

The oscillating motion of the suspended mass, which is excited by the base acceleration, induces an electromotive force (emf)  $K_t \dot{z}$  in the electric circuit of the generator, which, in turn, generates an electric damping force  $K_t i$  (where  $i$  is the current through the coil) in the mechanical system. The equation, which describes mechanical behaviour of the energy harvester, follows:

$$m\ddot{z} + c_m \dot{z} + f_s \operatorname{sgn}(\dot{z}) + kz + K_t i = -m\ddot{y} - mg \quad (3.1)$$

, where  $z=x-y$  is the relative displacement between the mass displacement  $x$  and the base displacement  $y$ . The dots indicate the derivations. The friction is here modelled as Coulomb damping, which represents the simplest and the mostly used model [22,49]. The signum function ( $\operatorname{sgn}$ ) is discontinuous at the origin, and is defined as:

$$\operatorname{sgn}(\dot{z}) = \begin{cases} 1, & \dot{z} > 0 \\ -1, & \dot{z} < 0 \end{cases} \quad (3.2)$$

the inductance of the generator is neglected, since at low frequencies the inductance does not much affect the electric circuit, then the equilibrium equation of the electric circuit can be written as:

$$K_t \dot{z} = (R_{nl} i)^{1/3} \quad (3.3)$$

, where a load has been assumed with the nonlinear characteristic and no electrical internal dissipation  $R_i$  are considered,

$$v = (R_{nl} i)^{1/3} \quad (3.4)$$

, so that,

$$i = \frac{K_t^3}{R_{nl}} \dot{z}^3 \quad (3.5)$$

Substituting equation (3.5) into equation (3.1), the ordinary differential equation (ODE) describing the electromechanical behaviour is obtained:

$$m\ddot{z} + c_m \dot{z} + f_s \operatorname{sgn}(\dot{z}) + \frac{K_t^4}{R_{nl}} \dot{z}^3 + kz = -m\ddot{y} - mg \quad (3.6)$$

Neglecting gravity, since it does not affect the output power, and assuming the base displacement in the form of  $y=Y\sin(\omega t+\varphi)$ , equation (3.6) becomes:

$$m\ddot{z} + c_m\dot{z} + f_s \operatorname{sgn}(\dot{z}) + \frac{K_t^4}{R_{nl}}\dot{z}^3 + kz = m\omega^2 Y \sin(\omega t + \varphi) \quad (3.7)$$

If the damping is divided into dissipating forces (friction plus mechanical viscous damping, shown Figure 18(left)) and the harvesting forces (electric load, Figure 18(right)), the contribution to the harvested power is only due to the latter.

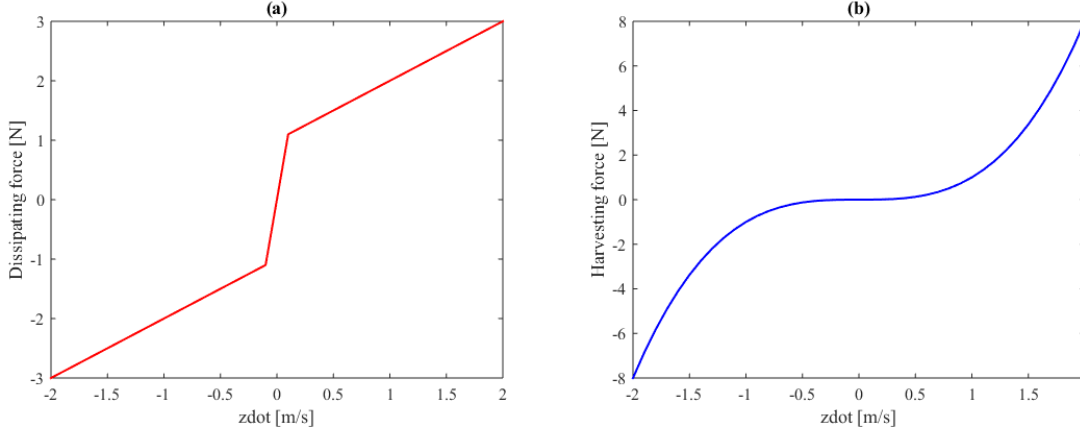


Figure 18: Examples of the dissipating (left) and harvesting force (right) for  $c_m = 1 \text{Ns/m}$ ,  $f_s = 1 \text{N}$ ,  $R_{nl} = 1.4 \text{V}^3/\text{A}$

It is known that only an odd damping function can generate harvested power, which justifies the choice of a third order polynomial rather than a second order polynomial. The reason is that if a quadratic damping function is used  $f(\dot{z}) = c\dot{z}^2$ , the harvested power can be indicated as  $f(\dot{z})\dot{z} = c\dot{z}^3$ . If the input is zero mean, all the odd statistical moments are zero and, consequently the average harvested power will be  $E[c\dot{z}^3] = 0$ .

### 3.3 Harmonic balance method

The exact solution of equation (3.7) is hard to obtain. Several methods can be found in literature, which provide a closed-form approximate solution, such as perturbation method [50], averaging method [51] and harmonic balance method [22,49]. The accuracy of these methods depends on the strength of the nonlinearity, the stronger of nonlinearity, the larger the approximation and, therefore, the error of the method [52]. Hereafter, the harmonic balance method is considered since it is straightforward to use compared to other methods.

The harmonic balance method (HB) assumes that the response of a harmonically excited system is at the frequency of the excitation, however with different amplitude  $Z$  and phase. Therefore, considering the right side of equation (3.7) and the assumption of the HB method, the response  $z$  can be written as;



$$z = Z \sin(\omega t) \quad (3.8)$$

The phase  $\varphi$  is associated to the input to simplify the further analysis. As aforementioned in the section 3.1, on the nature of  $Z$  are imposed assumptions and restrictions; when computing the roots of the algebraic polynomial system,  $Z$  can only be a real number as it will be used to compute the harvested power and only the real part is beneficial. However, the number of real solutions can still be larger than one. In that case, all the solutions would be kept.

Equation (3.8) and its derivations are substituted into equation (3.7) and the equation describing the electrodynamic behaviour of the harvester is derived as:

$$\begin{aligned} & -m\omega^2 Z \sin(\omega t) + c_m \omega Z \cos(\omega t) + f_s \operatorname{sgn}(\omega Z \cos(\omega t)) + \frac{K_t^4}{R_{nl}} (\omega Z \cos(\omega t))^3 + \\ & + kZ \sin(\omega t) = m\omega^2 Y \sin(\omega t + \varphi) \end{aligned} \quad (3.9)$$

The friction term and the cubic term are nonlinear and, therefore, they generate higher harmonic components. Since the harmonic balance method takes into account only the fundamental component (we could have chosen to consider more harmonics in the response  $z$  though), it is necessary to rewrite those terms in such a way that the fundamental component can be identified.

The cubic term can be decomposed using the Werner trigonometric formulas and only the fundamental component is taken as follows:

$$\cos^3(\omega t) = \left( \frac{1}{4} \cos(3\omega t) + \frac{3}{4} \cos(\omega t) \right) \approx \frac{3}{4} \cos(\omega t) \quad (3.10)$$

Decomposing the friction term in Fouries series and considering the fundamental frequency, it is:

$$\operatorname{sgn}(\cos \omega t) = \frac{4}{\pi} \cos \omega t + \frac{4}{3\pi} \cos 3\omega t + \frac{4}{5\pi} \cos 5\omega t + \dots \approx \frac{4}{\pi} \cos \omega t \quad (3.11)$$

The left side of equation (3.9) can be rewritten assuming that the response only happens at the fundamental frequency as:

$$-m\omega^2 Z \sin(\omega t) + c_m \omega Z \cos(\omega t) + \frac{4}{\pi} f_s \cos(\omega t) + \frac{3}{4} \frac{K_t^4}{R_{nl}} (\omega Z)^3 \cos(\omega t) + kZ \sin(\omega t) \quad (3.12)$$

The right side of equation (3.9) can also be rearranged using trigonometric relations. We have:

$$m\omega^2 Y \sin(\omega t + \varphi) = m\omega^2 Y [\sin(\omega t) \cos \varphi + \sin \varphi \cos(\omega t)] \quad (3.13)$$

Now, the harmonic balance can be applied balancing the coefficients of the sines terms on the left side with the sine term on the right side, and the same for the cosine terms. Two equations are obtained:

$$-m\omega^2 Z + kZ = m\omega^2 Y \cos \varphi \quad (3.14)$$

$$c_m \omega Z + \frac{4}{\pi} f_s + \frac{3}{4} \frac{K_t^4}{R_{nl}} (\omega Z)^3 = m\omega^2 Y \sin \varphi \quad (3.15)$$

Equation (3.14) is linear in  $Z$ , while equation (3.15) is nonlinear in  $Z$ , due to the presence of the friction and the cubic damping.

Squaring and summing equation (3.14) and equation (3.15), the electrodynamic equation can be written in the frequency domain as:

$$\left(-m\omega^2 Z + kZ\right)^2 + \left(c_m \omega Z + \frac{4}{\pi} f_s + \frac{3}{4} \frac{K_t^4}{R_{nl}} \omega^3 Z^3\right)^2 = m^2 \omega^4 Y^2 \quad (3.16)$$

This equation represents a sixth order polynomial algebraic equation, whose roots are the amplitudes  $Z$ . To obtain the analytical frequency response function, the equation (3.16) is solved using the Matlab command *roots* [53]. The approximate analytical result is then compared with the results from a time domain simulation run, using a fourth order Runge-Kutta numerical integration technique (*Ode45*) in Matlab Simulink [54]. The use of *Ode45* is due to the presence of a nonlinearity like the Coulomb friction, which is discontinuous and can provoke a sharp change in the solution that only a variable solver can track accurately.

### 3.4 Equivalent linearisation

The aim of this chapter is to show that the deliberate introduction of an electric cubic damping can improve the harvested power compared to the linear counterpart.

However, to compare the linear and the cubic harvesters, it is necessary to impose an operating condition, in which their behaviour is equivalent. When the operative conditions change, the linear and the cubic harvester respond differently, and considerations can be drawn based on the response and the harvested power. As mentioned in Chapter 2, the design of an energy harvesting device should consider some constraints. In particular, the main constraint involves the maximum relative displacement  $Z_{max}$  (or maximum displacement of the suspended mass  $X_{max}$ ), which is limited by the size and the available volume of the harvester. Hereafter, it is assumed that the maximum relative displacement  $Z_{max}$  occurs when the harvester is excited at the natural frequency  $\omega_n$  with the maximum input displacement  $Y_{max}$ . In case of harmonic excitation,  $Y_{max}$  is a measurable value that cannot be exceeded, because it represents the worst-case scenario for the input level of the environmental excitation. This represents the condition in which it is assumed that the linear and the cubic harvesters to have the same response. It is clear that if the linear and the nonlinear harvester respond with the same  $Z_{max}$  at the natural frequency, when  $Y=Y_{max}$ , the damping must be equivalent in some sense.

Therefore, an equivalent linear load  $R_{l,eq}$  is introduced and, in turn, the cubic  $R_{nl}$  is computed. At this stage, it is assumed that the system is not affected by the static friction, thus  $f_s=0N$ . To calculate the cubic damping, equation (3.16) is recalled and rewritten as:

$$\left(-m\omega^2 Z + kZ\right)^2 + \left(c_m \omega Z + \frac{3}{4} \frac{K_t^4}{R_{nl}} \omega^3 Z^3\right)^2 - m^2 \omega^4 Y^2 = 0, \quad (3.17)$$

, where the friction has been neglected. The same equation is derived for an equivalent linear energy harvester,

$$\left(-m\omega^2 Z + kZ\right)^2 + \left(c_m \omega Z + \frac{K_t^2}{R_{l,eq}} \omega Z\right)^2 - m^2 \omega^4 Y^2 = 0 \quad (3.18)$$

By making equation (3.17) and equation (3.18) to be equal at  $\omega=\omega_n$  and  $Y=Y_{max}$ , the following relation between the equivalent linear damping and the cubic damping is achieved:

$$R_{l,eq} = \frac{4}{3} \frac{R_{nl}}{K_t^2 \omega_n^2 Z_{max}^2} \quad (3.19)$$

From equation (3.19), for a given cubic load  $R_{nl}$ , an equivalent linear load  $R_{l,eq}$  (or vice versa a cubic load for a given linear load) can be computed, such that the two harvesting devices respond with the same relative displacement  $Z_{max}$  when  $\omega=\omega_n$  and  $Y=Y_{max}$ . The frequency response function of the relative transmissibility  $Z/Y_{max}$  is obtained solving equation (3.17), for the cubic harvester, and equation (3.18), for the linear harvester. The relative transmissibility is here defined as the ratio between the amplitude of the relative displacement  $Z$  and the maximum amplitude of the input displacement  $Y_{max}$  and is plotted in Figure 20. The simulation parameters are listed in Table 2.

Table 2: Parameters of the equivalent linear energy harvester

<i>Parameter</i>	<i>Value</i>
$m$ [kg]	1
$k$ [N/m]	$4\pi^2$
$c_m$ [Ns/m]	0.2
$K_t$ [N/A]	0.5
$R_{l,eq}$ [ $\Omega$ ]	0.185
$R_{nl}$ [ $V^3/A$ ]	1.37
$\omega_n$ [rad/s]	$2\pi$
$Y_{max}$ [m]	0.246
$Z_{max}$ [m]	1

Here, the friction is neglected, in order to evaluate the benefits of the cubic load with respect to the linear load. Afterwards, the static friction  $f_s$  will also be included and the equivalent linearization will be again applied to find a new value of  $R_{nl}$ . Using equation (3.18), the analytical expression for the relative transmissibility with cubic load can be obtained.

$$\frac{Z}{Y_{max}} = \frac{m\omega^2}{\sqrt{(k - m\omega^2)^2 + \left(c_m\omega + \frac{3}{4} \frac{K_t^4 \omega^3 Z^2}{R_{nl}}\right)^2}} \quad (3.20)$$

Mathematically, the equation has six solutions, and only the real positive solutions are considered as assumed previously. To solve it easily, the sixth order equation can be reduced to a third order equation by substituting  $Z^2$  with  $Q$ . Therefore, equation (3.17) becomes,

$$\frac{9}{16} \left( \frac{K_t^4 \omega^3}{R_{nl}} \right)^2 Q^3 + \frac{3}{2} c_m \frac{K_t^4}{R_{nl}} \omega^4 Q^2 + (m^2 \omega^4 + k^2 - 2mk\omega^2 + c_m^2 \omega^2) Q - m^2 \omega^4 Y^2 = 0 \quad (3.21)$$

Now, depending on the discriminant, a cubic algebraic equation can have either three distinct real roots, or real multiple roots or one real root and two complex conjugate roots. The general cubic equation has the form:

$$ax^3 + bx^2 + cx + d = 0 \quad (3.22)$$

The discriminant is defined as,

$$\Delta = 18abcd - 4b^3d + b^2c^2 - 4ac^3 - 27a^2d^2 \quad (3.23)$$

As aforementioned, three types of solutions can be obtained:

- $\Delta > 0$ : three distinct real roots;
- $\Delta = 0$ : Three multiple roots;
- $\Delta < 0$ : One real root and two complex conjugate roots;

The discriminant is plotted in Figure 19. The discriminant is always negative therefore, one real root and two complex conjugate roots are obtained. Because of the assumption that  $Z$  is a real positive number, the two complex conjugate solutions are neglected and only the real one is kept.

By taking the square root of the real root  $Q$  we obtain two possible values for  $Z$ , one positive and one negative. As  $Z$  is an amplitude, which is always a positive number by definition (given a complex number,  $z = x + iy$ , the amplitude is  $\sqrt{x^2 + y^2}$ ), only one solution  $Z$  is taken to construct the steady state transfer function

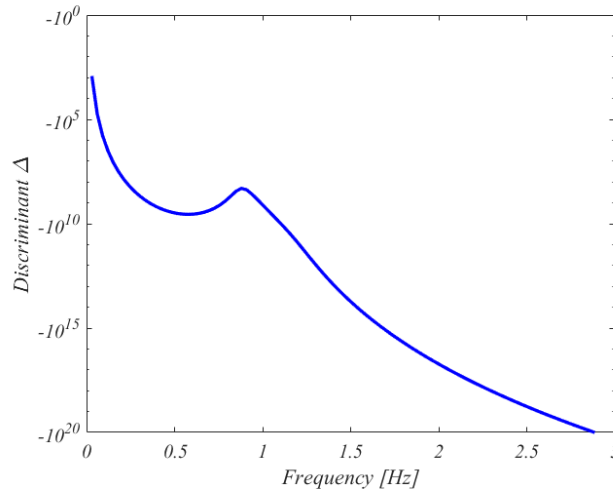


Figure 19: Discriminant of the cubic equation as a function of the frequency - one real solution and two complex conjugate solutions are obtained

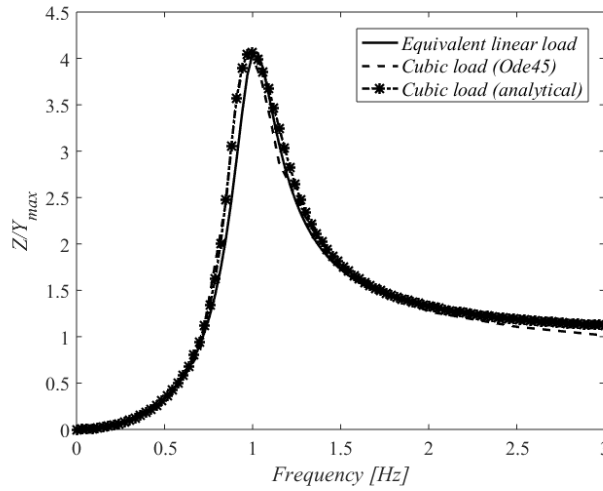


Figure 20: Relative transmissibility as a function of the frequency for linear (solid black line) and cubic (dash black line) energy harvesters where  $m=1\text{kg}$ ,  $k=4\pi^2$ ,  $c_m=0.2\text{Ns/m}$ ,  $R_{l,eq}=0.185\text{Ns/m}$ ,  $R_{nl}=1.37\text{V}^3/\text{A}$ ,  $Y_{max}=0.246\text{m}$  – dashed dotted line with star markers is referred to the analytical solution obtained by the harmonic balance method

From Figure 20, at the natural frequency, the equivalent condition occurs, where the cubic and the equivalent linear energy harvesting devices have the same relative transmissibility  $Z/Y_{max}$  (which is about 4) and a phase shift of  $90\text{deg}$ . At high frequencies, the relative transmissibility tends to one and the phase is zero, which means that the suspended mass does not oscillate. All the input power is transmitted to the damper, and is dissipated. At low frequencies, the amplitude of the mass displacement  $X$  is equal to the amplitude of the base displacement  $Y$ , therefore,  $Z$  is zero, and the phase shift is  $180\text{deg}$ . It has to be noticed that only one real solution was present at this time.

The cubic load computed using equation (3.19), is derived from an analytical approximate method. Therefore, it is clear that the analytical approximate cubic solution ( $HB$ ) is not exactly equal to the

numerical solution (*Ode45*), which is assumed to be the exact solution. However, there is a reasonably good agreement between the harmonic balance and numerical simulation and, at resonance; the difference is minimal because the effect of the higher harmonic components (for example the odd harmonics typical of the cubic damping) is weak. The good agreement between the analytical and the numerical methods highlights the stability of the solution. In Figure 21, the FFT of the analytical approximate solution is compared with the FFT of the numerical solution (*Ode45*). At the fundamental frequency, both the solutions have the same amplitude. The zoomed plot shows that the numerical integration has the third harmonic component, which, instead, is not detectable in the analytical solution because of the assumption of the method in equation (3.8).

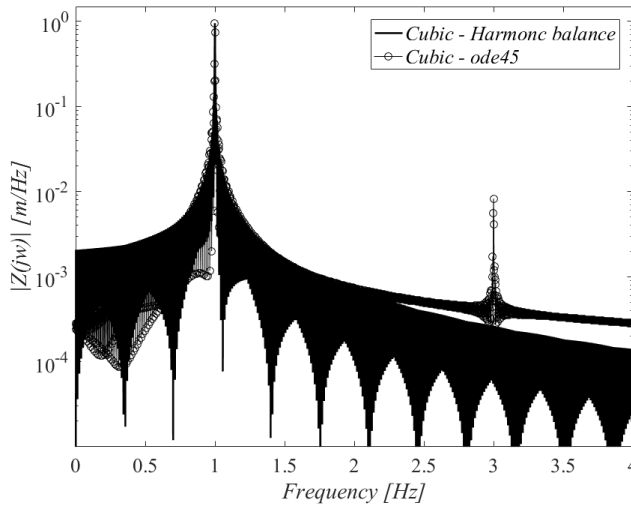


Figure 21: FFT of the relative displacement at resonance for  $Y=Y_{max}$  - harmonic balance (solid black line) and ode45 (solid black line with circle markers). It is evident the presence of a third harmonic component in numerical solution (in the zoomed plot), which, instead, is not present in the analytical solution.

It has been shown that the presence of an electric load  $R_l$  acts as an additional viscous damping, which can be linear or cubic depending of the voltage across the load. The output power can then be computed as the damping force due to the electric load times the velocity. For a linear energy harvesting device, we have:

$$P_{ave} = \frac{K_t^2}{R_{l,eq}} E[\dot{x}^2] \quad (3.24)$$

, where  $E[\cdot]$  is the operator expectation, which averages the instantaneous power over time. The relation between the power and the amplitude of the relative displacement can be obtained in frequency domain, where equation (3.24) becomes:

$$P_{ave} = \frac{1}{2} \frac{K_t^2}{R_{l,eq}} \omega^2 Z^2 \quad (3.25)$$

For a cubic energy harvesting device, the average harvested power can be written in time domain as:

$$P_{ave} = \frac{K_t^4}{R_{nl}} E[\dot{x}^4] \quad (3.26)$$

, and in the frequency domain as:

$$P_{ave} = \frac{3}{8} \frac{K_t^4}{R_{nl}} \omega^4 Z^4 \quad (3.27)$$

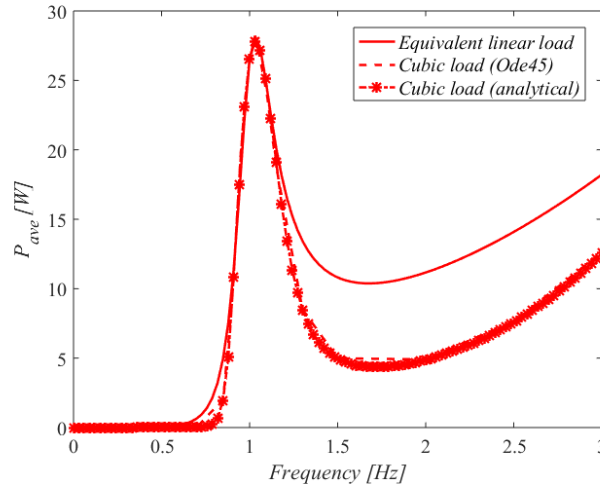


Figure 22: Average harvested power as a function of the frequency for linear (solid red line) and cubic (dashed red line) energy harvesters where  $m=1\text{kg}$ ,  $k=4\pi^2$ ,  $c_m=0.2\text{Ns/m}$ ,  $R_{l,eq}=0.185\text{Ns/m}$ ,  $R_{nl}=1.37\text{V}^3/\text{A}$ ,  $Y_{max}=0.246m$  – dashed dot line with star markers is referred to the analytical solution obtained by the harmonic balance method

At the natural frequency, the linear and the nonlinear harvesters have the same harvested power, as it can be seen from Figure 22, which is a consequence of having imposed the same relative displacement  $Z_{max}=Im$ .

As mentioned in Chapter 2, the frequency of the excitation plays an important role in choosing an appropriate technology (piezo, electromagnetic, etc.) for designing an energy harvesting device. The harvested power increases with the square of the vibration frequency in linear devices, as shown in equation (3.25), however increases with the fourth power of the vibration frequency when cubic load is used, as shown in equation (3.27). It must be remembered that, electromagnetic transduction, which is the type of transduction studied in this thesis, is not effective at high frequencies (which is the reason for choosing such a low resonance frequency), where instead a piezo electric solution is more suitable, and therefore, high frequency analysis is not considered here.

### 3.5 Optimum load resistance

In Chapter 2, it was explained that in electromagnetic transducer energy harvesting devices, an optimum value of load resistance  $R_{l,opt}$  can be found such that the harvested power is maximised [21,23,24]. Some authors [23,24] assert that the electric load should be part of the design, which would allow to design a harvester that works at the best operating conditions. However, from the practical point of view, this may not be the correct strategy as it can happen that the properties of the energy harvester, such as the mechanical damping, change, for example, in environment where the temperature varies over a wide range, and therefore, the designed electric load is no longer the optimum. Consequently, in some applications the load is a posteriori parameter. According to this, the electric load  $R_l$  is considered as a posteriori tuneable parameter, which can be adapted according to the nature of the ambient.

In the previous section, the relative transmissibility was plotted assuming arbitrarily a cubic load  $R_{nl}$  that does not necessarily coincide with the optimum load  $R_{l,opt}$ . To investigate the effect of the damping on the harvested power, equation (3.25) and equation (3.27) are recalled. If the energy harvester is driven at the natural frequency, the equation (3.25) becomes:

$$P_{ave} = \frac{1}{2} \frac{K_t^2}{R_{l,eq}} \omega_n^2 \left( \frac{m \omega_n Y}{\frac{K_t^2}{R_{l,eq}} + c_m} \right)^2 \quad (3.28)$$

, where the response  $Z$  has been calculated at the natural frequency by solving equation (3.18). The optimum value of the load  $R_{l,opt}$ , for which the harvested power is maximised, can be found by imposing the first derivative of the harvested power, with respect to the damping  $R_{l,eq}$ , to be zero as:

$$\frac{\partial P_{ave}}{\partial R_{l,eq}} = 0 \quad (3.29)$$

, solving equation (3.29), it yields:

$$R_{l,opt} = \frac{K_t^2}{c_m} \quad (3.30)$$

The optimum load is found to depend on the type of generator  $K_t$  and the mechanical viscous damping  $c_m$ , as confirmed also in [21,23,24].



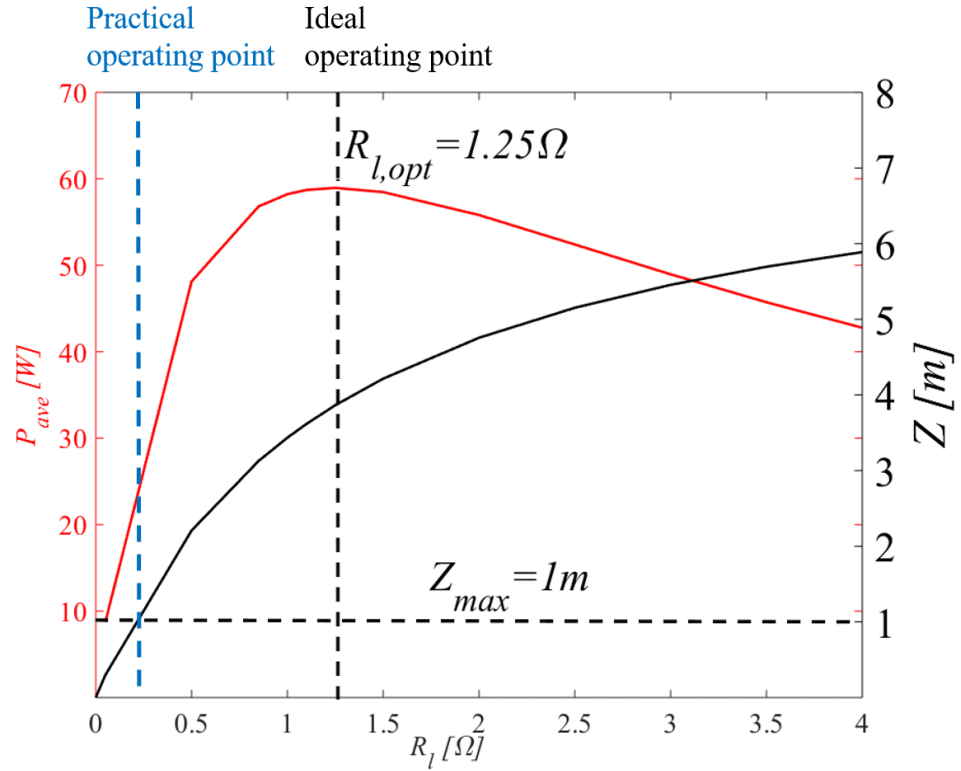


Figure 23: Average harvested power (solid red line) and relative displacement (solid black line) as a function of the equivalent viscous damping at the natural frequency for  $Y=Y_{max}$  - the black dashed dotted line represents the constraint on the maximum displacement  $Z_{max}$  while the red dashed dotted line yields the value of the maximum harvested power  $P_{max}$  and equivalent damping  $R_{l,eq}$  corresponding to  $Z_{max}$ . As shown, the energy harvester does not work at the optimum conditions  $(R_{l,opt}, P_{opt})$

In Figure 23, if the energy harvester is constrained by the maximum relative displacement  $Z_{max}$ , it is clear that the optimum harvested power  $P_{opt}=60W$  cannot be achievable because the amplitude of the response would be  $4m$ . Therefore, the device must operate at  $R_l=0.185\Omega$ , corresponding to the harvested power equal to  $24W$ . The integrity of the device is the main concern when designing an energy harvester, and, consequently, in linear devices, one has to accept a reduction of performance to ensure a high reliability of the system. This hindrance will be overcome at the end of this chapter, where the level-dependent load will be introduced. It will be shown that nonlinearity in the damping allows energy harvester to operate always at its optimum conditions.

### 3.6 Benefit of the cubic load resistance

The cubic load is characterised by the fact that the current flowing through the coil is proportional to the cubic of the voltage across it. As the load affects the dynamic response at the natural frequency, all the analyses in this chapter will be run assuming the frequency of excitation to be at the natural frequency. Also, it is well-known that the output of a nonlinear system is not directly proportional to the input, and therefore, the following analysis will consider a variable input displacement  $Y$ . In the

first part of this section, the friction will be still neglected. However, this assumption will be relaxed in the next section.

Recalling equation (3.18) and imposing  $\omega=\omega_n$ , the relative displacement of the linear energy harvester can be written as:

$$Z = \frac{m\omega_n^2 Y}{c_m + \frac{K_t^2}{R_{l,eq}}} \quad (3.31)$$

The relative displacement  $Z$  is directly proportional to the input displacement  $Y$ . The harvested power can then be computed from equation (3.25). For the nonlinear energy harvester, a third order polynomial in  $Z$  is obtained as follows

$$\frac{3}{4}c_3\omega_n^3 Z^3 + c_m\omega_n Z - m\omega_n^2 Y = 0. \quad (3.32)$$

Equation (3.32), which is solved using the Matlab command *roots*, is clearly nonlinear and underlines that  $Z$  is not directly proportional to  $Y$ . The peculiarity of the cubic damping can be appreciated plotting the relative transmissibility (Figure 24(left)) and the average harvested power (Figure 24(right)) in frequency domain assuming the input displacement  $Y$  to be a fifth of the maximum input amplitude, thus  $Y=Y_{max}/5$ .

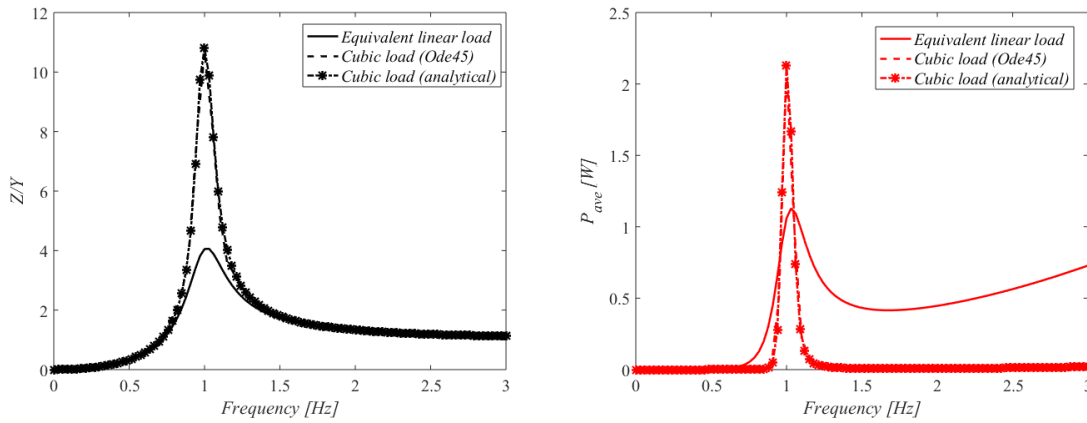


Figure 24: Relative transmissibility (left) and average harvested power (right) as a function of the frequency for linear (solid line) and cubic (dashed line) energy harvesters where  $m=1kg$ ,  $k=4\pi^2$ ,  $c_m=0.2Ns/m$ ,  $R_{l,eq}=0.185Ns/m$ ,  $R_{nl}=1.37V^3/A$ ,  $Y=0.049m$  – dashed-dotted line with star markers is referred to the analytical solution obtained by the harmonic balance method

In linear systems, the ratio between input and output remains the same, and therefore, the relative displacement does not change when the input level varies. The introduction of cubic nonlinearity instead makes the relative transmissibility to grow with respect to the linear harvester. This effect is

due to the fact that, at low input levels, the force acting on the cubic damper (the electric load can be considered as a cubic damper) is smaller than the force acting on the linear damper, and, as a consequence, the response is larger. The reduction of damping force detected in the nonlinear harvester is beneficial for the harvested power. Indeed, in Figure 24(right), if the input level  $Y$  is a fifth of the maximum input  $Y_{max}$ , the nonlinear device provides more than twice the harvested power of the linear device.

The effect of the cubic damping can also be demonstrated by the level curves. The level curves show the effect of the input level  $Y$  on the relative displacement  $Z$  and the harvested power  $P_{ave}$ , when the system is excited at the natural frequency. Equation (3.31) and equation (3.32) allow us to compute the level curves of the relative displacement  $Z$  for the linear and the cubic harvester respectively, as shown in Figure 25.

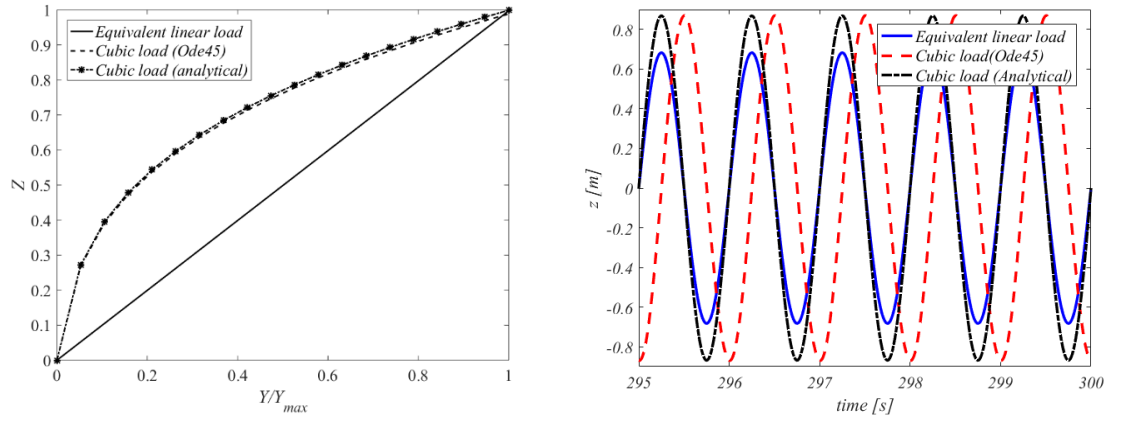


Figure 25: Level curves of the relative displacement  $Z$  (left) for linear (solid line) and cubic (dashed line) energy harvesters as a function of the normalised input amplitude  $Y/Y_{max}$  and time history of the relative displacement (right) for  $Y/Y_{max}=0.68$ , where  $m=1\text{kg}$ ,  $k=4\pi^2$ ,  $c_m=0.2\text{Ns/m}$ ,  $R_{l,eq}=0.185\text{Ns/m}$ ,  $R_{nl}=1.37\text{V}^3/\text{A}$ ,  $Y_{max}=0.246\text{m}$

It can be noticed that the response of the cubic harvester is larger than the linear counterpart in the entire dynamic range. It can be also appreciated the good agreement between the numerical solution and the approximate analytical solution, which means that the effect of the higher harmonic component can be neglected. In the time domain, the equivalent linear load and the cubic load (analytical) are in phase because of the harmonic balance method, while the numerical solution is out-of-phase. It can also be noticed how the numerical response in the time domain looks linear. The effect of the higher harmonics is very small; however, the difference of amplitude compared to the equivalent linear load is consistent.

According to equation (3.24) and equation (3.26), the harvested power is proportional to the square of velocity for the linear case and the fourth-power of velocity for the cubic case. Therefore, the increment of the relative displacement  $Z$  influences the harvested power, which represents the quantity to improve, as shown in Figure 26.

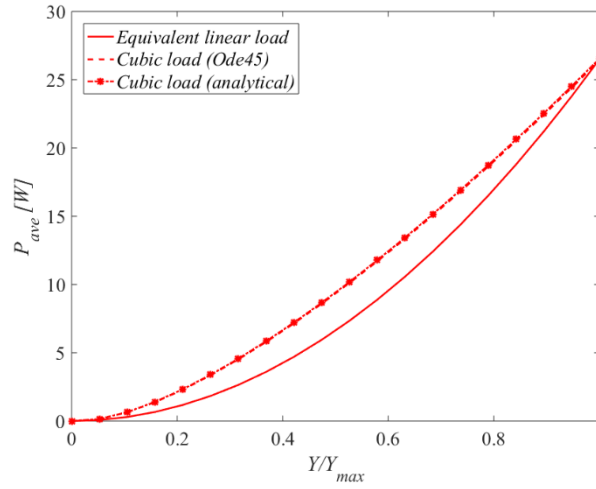


Figure 26: Level curves of the average harvested power  $P_{ave}$  for linear (solid line) and cubic (dashed line) energy harvesters as a function of the normalised input amplitude  $Y/Y_{max}$  where  $m=1kg$ ,  $k=4\pi^2$ ,  $c_m=0.2Ns/m$ ,  $R_{l,eq}=0.185Ns/m$ ,  $R_{nl}=1.37V^3/A$ ,  $Y_{max}=0.246m$  – dashed-dotted line with star markers is referred to the analytical solution obtained by the harmonic balance method

The deliberate introduction of a cubic electric damping allows one to improve the harvested power. The cubic nonlinearity enlarges all the dynamic range of performance and, for example, it can be seen that when  $Y/Y_{max}=0.6$ , the harvested power increases about 3W with respect to the linear device.

### 3.7 Effect of parasitic friction

As aforementioned in section 3.1, the parasitic friction is another aspect to consider when designing an electromagnetic energy harvester, and its effect on the harvested power is one of the novel contributions of the thesis [49]. Only static friction will be considered here. Static friction is present in devices, which work based on a conversion mechanism of motion, such as ball screw or rack and pinion [23]. In this work, the source of friction is represented by the gearbox, which is usually adopted in electromagnetic generator to increase the output voltage, as will be described in details in Chapter 5. Since static friction can influence the experimental results (as it will be presented in Chapter 6), it is worth to investigate its effect on the dynamics and the harvested power.

The mathematical formulation of the complete model, which considers also the static friction, was presented in section 3.2. The complete nonlinear model in the frequency domain is described using equation (3.16).

Assuming a static friction coefficient  $f_s=1N$ , the linearization leads to equation (3.31). The friction force is now added to the equation of motion, but the definition of equivalent linear load does not change because friction is dissipative and cannot be included in the definition of equivalent load.

However, the relative transmissibility will change in frequency domain according to equation obtained by using the harmonic balance method.

$$\frac{Z}{Y_{max}} = \frac{m\omega^2}{\sqrt{\left(k - m\omega^2\right)^2 + \left(c_m\omega + \frac{3}{4} \frac{K_t^4 \omega^3 Z^2}{R_{nl}} + \frac{4f_s}{\pi Z}\right)^2}} \quad (3.34)$$

The difference between equation (3.19) and equation (3.34)) is highlighted in Figure 27. At low levels of  $Z$ , the equivalent load is small, because the friction dominates the dynamics. Therefore, the harvester behaves in a nonlinear manner. However, at high levels of  $Z$ , the friction is overcome by the cubic damping, which has more influence at high input level. Consequently, the load tends to achieve the same value and the friction becomes almost negligible.

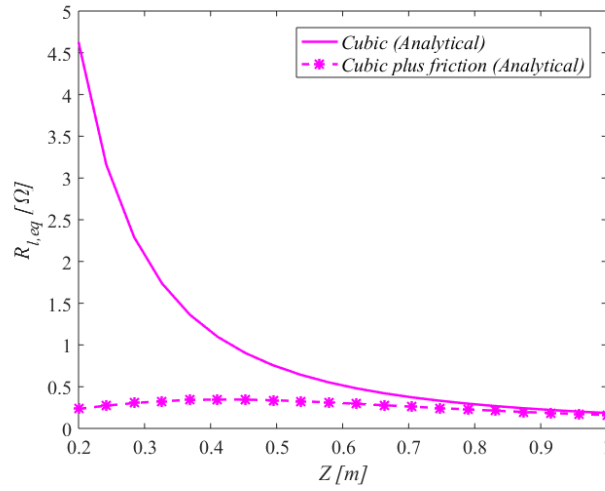


Figure 27: Equivalent load  $R_{t,eq}$  as a function of the relative displacement  $Z$  at resonance - the black dotted line is referred to the cubic damping, the black solid line with x markers is referred to the combination of cubic and friction

The numerical solution is obtained from Simulink where the friction has been model by using the hyperbolic tangent in which the coefficient of the angle is set equal to 1000. This causes the hyperbolic tangent function to be very similar to the sign function but still continuous. The hyperbolic tangent is one of the most used model to simulate static friction [55].

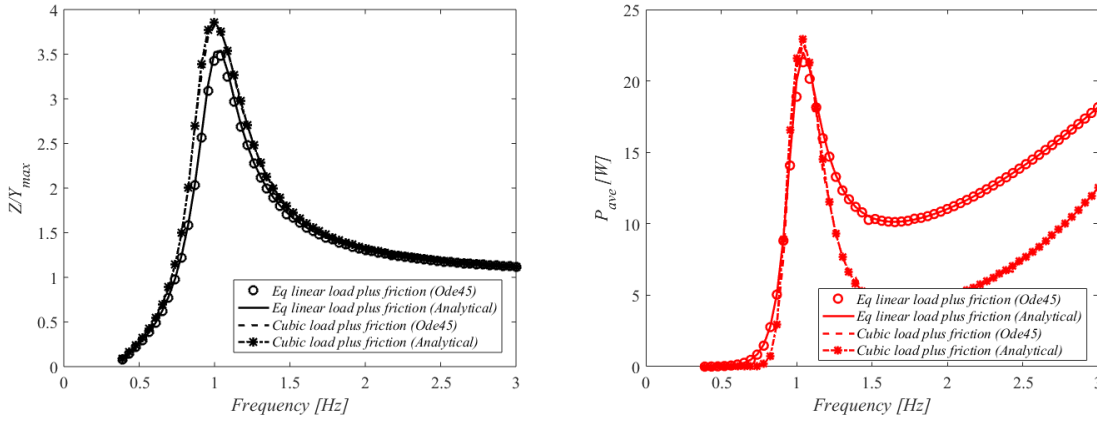


Figure 28: Relative transmissibility (left) and average harvested power (right) as a function of the frequency for linear (solid black line) and cubic (dash black line) energy harvesters where  $m=1kg$ ,  $k=4\pi^2$ ,  $c_m=0.2Ns/m$ ,  $f_s=1N$ ,  $R_{l,eq}=0.185Ns/m$ ,  $R_{nl}=1.37V^3/A$ ,  $Y_{max}=0.246m$  – dashed dotted line with star markers is referred to the analytical solution obtained by the harmonic balance method

The static friction, as any source of damping, affects the frequency response at the natural frequency. Comparing Figure 28(left) with Figure 20 and Figure 28(right) with Figure 22, it can be seen that the amplitude of the relative transmissibility and the average harvested power are reduced at resonance. Also, in Figure 28 (both left and right), the cubic harvester is less affected by the friction and it presents a higher harvested power at resonance. As aforementioned, the friction is not part of the equivalent load because it is dissipative. This causes the response and the harvested power of the cubic and the equivalent linear systems to be different at resonance. It seems that by adding the same amount of static friction to both systems, the cubic damping is less affected and the power is larger compared to the equivalent linear harvester. It is also remarkable that the error between the numerical and the analytical solutions are very small, which means that the higher harmonic components are almost negligible and the solutions are stable. In particular, by studying the effect of the friction at resonance, equation (3.31) and equation (3.32) modify as follows:

$$Z = \left( m\omega_n^2 Y - \frac{4f_s}{\pi} \right) \frac{1}{\omega_n \left( c_m + \frac{K_t^2}{R_{l,eq}} \right)} \quad (3.35)$$

, for the linear load, and

$$\frac{3}{4}c_3\omega_n^3 Z^3 + c_m\omega_n Z + \frac{4f_s}{\pi} - m\omega_n^2 Y = 0 \quad (3.36)$$

, for the cubic load. In Figure 29, the level curves obtained by equation (3.35) and equation (3.36) are shown.

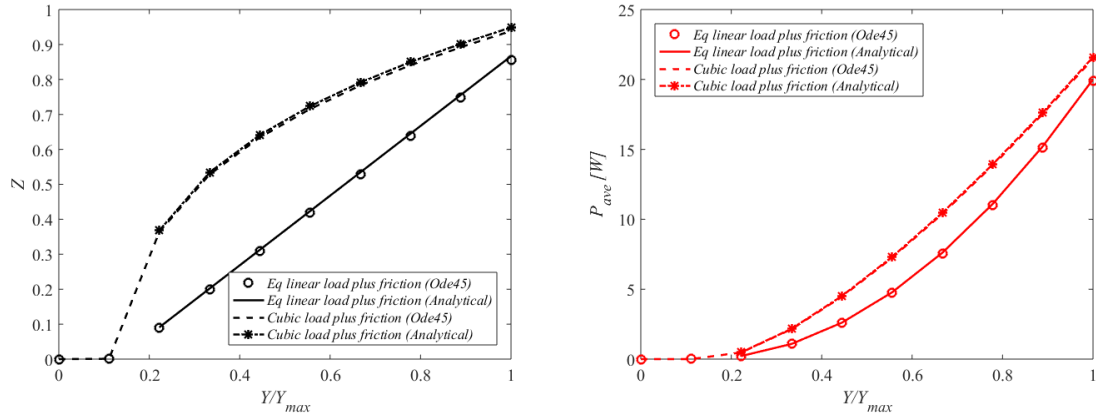


Figure 29: Level curves of the relative displacement (left) and average harvested power for (right) linear (solid line) and cubic (dashed line) energy harvesters as a function of the normalised input amplitude  $Y/Y_{max}$  where  $m=1kg$ ,  $k=4\pi^2$ ,  $c_m=0.2Ns/m$ ,  $f_s=1N$ ,  $R_{l,eq}=0.185Ns/m$ ,  $R_{nl}=1.37V^3/A$ ,  $Y_{max}=0.246m$  – dashed-dotted line with star markers is referred to the analytical solution obtained by the harmonic balance method

As shown in Figure 29, friction produces a general reduction of power in entire dynamic range of performance when compared with frictionless systems. However, the effect of friction seems to be stronger in the linear system than in cubic system. At the maximum level  $Y/Y_{max}=1$ , the cubic load provides more power than a linear load. However, as the input level decreases, the effect of friction becomes remarkable. Consequently, stiction takes place and the response  $Z$ , and so the power, drops to zero even if the input level is still positive. This can be noticed in Figure 29(left). At  $Y/Y_{max}=0.1$ , the relative displacement equals zero. It can also be noticed that at  $Y/Y_{max}=0.2$ , the analytical solutions interrupt because no real positive solution is obtained from equation (3.35) and equation (3.36) below that level.

According to the numerical analyses, it can be concluded that the cubic load produces a general improvement of the performance with respect to the linear devices also in presence of friction, which provokes a general reduction of power especially at low input levels.

### 3.8 An alternative approach: the level-dependent load

In Section 3.7, the advantage of a cubic electric damping was discussed and compared to linear load. To synthesize a cubic load, it is necessary to implement a controller, which is able to supply a value of electric load  $R_l$  such that the current through the coil is proportional to the third power of the voltage for any input level. However, although it was demonstrated that a cubic load can be a promising solution, it is not the only strategy.

Another approach was proposed in [56]. The authors investigated an inverse design of nonlinearity in an energy harvesting device to achieve the optimum load condition. When the energy harvester is excited above its physical limit, the relative displacement is kept at the maximum level by adjusting

the value of the electric load. This implies that the load depends on the input, especially at high levels. The equation of motion can be written as:

$$m\ddot{z} + \left( c_m + \frac{K_t^2}{R_l(Y)} \right) \dot{z} + kz = m\omega^2 Y \sin(\omega t + \varphi) \quad (3.37)$$

, where  $R_l(Y)$  is the level-dependent shunt load, and the friction has been neglected for simplicity. At the natural frequency, the amplitude of the relative displacement can be computed as,

$$Z = \frac{m\omega_n Y}{c_m + \frac{K_t^2}{R_l(Y)}}. \quad (3.38)$$

For each level of excitation, equation (3.38) states that the shunt load  $R_l(Y)$ , is adjusted such that the desired displacement  $Z$  is achieved. For example, when  $Y=Y_{max}$ , to reach the maximum throw  $Z=Z_{max}$  the load should be  $R_l(Y_{max})=0.185\Omega$ . The load is then a function of the input level  $Y$  as:

$$R_l = \frac{K_t^2 Z_{max}}{m\omega_n Y - c_m Z_{max}}. \quad (3.39)$$

If it is assumed that the optimum load  $R_{lopt}$  is larger than that necessary to limit the relative displacement at the maximum input, thus  $R_{lopt} > R_l$ , then the variable shunt load can be tuned, such that the maximum throw is always achieved, for each level below the  $Y_{max}$ , and the device operates at the optimum conditions. A reduction of input level is compensated by a reduction of the electrical damping (when the load increases the damping reduces) so that the relative displacement is always maximal. This compensation proceeds until the shunt load is equal to the optimum load computed by equation (3.30). Then, it is set up to constant, and the response decreases linearly with the input level, as described in equation (3.38). In Figure 30, the variable shunt load is plotted as a function of the input level. It can be seen that, as the input level reduces, the load has to increase to reduce the damping so that  $Z=Z_{max}$ . When the optimum load is achieved,  $R_{l,opt}$ , then the shunt load is maintained as a constant, because a further growth of load would cause a reduction of power according to Figure 23.



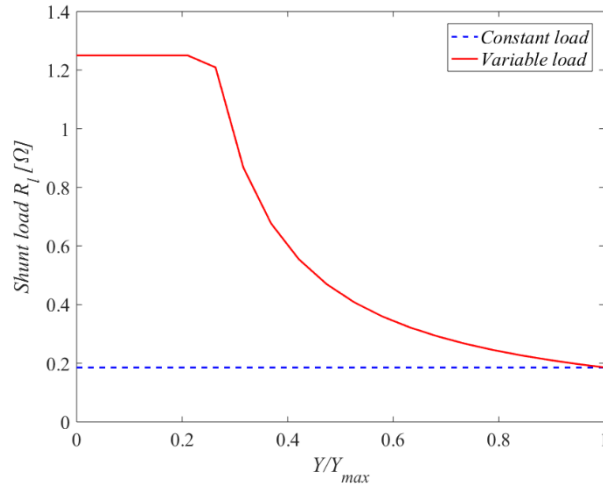


Figure 30: Shunt load  $R_l$  as a function of the normalised input amplitude  $Y/Y_{max}$  at resonance - the blue dashed line is referred to the linear device, the red solid line is referred to the level-dependent load – the load  $R_l$  reduces linearly with  $Y/Y_{max}$  until the optimum value is achieved

Practically, the implementation of a level dependent can be done by synthesising a bilinear shunt. In Figure 31, the ratio between the amplitude of the shunt damping force ( $\omega Z K_t^2/R_l$ ) and the amplitude of the relative velocity is shown.

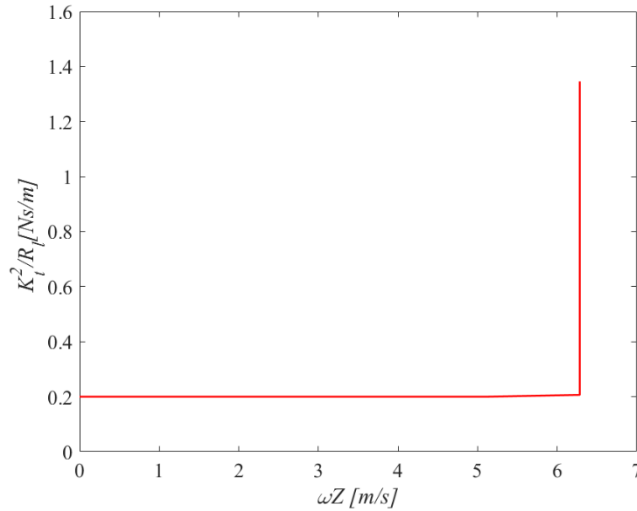


Figure 31: Ratio between the amplitude of the shunt damping force and the amplitude of the relative velocity as a function of the amplitude of the relative velocity

For a constant input level  $Y$ , the system is linear because  $R_l$  only varies with  $Y$ , therefore, the describing function, which is the electric damping force over the relative velocity is constant. The electric damping force remains constant, until the relative velocity reaches the limit of  $2\pi$  m/s, which corresponds to the maximum throw of  $1m$  at  $1Hz$ . The proposed strategy allows one to keep the maximum throw, and operate at the best conditions, when the current value of load does not match with the optimum value.

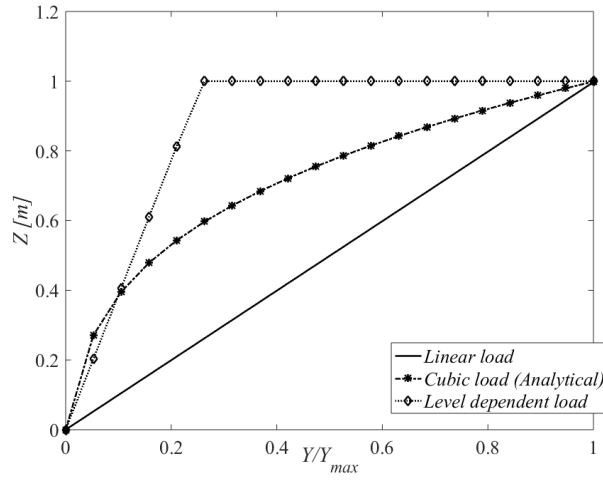


Figure 32: Level curves of the relative displacement  $Z$  for linear (solid line), cubic (dashed line) and level-dependent load (dotted line) energy harvesters as a function of the normalised input amplitude  $Y/Y_{max}$  where  $m=1kg$ ,  $k=4\pi^2$ ,  $c_m=0.2Ns/m$ ,  $R_{l,eq}=0.185Ns/m$ ,  $R_{nl}=1.37V^3/A$ ,  $Y_{max}=0.246m$  – dashed-dotted line with star markers is referred to the analytical solution obtained by the harmonic balance method

Clearly, operating at the maximum throw for different input levels, produces benefits in terms of power in the entire dynamic range, as the power is proportional to the square of the relative displacement, as obtained from equation (3.24). In Figure 32, the linear harvester is compared with the proposed strategies, such as the cubic and the quasi-linear harvesters. The nonlinearities, in the form of cubic load or level-dependent, enhance the response of the system, and increase the dynamic range. An adjustable shunt load, namely the level-dependent model, shows the largest relative displacement. Only at low levels ( $Y/Y_{max} < 0.12$ ) the cubic load produces a higher response with respect to the level-dependent model.

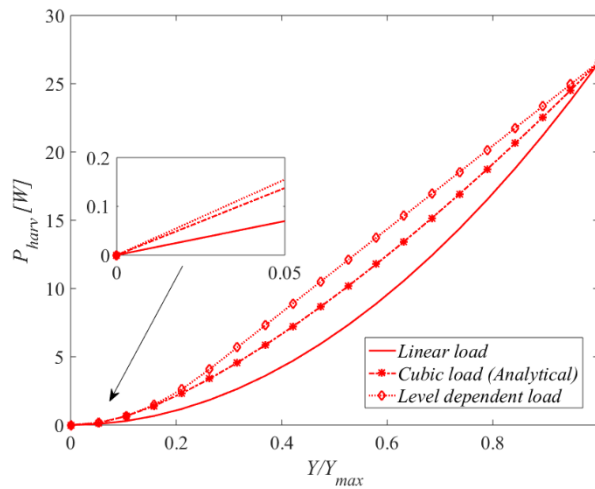


Figure 33: Level curves of the average harvested power  $P_{ave}$  for linear (solid line), cubic (dashed line) and level-depended load (dotted line) energy harvesters as a function of the normalised input amplitude  $Y/Y_{max}$

where  $m=1\text{kg}$ ,  $k=4\pi^2$ ,  $c_m=0.2\text{Ns/m}$ ,  $R_{l,eq}=0.185\text{Ns/m}$ ,  $R_{nl}=1.37\text{V}^3/\text{A}$ ,  $Y_{max}=0.246\text{m}$  – dashed-dotted line with star markers is referred to the analytical solution obtained by the harmonic balance method

As the nonlinear arrangements produce a larger response, it is expected the average harvested power to improve. Reminding that, the average harvested power depends only on the square of the relative displacement (for the linear harvesters), or the fourth power of the relative displacement (for the cubic harvester), in Figure 33, the benefits of the nonlinear strategies are evident. The level-dependent model generates the highest performance also at low level, as shown in the zoomed figure, and enlarges the dynamic range of performance. The cubic load is less effective than a level-dependent load; however, it represents a good improvement with respect to the linear device.

### 3.9 Summary

The aim of this chapter was to analyse the response of an electromagnetic energy harvesting device subjected to sinusoidal excitation. The energy harvester is assumed to have a constraint on the maximum relative displacement, which is limited by the size of the device and the available volume. It has been shown that the deliberate introduction of a nonlinear electric damping enlarges the dynamic range of performance and increases the harvested power. In particular, two different strategies have been proposed to obtain a higher performance, such as a cubic damping and a level-dependent load. The nonlinear arrangements, namely the cubic damping and the level-dependent damping, produce a beneficial effect on the response with respect to linear devices, and, as a consequence, the average harvested power increases. The level-dependent strategy consists in adjusting the electric load according to the input so that the energy harvester operates always at its maximum relative displacement unless the optimum load condition is achieved. In this case, the electric load is maintained as a constant and the harvester behaves linearly. The cubic electric damping can be obtained synthesising a nonlinear electric load, such that the current flowing through the coil is a cubic function of the voltage. Among these two strategies, it has been shown that the level-dependent load provides more harvested power with respect to the cubic damper.

Also, the effect of the static friction has been investigated, since it represents a common source of loss, especially in those mechanisms that are coupled with electromagnetic generators, as it will be presented in Chapter 6. Assuming to have a limitation on the maximum throw, the presence of friction generates a reduction of the response at the natural frequency. This provokes a general reduction of the average harvested power. However, it has been demonstrated that the friction affects the dynamics mainly at low input levels, while at high input levels it can be neglected.

## Chapter 4: Nonlinear damping in randomly-excited energy harvesting device

### 4.1 Introduction

As mentioned in Chapter 2, the ambient excitation has several forms; the input can be characterised by a very narrow frequency bandwidth, which allows the assumption of harmonic excitation. Nevertheless, many excitations are of a stochastic nature and is broadband, such as the signal of a rough road [57], and, therefore, the harmonic input does not represent a reliable model. The reference model for broadband input is called Gaussian white noise, and will be described in details in the next sections. Some other signals are instead bandlimited, such as the acceleration detected during an earthquake [58], or the vertical displacement due to the sea waves [23,43]; in these cases, the input noise is coloured. The following chapter focuses on the effects that such inputs, namely white and coloured noise, have on the nonlinear and the linear energy harvesting device.

### 4.2 Theory of random processes

A random (or stochastic) process is an infinite indexed collection of random variable  $\{X(t): t \in T\}$ , defined over a common probability space. The index  $t$  is usually time, but it can also be a spatial dimension, an example is the rain-on-the-the-roof excitation, where the autocorrelation function  $R_w(x, t)$  defines a random process where the forces are uncorrelated white noise with the same power spectral density in time and space [59]. Moreover, one can also consider the outcome of the random realisation (or experiment) as a variable  $\zeta$ , and, consequently, the random process can be viewed as a function of two variables, thus  $X(t, \zeta)$ . The random process  $X$  is often denoted with a capital letter as the ‘ensemble’ of all possible realisations  $\{x_i(t)\}$ . Each realisation is termed as sample function and is denoted by lowercase letters. A random variable is said to be stationary if all its statistical moments do not vary with time. Stationary processes are the main class of random processes considered in practice. From the measure prospective, in practical situations one usually does not have access to all the sample realisations. Therefore, it is assumed that the process is ergodic, which means that all the statistical characteristics of the process can be inferred by a single realisation averaging over the time. For a stationary and ergodic process, the so-called autocorrelation function can then be introduced as:

$$R_w(\tau_1, \dots, \tau_{k-1}) = \lim_{N \rightarrow \infty} \frac{1}{2N} \int_{-N}^N X(t)X(t - \tau_1) \dots X(t - \tau_{k-1}) dt \quad (4.1)$$

, where  $\tau$  is the time differences/lag and  $N$  is finite, because in practice only finite data records are available.

Two important parameters of a stationary and ergodic process, are the power spectral density (*PSD*) (generally denoted as  $S(j\omega)$ ), which is defined as the Fourier transform of the autocorrelation function, as:

$$S_w(j\omega) = \int_{-\infty}^{\infty} R_w(\tau) e^{-j\omega\tau} d\tau \quad (4.2)$$

, and the probability density function (*PDF*). Assuming  $x(k)$  is a random variable of a realisation  $k$ , and  $x$  is a specific value of  $x(k)$ , the probability distribution function  $P(x)$  can be defined as:

$$P(x) = \Pr[x(k) \leq x] \quad (4.3)$$

, where  $P(-\infty) = 0$ ,  $P(+\infty) = 1$  and  $P(a) \leq P(b)$  if  $a \leq b$ . Assuming  $P(x)$  to be continuous, the *PDF* is defined as:

$$p(x) = \lim_{\Delta x \rightarrow 0} \left( \frac{\Pr[x < x(k) \leq x + \Delta x]}{\Delta x} \right) \quad (4.4)$$

, with the following properties:

$$p(x) \geq 0 \quad \int_{-\infty}^{+\infty} p(x) dx = 1 \quad P(x) = \int_{-\infty}^x p(\eta) d\eta \quad (4.5)$$

The first property says that the *PDF* is always positive; the second property states that the area under the *PDF* is equal to 1; the third property defines the probability function  $P(x)$  as the integral of the *PDF*. In the case of system with more variables, the joint probability density function (*JPDF*) can be used:

$$p(x_1, x_2) = \lim_{\substack{\Delta x_1 \rightarrow 0 \\ \Delta x_2 \rightarrow 0}} \left( \frac{\Pr[x_1 < x_1(k) \leq x_1 + \Delta x_1 \ \& \ x_2 < x_2(k) \leq x_2 + \Delta x_2]}{\Delta x_1 \Delta x_2} \right) \quad (4.6)$$

, where  $x_1$  and  $x_2$  are the state variables.

The *PSD* allows distinguishing between white and coloured noise, while the *PDF* classifies the shape of the probability distribution, such as Gaussian,  $\chi$ -squared, etc

### 4.3 Statistical moments

Before moving to the definition of the Gaussian white noise, which represents the reference signal when dealing with randomly excited dynamic systems, it is worth to briefly introduce a set of specific

quantitative measures that determine the probability distribution. These measures are called statistical moments, and are split into orders.

The zeroth moment is 1, as it represents the area under the *PDF*. The first moment is called *mean*  $\mu_x$ , and is defined as:

$$\mu_x = E[x_k(t)] = \int_{-\infty}^{+\infty} xp(x)dx \quad (4.7)$$

The second central moment, referred to the state variable  $x$ , is termed as *variance*  $\sigma_x^2$ , and is computed from:

$$\sigma_x^2 = E[(x_k(t) - \mu_x)^2] = \int_{-\infty}^{+\infty} (x - \mu_x)^2 p(x)dx \quad (4.8)$$

The square root of the variance is called *standard deviation*  $\sigma_x$ . In this thesis, the input signal will be assumed to have a zero mean, as it is the most common situation in practice. Therefore, the time domain response will always have zero mean, due to the stationarity assumption, and the mean square and the standard deviation coincide. The third and the fourth moments, respectively called skewness and kurtosis.

The state variable, namely  $x_1$  and  $x_2$ , of linear and nonlinear systems are characterised by different behaviour when subjected to a random input. In general, two random variables (or in this case, the state variables) are termed *statistically independent* if:

$$p(x_1, x_2) = p(x_1)p(x_2) \quad (4.9)$$

Moreover, the following definition of covariance for two variables can be considered:

$$C_{x_1x_2} = E[(x_1(t) - \mu_1)(x_2(t) - \mu_2)] \quad (4.10)$$

, where if  $x_1 = x_2 \Rightarrow C_{x_1x_1} = \sigma_{x_1}^2$  and if  $\mu_1 = \mu_2 = 0 \Rightarrow C_{x_1x_2} = R_{xy}(\tau)$ .

The covariance function is a measure of how much the two signals look like each other. An estimation of this similarity is given by the following correlation coefficient  $\rho_{x_1x_2}$ :

$$\rho_{x_1x_2} = \frac{C_{x_1x_2}}{\sigma_{x_1}\sigma_{x_2}} \quad (4.11)$$

, where  $-1 \leq \rho_{x_1x_2} \leq +1$ . If the correlation coefficient is zero, the two variables are defined as *uncorrelated*. In general, if two variables are statistically independent, they are also uncorrelated, but the reverse does not apply. The reverse applies only in the case of Gaussian distribution.

The reason is that, for a nonlinear system, a Gaussian input does not imply a Gaussian output. In the next section, the assumption of Gaussian white noise input will be analysed with more attention.

#### 4.4 Gaussian white noise

Gaussian white noise is a stationary and ergodic random process with zero mean, in which any pair of times are identically distributed and statistically independent (thus, also uncorrelated). Its success is due to the fact that, in many applications, such as acoustics, electronics and structural dynamics, this type of model describes well the dynamics of the process. There is also a practical reason behind the use of this model. A Gaussian distribution is completely described by second order statistics (mean and variance), which are relatively easy to measure. The *PDF* of a Gaussian white input is shown in Figure 34. It can be highlighted that the odd-order autocorrelation functions of a zero-mean Gaussian process (white or coloured) are zero.

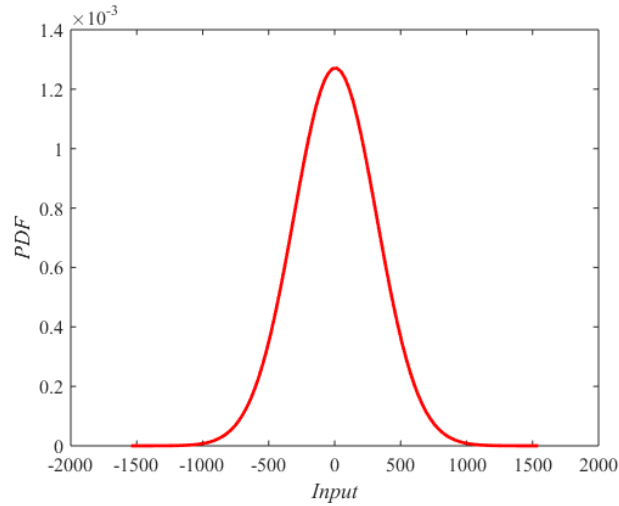


Figure 34: Example of a *PDF* of a Gaussian white input

The autocorrelation function of a *Gaussian white noise* is defined as:

$$R_w(\tau) = S_w \delta(\tau) \quad (4.12)$$

, where  $\delta(\tau)$  is the delta Dirac function, and  $S_w$ , which is expressed in  $D^2/Hz$ , is the one-sided *PSD* of the input. Hereafter, the quantity  $D$  is assumed to be the input acceleration at the base of the energy harvesting device. The term white derives from the fact that the *PSD* is constant over all the frequency range; even though this simplifies the analytical calculations, the Nyquist theorem limits the bandwidth and the assumption of white noise is not valid. In practise, Gaussian white noise is not physically realisable, because it would have infinite variance. An example of *PSDs* of Gaussian white and coloured noise are given in Figure 35.

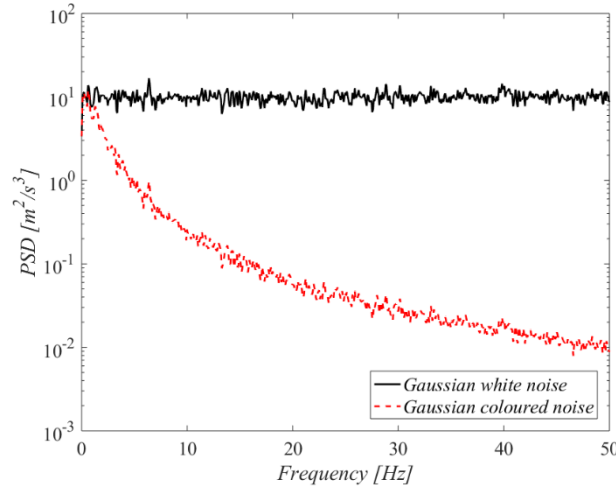


Figure 35: Examples of  $PSDs$  of Gaussian white (solid black line) and coloured (red dash line) noise

Another distinction is between additive and multiplicative Gaussian white noise. If the input depends on the state variables, then one refers to multiplicative Gaussian white noise, otherwise the signal is called additive. This thesis work only deals with additive Gaussian white noise.

## 4.5 Equivalent linearization method

In Chapter 3, the energy harvester with cubic load was studied by using the harmonic balance method to obtain an analytical approximate solution. The equivalent linear load is a function of the input and, in weakly nonlinear and slightly damped structures, the harmonic balance method approximates the nonlinear response at the fundamental frequency with reasonable accuracy. If the input is not harmonic, but broadband, no simple interpretation of the harmonics is possible, because the energy is spread over a wider bandwidth. The development of approximate analytical techniques for the estimation of the response of nonlinear systems subjected to random excitation has attracted the interest of researchers in the last decades. The importance of this topic stems from the fact that when structures are subjected to random inputs, for example sea wave action, earthquake, the response will be random with a nonlinear nature. Among these approximate techniques, the most popular ones are: (i) statistical equivalent linearisation or, in general, Gaussian closure methods [52,53], (ii) non-Gaussian closure methods [62,63], (iii) Fokker-Planck-Kolmogorov equation [35,64] and (iv) Wiener-Hermite series expansion [65]. In this thesis, only the statistical equivalent linearisation technique will be applied. This method is based on the technique of equivalent linearisation introduced by Krylov and Bogoliubov [66], for the study of nonlinear system subjected to deterministic input. The method has been then extended to random input by Booton [67] and Caughey [61]. The concept of the equivalent linearisation method is to replace the nonlinear system by an optimal linear substitute, which can be solved by using an analytical approach.



The assumption of the equivalent linearisation method refers to the probability distribution of the input, which is Gaussian. The importance of the Gaussian assumption from the mathematical and practical point of view was pointed out in Section 4.4. In terms of frequency contents, the input can be both white and coloured and the method applies to both cases. A coloured input is considered as the output of an analogue linear filter, which is subjected to a white noise input. Unlike other methods such as the Fokker-Planck-Kolmogorov equation, the equivalent linearisation works with a much wider class of nonlinearity. For example, it applies to nonlinearities, which depend on both displacement, velocity and acceleration; also nonlinearities associated with self-oscillatory systems can be dealt with this method. In addition, past-dependent (hysteresis) and asymmetric nonlinearities can also be solved with this method.

Recalling equation (3.1), we have

$$m\ddot{x} + c_m\dot{x} + \frac{K_t^4}{R_{l,nl}}x + kz = m\ddot{u}(t) \quad (4.13)$$

, where the friction terms is neglected in this chapter. It is assumed that the motion of the base is random, and the base acceleration is approximated as a stationary white noise, so that

$$E[\ddot{u}(t)\ddot{u}(t+\tau)] = S_w\delta(\tau) \quad (4.14)$$

, where,  $S_w$  is the one-sided auto power spectral density of the input acceleration. The input acceleration is assumed to have a zero mean.

As aforementioned, the method consists of replacing the nonlinear term with an equivalent linear term that is optimal in some statistical sense, we have

$$m\ddot{x} + c_m\dot{x} + \frac{K_t^2}{R_{l,eq}}x + kz = m\ddot{u}(t) \quad (4.15)$$

, for nonlinear damping. To compute the equivalent load, there are different approaches that lead to the same result: (i) error minimisation, (ii) series truncation, and (iii) power balance [68]. Hereafter, the first approach is used. To compute the equivalent load  $R_{l,eq}$ , the mean square error between the replaced and the replacing terms should be minimised. In general, the error can be a function of displacement, velocity, acceleration, or time (if the system is nonstationary). As in this study, the acceleration and the displacement are linear and the input is stationary, the error  $e$  only depends on the velocity,

$$e(\dot{x}) = \frac{K_t^4}{R_{l,nl}}\dot{x} - \frac{K_t^2}{R_{l,eq}}\dot{x} \quad (4.16)$$

By definition, the mean square error can be obtained as

$$E[e^2] = \lim_{T \rightarrow \infty} \frac{1}{2T} \int_{-T}^T e^2(\mathfrak{z}) dt \quad (4.17)$$

The goal is to compute the value of  $R_{l,eq}$  such that the mean square error is minimised. Therefore, it is imposed,

$$\frac{\partial E[e^2]}{\partial R_{l,eq}} = 0 \quad (4.18)$$

, as the integrand in equation (4.17) is continuous, the expectation and the derivative operators can be exchanged,

$$E\left[\frac{\partial e^2}{\partial R_{l,eq}}\right] = E\left[-\frac{1}{R_{l,eq}} \mathfrak{z}^2 + \frac{K_t^2}{R_{l,nl}} \mathfrak{z}^4\right] = 0 \quad (4.19)$$

Therefore, the equivalent load is,

$$R_{l,eq} = \frac{R_{l,nl}}{K_t^2} \frac{E[\mathfrak{z}^4]}{E[\mathfrak{z}^2]} \quad (4.20)$$

Upon studying equation (4.20), it can be observed that both expectations need to be evaluated. However, the *PDF*, which is unknown, is required to calculate the equivalent load. If a nonlinear system is excited by a Gaussian input, then the response is not Gaussian. Nevertheless, as part of the Gaussian closure methods, the equivalent linearisation assumes that the probabilistic distribution of the response of a nonlinear system subjected to a Gaussian input is still Gaussian,

$$p(\mathfrak{z}) \approx p_{eq}(\mathfrak{z}) = \frac{1}{\sqrt{2\pi\sigma_{\mathfrak{z},eq}^2}} e^{-\left(\frac{\mathfrak{z}^2}{2\sigma_{\mathfrak{z},eq}^2}\right)} \quad (4.21)$$

, where  $p(\mathfrak{z})$  is the *PDF* of the velocity of the nonlinear system,  $p_{eq}(\mathfrak{z})$  is the *PDF* of the velocity of the linearised system and  $\sigma_{\mathfrak{z},eq}^2$  is the variance of the equivalent linear system. The variance of the velocity of a linear system (which is the equivalent in this case), can be computed in different ways, such as Fokker-Planck-Kolmogorov equation or Lyapunov equation. In Appendix I, the variance of displacement and velocity are derived by solving the Lyapunov equation. Therefore, for the equivalent linear system, the variance of the displacement is

$$\sigma_{z,eq}^2 = \frac{mS_w}{2\left(c_m + \frac{K_t^2}{R_{l,eq}}\right)\omega_n^2} \quad (4.22)$$

, the variance of velocity is instead,

$$\sigma_{\xi_{eq}}^2 = \frac{mS_w}{2 \left( c_m + \frac{K_t^2}{R_{l,eq}} \right)} \quad (4.23)$$

, which can be substituted at numerator into equation (4.20). The fourth-order expectation at the numerator becomes

$$E[\xi^4] = \frac{1}{\sqrt{2\pi\sigma_{\xi_{eq}}^2}} \int_{-\infty}^{+\infty} \xi^4 e^{-\left(\frac{\xi^2}{2\sigma_{\xi_{eq}}^2}\right)} d\xi \quad (4.24)$$

, which belongs to the class of Gaussian integrals. The Gaussian integral in equation (4.24) can be solved analytically (see Appendix II) and its solution is

$$E[\xi^4] = 3\sigma_{\xi_{eq}}^4 \quad (4.25)$$

In this result, the advantage of the Gaussian assumption is highlighted. All the higher-order statistical moments of a Gaussian variable can be expressed in terms of first and second order moments; in this specific case, a fourth-order moment can be obtained by squaring the variance  $(\sigma_{\xi_{eq}}^2)^2$  and multiplying by a factor of 3. The equation (4.20) becomes

$$R_{l,eq} = \frac{R_{l,nl}}{3K_t^2\sigma_{\xi_{eq}}^2} \quad (4.26)$$

, substituting equation (4.10), the equivalent linear load can be obtained as follows:

$$R_{l,eq} = \frac{1}{3} \frac{c_m R_{l,nl}}{mS_w K_t^2} + \frac{1}{2} \sqrt{\left( \frac{2}{3} \frac{c_m R_{l,nl}}{mS_w K_t^2} \right)^2 + \frac{8}{3} \frac{R_{l,nl}}{mS_w}} \quad (4.27)$$

, where only the positive solution has physical meaning. The relation between the nonlinear and the equivalent linear load for a white noise input is plotted in Figure 36.

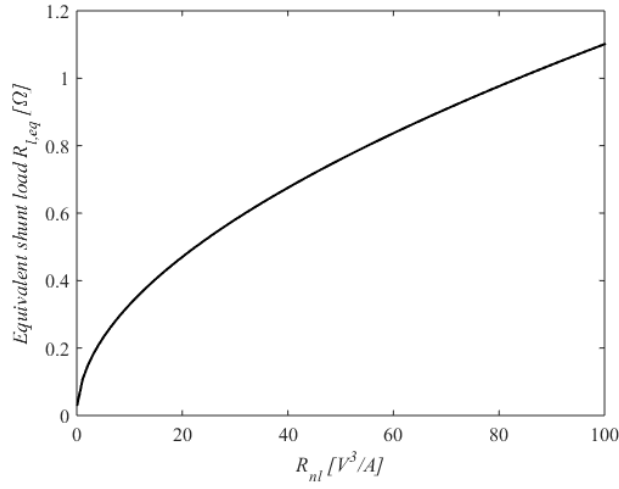


Figure 36: Equivalent linear load as a function of the nonlinear load – analytical result

The linearisation requires the load to be level-dependant, as shown in Figure 37, where the equivalent load is plotted with respect to the power spectral density of the input acceleration. Recalling equation (3.24), the average harvested power of the equivalent linear system can be written as:

$$P_{harv} = \frac{K_t^2}{R_{l,eq}} \sigma_{\ddot{x}}^2 \quad (4.28)$$

, which leads to

$$P_{harv} = \frac{m S_w K_t^2}{2(R_{l,eq} c_m + K_t^2)} \quad (4.29)$$

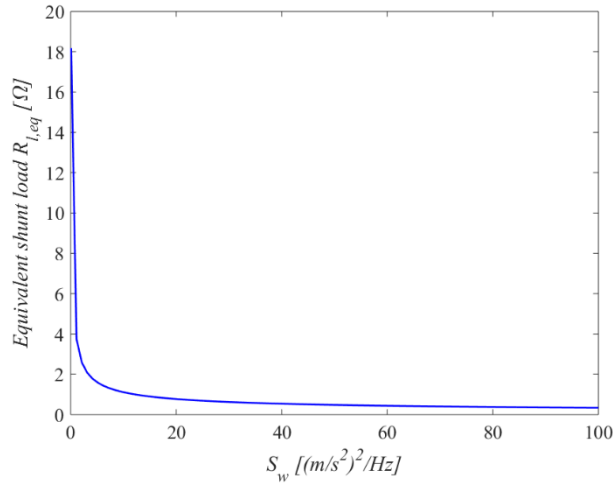


Figure 37: Equivalent electric load as a function of the power spectral density of the input acceleration—analytical result

In Chapter 3, to find the equivalent load it was imposed that the nonlinear and the equivalent linear need to have the same response  $Z$  at resonance when the input displacement was maximum. This

assumption was significant when the two systems were subjected to a variable input level, because the advantage of the nonlinearity can be observed.

In case of random input, it is not possible to find the equivalent load by imposing the same response, because the amplitude of the response is random. Therefore, the mean square has been used to obtain the equivalent load. Nevertheless, in practice, the mean square is somewhat abstract, in the sense that when a physical constraint has to be fixed, this is usually referred to the amplitude of the response (for a deterministic input) or the probability of the response (for a random input). In this case, the probability of the response is assumed to be lower than 1 meter, for the 95% of the samples. Therefore, the mean square is automatically defined, and in addition, is related to a physical quantity, thus the amplitude.

The simulations are run using a Matlab script, which recalls the solver *Ode4* (fourth-order with fixed step), which is written in *C* language. The choice of *Ode4* is due to the fact that the friction is neglected and it is not expected to have a sharp change in the solution, in which case a variable solver is more accurate (see Chapter 3). The use of *C* is due to its fast performance. To simulate a random white noise input, a high sampling frequency and large simulation time are required. As an example, a linear *Ode* was solved by running *Ode4* in both Matlab and *C*. The aim is to ensure that the results, obtained from Matlab Simulink and *C*, are the same. Also, the computational time is calculated to demonstrate the effectiveness of the use of *C*.

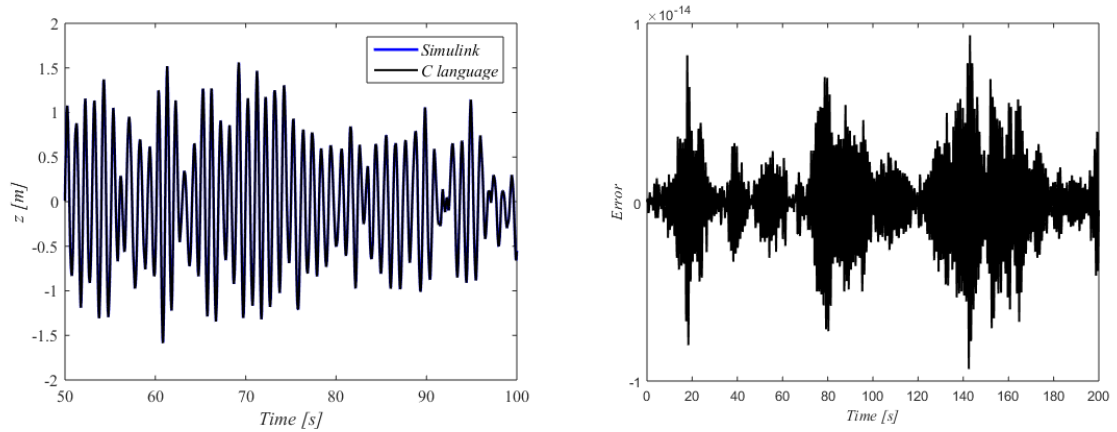


Figure 38: Displacement obtained from Simulink and *C* (left) and error (right) in time domain, where

$$m=1\text{kg}, c_m=0.2\text{Ns/m}, k=4\pi^2, K_t=0\text{N/A}, R_{nl}=0\text{V}^3/\text{A} \text{ (a)}, S_w=10 \text{ (m/s}^2\text{)}^2/\text{Hz} \text{ (b)}$$

From Figure 38, the response  $z$  (obtained from Simulink and *C*) and the error is defined as the difference between the responses computed with Simulink and *C*. The *C* model yields the same results as Simulink, but it performs about 13 times faster.

## 4.6 Constraint on the probability of the response

The simulation parameters are listed in Table 3.

Table 3: Parameters of the energy harvester

<i>Parameter</i>	<i>Value</i>
$m$ [kg]	1
$k$ [N/m]	$4\pi^2$
$c_m$ [Ns/m]	0.2
$K_t$ [N/A]	1.1
$R_{l,nl}$ [V <sup>3</sup> /A]	11
$\omega_n$ [rad/s]	$2\pi$
$S_{w,max}$ [(m/s <sup>2</sup> )/Hz]	130
$R_{l,eq}$ [ $\Omega$ ] (referred to $S_{w,max}$ )	0.34
$P(Z \leq lm)$	95%

The input acceleration is a broadband signal with a sampling frequency of 48 kHz and a constant PSD up to 24 kHz, as shown in Figure 39. Since the natural frequency is 1 Hz, such an input can be considered as white noise.

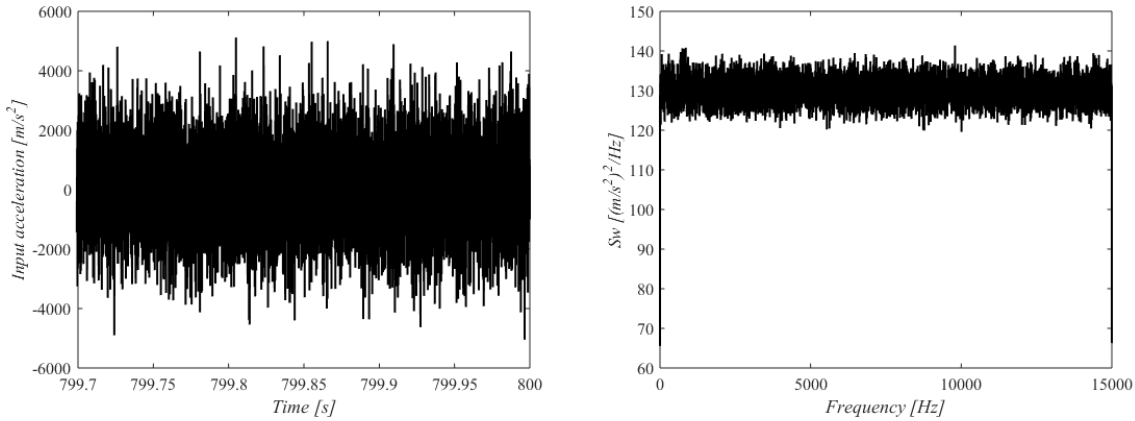


Figure 39: Input acceleration (left) and its PSD (right) used to obtain the equivalent load. For such an input the equivalent load is computed so that the mean square (or the probability that  $Z \leq lm$ ) of the linear and the nonlinear system is the same

To highlight the nonlinear behaviour, the parameters such as the input spectrum, the transduction coefficient and the nonlinear load are chosen so that the nonlinearity is strong enough to generate nonlinear effects. In Figure 40, the harvesting force, due to the nonlinear load, is plotted and compared to the force produced by the equivalent linear load. At the maximum input  $S_{w,max}$ , the degree of nonlinearity is high. This will cause the output not to be Gaussian. Consequently, the

equivalent linearization method, which is based on the assumption that the output of a nonlinear system is Gaussian, will not be an exact method, but it will yield an approximate solution for the mean square.

The harvesting force, associated with the equivalent linear load is:

$$f_{R_l} = \frac{K_t^2}{R_{l,eq}} \mathfrak{Z} \quad (4.30)$$

, while for the nonlinear device with cubic load is:

$$f_{R_l} = \frac{K_t^4}{R_{nl}} \mathfrak{Z}^3 \quad (4.31)$$

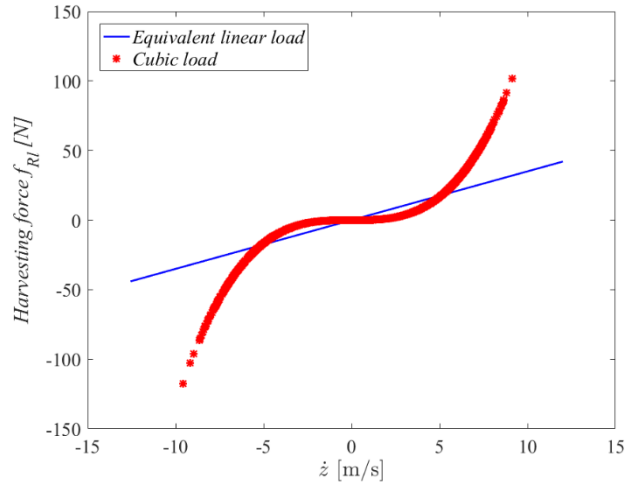


Figure 40: Harvesting force for the equivalent linear load (solid blue line) and cubic load (starred red markers) for  $S_w=S_{w,max}$

As aforementioned, imposing that the linear and the nonlinear systems have the same probability on the displacement (thus that  $Z \leq lm$ ), is equivalent to fix the mean square. The probability function and the *PDF* of the displacement are plotted in Figure 41.

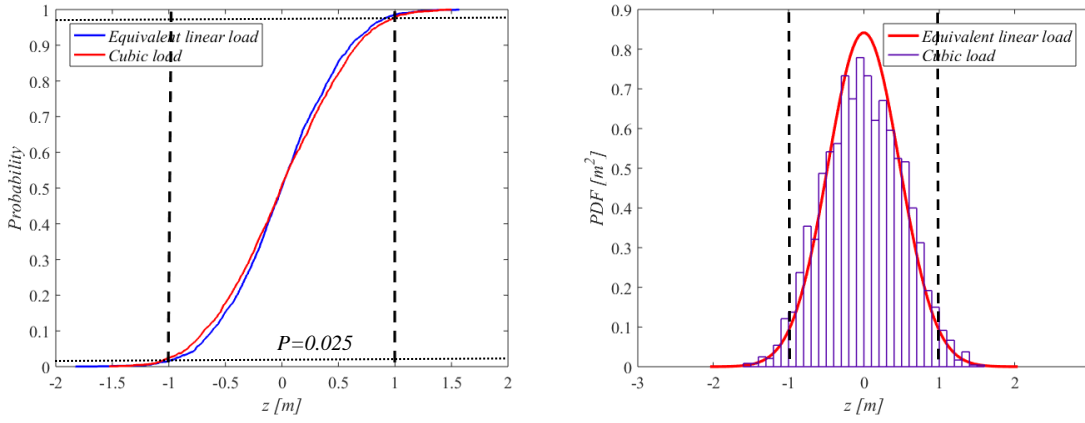


Figure 41: Probability function (left) of the displacement  $z$  and probability density function (right) for the simulation parameters indicated in Table 3 – the vertical dashed line indicate the constraint on the amplitude of  $z$ , the horizontal dotted line (left) indicate the lower and the upper limit of the probability such that the 95% of the sample satisfies the constraint

From the cumulative distribution in Figure 41(left), we can see that the nonlinear load and the equivalent linear load are complied with the constraint and this makes the amplitude of the response  $Z$  to be  $\leq 1m$  for the 95% of the samples. Nevertheless, if we look at the *PDF*, we can notice that the nonlinearity causes  $z$  to be non-Gaussian. Two characteristics can be noticed. First, the tails, which are described by the kurtosis (forth order central moment), are slightly different. In a Gaussian signal, the Kurtosis is  $3\sigma^4$  as can be seen from equation (4.25), however in a nonlinear system this is not valid. For the equivalent linear system, the kurtosis is  $0.15 m^4$ , while for the nonlinear system, the kurtosis is  $0.18 m^4$ , with a difference of 19%. The second difference can be found by observing the top of the distribution. The nonlinear distribution is more flat at the top and, consequently, non-Gaussian. This can be related to the fact that state variables are statistically correlated and, therefore, another method should be utilised such as equivalent non-linearisation [61,69,70] or non-Gaussian closure [62] to estimate the *PDF*, which does not assume the Gaussian property of the output. In particular, the equivalent non-linearisation method was introduced to estimate the probability density function of nonlinear systems. An example of this method is given in Appendix III. However, hereafter this method is not considered, because the main aim of the chapter is to compare the nonlinear and the equivalent linear load, and not finding a better statistical analytical solution.

The *PSD* of the state variables is plotted in Figure 42, where the analytical (equivalent linear load) and numerical (cubic load) are compared. This quantity is very important as it is strictly related to the harvested power as described in the next section.

After computing the equivalent load in equation (4.27), the *PSD* of the output velocity can be obtained as:

$$S_{\dot{z}}(j\omega) = |H_{eq}(j\omega)|^2 m^2 S_w \quad (4.32)$$



, where  $H_{eq}$  is the transfer function of the equivalent linear system referred to the relative velocity  $\dot{z}$  and is:

$$H_{eq}(j\omega) = \frac{j\omega}{-\omega^2 m + j\omega \left( c_m + \frac{K_t^2}{R_{l,eq}} \right) + k} \quad (4.33)$$

To obtain  $S_{zz}$  the numerator of equation (4.33) should be set to 1.

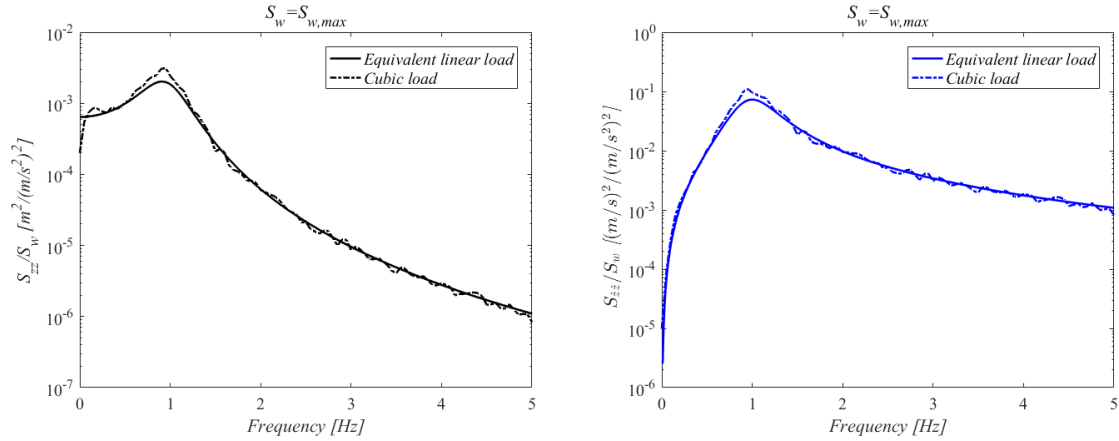


Figure 42: Power spectra of displacement (left) and velocity (right) for the cubic and the equivalent linear load where  $m=1\text{kg}$ ,  $c_m=0.2\text{Ns/m}$ ,  $k=4\pi^2$ ,  $K_t=1.1\text{N/A}$ ,  $R_{nl}=11\text{V}^3/\text{A}$ ,  $R_{l,eq}=0.34\Omega$ ,  $S_w=S_{w,max}$

At a first glance, it can be seen that the linear and the cubic system do not perfectly match at resonance, in Figure 42. The reason is that the equivalent linearisation is an approximate method and the approximation is as high as the nonlinearity increases. As shown in Figure 40, the cubic load, and consequently, the harvesting force, is set so that the nonlinear effect is strong. Therefore, it was expected that the cubic and the equivalent linear load provoke such a difference in the power spectral density. Equivalent linearisation method minimises the variance between the cubic and the equivalent linear load so that they are as close as possible, but if the nonlinearity is strong, the distribution is strongly not Gaussian and the error becomes larger. The equivalent linearisation underestimates the equivalent linear load (or in other words overestimates the damping), and in turn, the variance is underestimated too. In the level curves, shown in the section 4.8, it is expected that at the maximum input level  $S_{w,max}$  the variance of the equivalent linear system is smaller than the variance of the cubic system. In Appendix III another example is given in which the equivalent linearisation overestimates the damping when compared to the numerical nonlinear solution and the equivalent nonlinearisation method. As a consequence, the variance of the equivalent linear system is expected to be lower at the maximum input level  $S_{w,max}$  than the nonlinear system. Another important feature is that, although the nonlinearity is strong no super harmonics appear. The input signal is spread over the whole frequency domain and not at a single spectral linear, like in the harmonic case. Therefore, the effect of the odd harmonics, typical of the cubic load, is not visible. A broadband input tends to linearise

the system and to highlight the linear behaviour, even if the nonlinearity is strong, as shown in Figure 40.

Recalling the definition of autocorrelation function of the velocity  $\dot{z}$

$$R_{\dot{z}\dot{z}}(\tau) = E[\dot{z}(t)\dot{z}(t + \tau)] \quad (4.34)$$

and using equation (4.8), the autocorrelation function can be related to the mean square (or variance for a zero mean input) as follows

$$\sigma_{\dot{z}}^2 = R_{\dot{z}\dot{z}}(0) = E[\dot{z}^2(t)] \quad (4.35)$$

Moreover, the autocorrelation function can be obtained from the inverse Fourier transform of the power spectral density

$$R_{\dot{z}\dot{z}}(\tau) = \frac{1}{2\pi} \int_{-\infty}^{+\infty} S_{\dot{z}\dot{z}} e^{j\omega\tau} d\omega \quad (4.36)$$

Combining equation (4.35) and (4.36) and considering the one-sided *PSD*

$$\sigma_{\dot{z}}^2 = R_{\dot{z}\dot{z}}(0) = \frac{1}{\pi} \int_0^{+\infty} S_{\dot{z}\dot{z}} d\omega \quad (4.37)$$

Imposing the same variance as equivalent condition is equivalent to assume that the area below the power spectral density of the velocity is the same. This is the reason of expecting a different variance at the maximum input between cubic and equivalent linear system. This will be highlighted in the level curves in Section 4.8.

The power spectral density of the output velocity plays a fundamental role in the definition of the average harvested power of the equivalent linear system. For cubic and the equivalent linear load, equation (3.26) and (3.24) are still valid. However, to compare them, it is convenient to express average harvested power of the equivalent linear system in the frequency domain so that an analytical expression can be found.

For any mechanical system, the cross-correlation between the force  $f$  (which can be damping or harvesting force) and velocity  $\dot{z}$  is defined as:

$$R_{f\dot{z}}(\tau) = E[f(t)\dot{z}(t + \tau)] \quad (4.38)$$

It is clear that when  $\tau=0$ , equation (4.38) coincides with the power harvested or dissipated as:

$$P_{ave} = R_{f\dot{z}}(0) = R_{\dot{z}f}(0) \quad (4.39)$$

, where the cross-correlation is now an even function. Since we are interested into the harvested power, only the contribution of the electric load is considered. Using the well-known Wiener-Khinchine formulas [71], equation (4.38) can be related to the power spectrum (and vice versa),

$$S_{f\dot{x}}(j\omega) = \int_{-\infty}^{+\infty} R_{f\dot{x}}(\tau) e^{-j\omega\tau} d\tau \quad (4.40)$$

in which,  $S_{f\dot{x}}$  is the cross power spectrum of the force and velocity and is a complex function. The cross-correlation is the inverse Fourier transform of the power spectrum, so

$$R_{f\dot{x}}(\tau) = \frac{1}{2\pi} \int_{-\infty}^{+\infty} S_{f\dot{x}}(j\omega) e^{j\omega\tau} d\omega \quad (4.41)$$

Combining equation 4.39 and 4.41, we have

$$P_{ave} = R_{f\dot{x}}(0) = \frac{1}{2\pi} \int_{-\infty}^{+\infty} S_{f\dot{x}}(j\omega) d\omega \quad (4.42)$$

. However, only the real part can be related to the dissipated or harvested power. In addition,  $S_{f\dot{x}}$  is even therefore,

$$P_{ave} = \frac{1}{\pi} \int_0^{+\infty} \text{Re}[S_{f\dot{x}}(j\omega)] d\omega \quad (4.43)$$

Equation (4.43) is valid for both linear and nonlinear systems. Nevertheless, for nonlinear load the integral should be solved numerically. An analytical expression for the cross spectrum can be obtained for the equivalent linear load. For the equivalent linear load, the cross-correlation between the harvesting force and the velocity is:

$$R_{f\dot{x}}(\tau) = \frac{K_t^2}{R_{l,eq}} E[\dot{x}(t)\dot{x}(t+\tau)] = \frac{K_t^2}{R_{l,eq}} R_{\dot{x}\dot{x}}(\tau) \quad (4.44)$$

Applying the Fourier transform, we have

$$S_{f\dot{x}}(\omega) = \frac{K_t^2}{R_{l,eq}} S_{\dot{x}\dot{x}}(\omega) \quad (4.45)$$

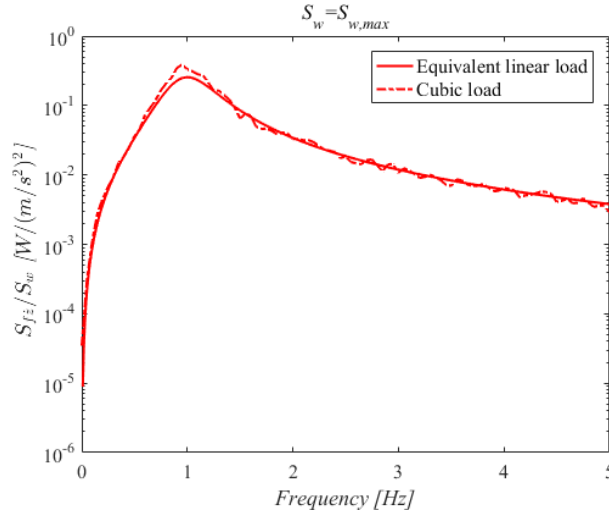


Figure 43: Cross spectrum of force and velocity for the cubic and the equivalent linear load where

$$m=1\text{kg}, c_m=0.2\text{Ns/m}, k=4\pi^2, K_t=1.1\text{N/A}, R_{nl}=11\text{V}^3/\text{A}, R_{l,eq}=0.34\Omega, S_w=S_{w,max}$$

The area below the cross spectrum, in Figure 43, corresponds to the power harvested, indeed, recalling equation (4.32) and (4.45) and substituting in equation (4.43), we have

$$P_{ave} = \frac{1}{\pi} \frac{m^2 S_w K_t^2}{2R_{l,eq}} \int_0^{+\infty} |H_{eq}(j\omega)|^2 d\omega \quad (4.46)$$

According to [72], the integral can be solved analytically. The average harvested power becomes:

$$P_{ave} = \frac{m S_w K_t^2}{2(R_{l,eq} c_m + K_t^2)} \quad (4.47)$$

Equation (4.47) coincides exactly with the average harvested power computed passing through the definition of variance in equation (4.28).

## 4.7 Upper bound and optimum load on the harvested power

Equation (4.47) has pointed out that the average harvested power of a device excited with a white input depends on the characteristics  $K_t$  of the generator, the load  $R_{l,eq}$ , the mass  $m$ , the mechanical damping  $c_m$  and the input level  $S_w$ . A remarkable breakthrough was achieved by Langley [41]. The author derived an analytical expression for the upper bound of the harvested power assuming no dissipation; in other words, the input power was entirely converted into harvested power. Assuming a Gaussian white noise input, Langley [41] demonstrated that

$$P_{ub} = \frac{m S_w}{2} \quad (4.48)$$

, where  $P_{ub}$  is the upper bound of the average harvested power.

The importance of this result relies on the generalisation that the author made to linear and nonlinear systems with single and multi-degrees of freedom. Equation (4.48) states that there exists an upper limit of the harvested power, which cannot be exceeded. Surprisingly, this limit does not depend on the damping but only on the input level and the mass of the system. However, this limit is practically impossible to measure due to the fact that the white noise is only a mathematical model and also that the output power of a mechanical system is hard to be measured. Numerically, the upper bound is impossible to achieve because the sampling for the numerical integration limits the frequency bandwidth. Nevertheless, the author showed that by increasing the sampling frequency, the output power converges to the analytical upper bound.

In the current case of study, the energy harvester is assumed to be affected by mechanical losses. Consequently, the average harvested power will be lower than the upper limit for any value of  $R_{l,eq}$ , as plotted in Figure 44. Nevertheless, to verify the validity of the analytical derivation, we can impose  $c_m=0$  in equation (4.47), which leads to equation (4.48).

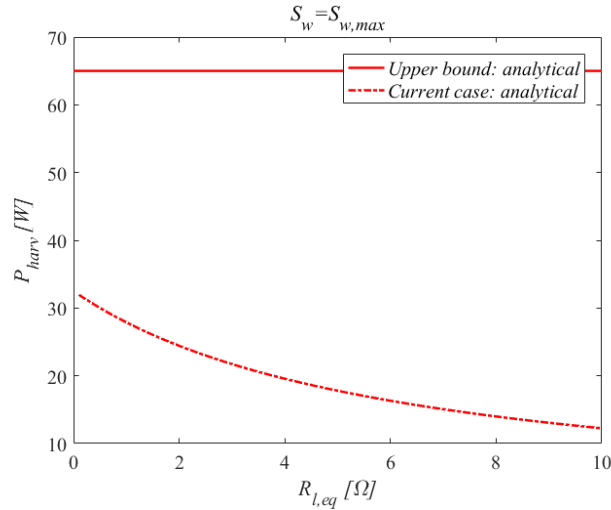


Figure 44: Average harvested power as a function of the electric load. The upper bound derived is indicated in blue solid line and assumes that all the input power is converted into harvested power; the solid dash dot line is the current case of study, in which a source of mechanical damping is introduced. If the electric load is zero, Langley's results are achieved

The limitation of the assumption of  $R_i=0$  (no electric internal dissipation in the generator) is evident. To obtain the optimum value of the load resistance, according to Chapter 3, the first derivative of the power is equal to zero:

$$\left. \frac{\partial P_{harv}}{\partial R_{l,eq}} \right|_{R_{l,eq} \geq 0} = -\frac{mS_w K_t^2 c_m}{2(R_{l,eq} c_m + K_t^2)^2} = 0 \quad (4.49)$$

, which corresponds to a hyperbole and is never verified (for any  $R_i > 0$ ). In other words, there is not an optimum load in this case. To highlight the importance of the assumption  $R_i = 0$ , we temporarily assume  $R_i = 0.1 \Omega$ , and consequently, the equation (4.47) becomes:

$$P_{harv} = \frac{m S_w K_t^2 R_{l,eq}}{2 \left( c_m + \frac{K_t^2}{R_{l,eq} + R_i} \right) (R_{l,eq} + R_i)^2} \quad (4.50)$$

Imposing (4.49), the optimum load can be calculated as

$$R_{l,eq} = \sqrt{R_i^2 + \frac{K_t^2 R_i}{c_m}} \quad (4.51)$$

For white noise, an optimum load only exists if an internal resistance is considered. Equation (4.51) states that if an internal resistance of  $0.1 \Omega$  is considered, then the optimum load would be  $R_{l,eq} = 0.78 \Omega$ , as confirmed analytically in Figure 45.

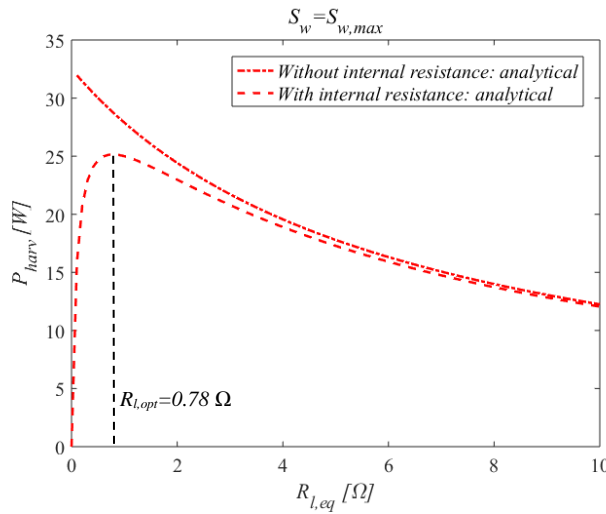


Figure 45: Average harvested power as a function of the electric load. Dashed red line is referred to the case  $R_i = 0$  and dashed dotted red line is referred to the case  $R_i = 0.1 \Omega$

For simplicity the internal resistance is not considered in this thesis because it is assumed that the voltage across the internal resistance is negligible compared to the voltage across the load resistance. The effect of the internal resistance is listed in Chapter 7 as part of future work.

## 4.8 Variation of the input level: level curves

According to what was made for the harmonic case, the current study focuses on the possible advantage that a nonlinear cubic load may have on the harvested power. To sum up, in Chapter 3 it was shown that when the input level decreases, assuming the excitation frequency is at the natural frequency of the energy harvester, the relative displacement of the nonlinear system increases when

compared to the linear counterpart. The reason is that by reducing the input level, the damping force produced by a cubic load is smaller than that produced by a linear load and consequently, the output displacement is larger. Therefore, the average harvested power improves, as it is proportional to the square of the output displacement.

The main difference here is that the device is not excited at a single spectral line, but the excitation is broadband and therefore, the energy spreads over all the frequency range. If the excitation is not at the fundamental component, as in the harmonic case (where if the fundamental component is excited all the odd higher harmonics of the cubic damping are also excited), then the nonlinear behaviour may not appear, as shown in Figure 42 and in Figure 43. To study the effect of a variable input level, it is assumed the input is set to a fifth of the maximum input level.

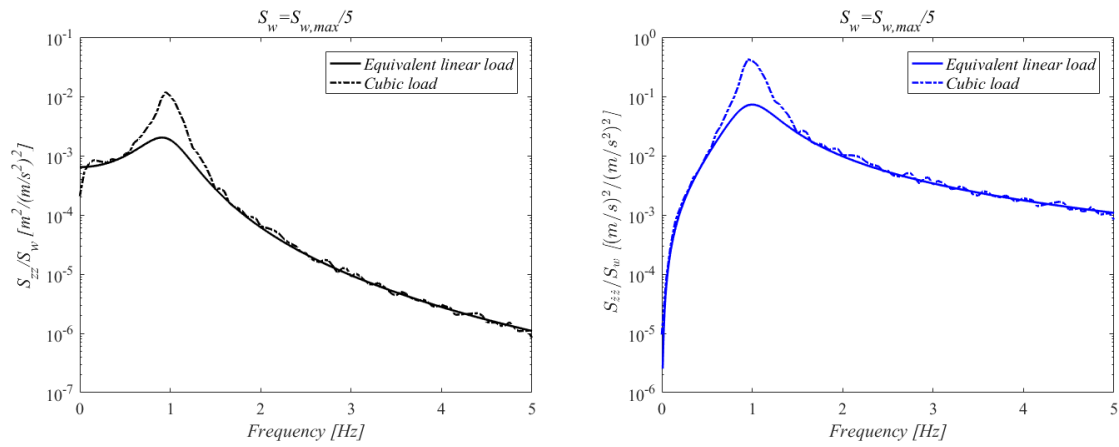


Figure 46: Power spectra of displacement (left) and velocity (right) for the cubic and the equivalent linear load where  $m=1\text{kg}$ ,  $c_m=0.2\text{Ns/m}$ ,  $k=4\pi^2$ ,  $K_t=1.1\text{N/A}$ ,  $R_{nl}=11\text{V}^3/\text{A}$ ,  $R_{l,eq}=0.34\Omega$ ,  $S_w=S_{w,max}/5$

The cubic load seems to produce the same effect on the response as in the harmonic case, as shown in Figure 46. In a linear system, the ratio between output and input is constant with respect to Figure 42. For the cubic load, when the input reduces, the ratio between output and input increases and is not constant. As shown in Chapter 3 for the harmonic case, a reduction of the input level causes the nonlinear device to be less damped and therefore the response around the resonance is larger than a linear system. The same effect can be detected in the cross spectrum, which is associated with the harvested power in Figure 47. Around resonance, the cubic system produces more power than a linear device. Nevertheless, unlike Figure 46, the cross spectrum off the resonance shows that the linear device has higher response and consequently produces more power (it is to remember that the average harvested power is the integral of the cross spectrum in frequency domain).

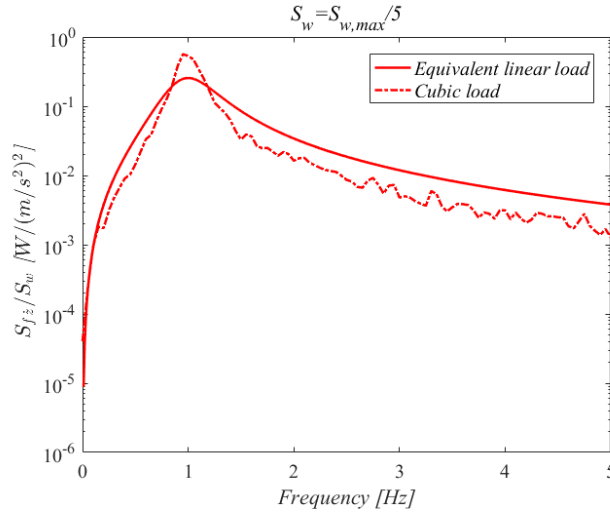


Figure 47: Cross spectrum of force and velocity for the cubic and the equivalent linear load where

$$m=1\text{kg}, c_m=0.2\text{Ns/m}, k=4\pi^2, K_t=1.1\text{N/A}, R_{nl}=11\text{V}^3/\text{A}, R_{l,eq}=0.34\Omega, S_w=S_{w,max}/5$$

Therefore, in a device with cubic load, a decrement of input level generates a higher power spectral density of the response, which means a larger variance, but it does not necessarily produce more power. The beneficial effect obtained at resonance with cubic load in Figure 47 is compensated off resonance where a linear device seems to perform better.

This behaviour can be observed also in the level curves of the variance velocity and the harvested power in Figure 48.

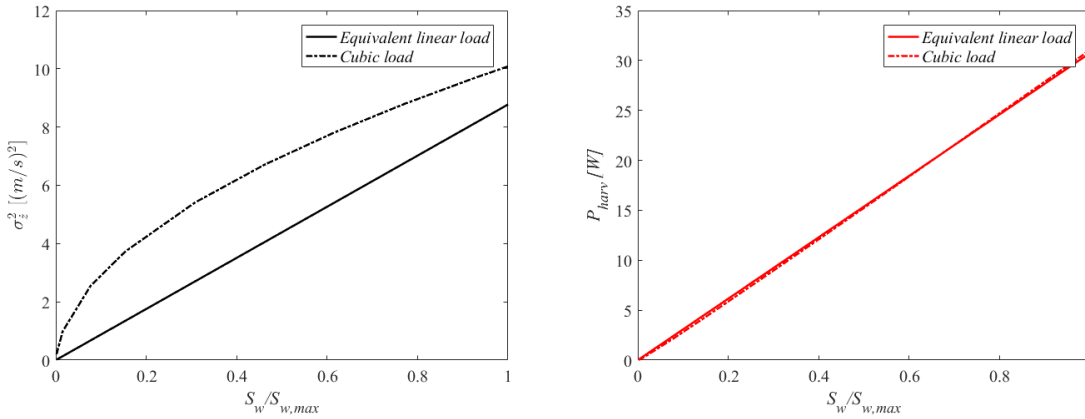


Figure 48: Level curves of the variance of velocity (left) and average harvested power (right) where

$$m=1\text{kg}, c_m=0.2\text{Ns/m}, k=4\pi^2, K_t=1.1\text{N/A}, R_{nl}=11\text{V}^3/\text{A}, R_{l,eq}=0.34\Omega$$

By reducing the input level  $S_w$  on the  $x$ -axis, the variance of the nonlinear device is larger; it is no longer a linear function of the input level as in the linear system. Nevertheless, this increment of variance is not beneficial for the harvested power. The harvested power is almost the same for both systems with linear and cubic load, the small differences are due to the fact that the cubic solution is computed numerically (thus, the input is not white). In addition, at the maximum input, the variance of velocity is not the same for the cubic and the linear load. As anticipated in Figure 42, the equivalent



linearization overestimates the damping and the variance is lower than that of the nonlinear system. The average harvested power is directly proportional to the input level for both linear and nonlinear devices, as demonstrated in [41]. It can be concluded that, for white noise, or more in general, for broadband excitation, a nonlinear load does not produce any benefit for the harvested power.

#### 4.9 Ambient excitation: Gaussian coloured noise

There are many different types of models, which may describe more practical excitations such as an earthquake or the motion of the sea wave, which excites the base of a ship. These signals are characterised by a bandlimited excitation that can be modelled as output of an analogue filter, which is fed with white noise input. Obviously, this representation is a rough approximation as both the earthquake and the sea wave are non-stationary. For excitation generated from the sea waves, which is the application considered in this thesis, the input can be described with good accuracy by using empirical spectra such as *Pierson-Moskowitz (PM)* and *JONSWAP*. These models were obtained by fitting measured data in specific seas and, consequently they cannot be always considered reliable. The *PM* spectrum was developed in 1964 from measurements in the North Atlantic. The best mathematical representation of this spectrum is a fifth order filter that changes its frequency content and amplitude according to the wind speed, as shown in Figure 49.

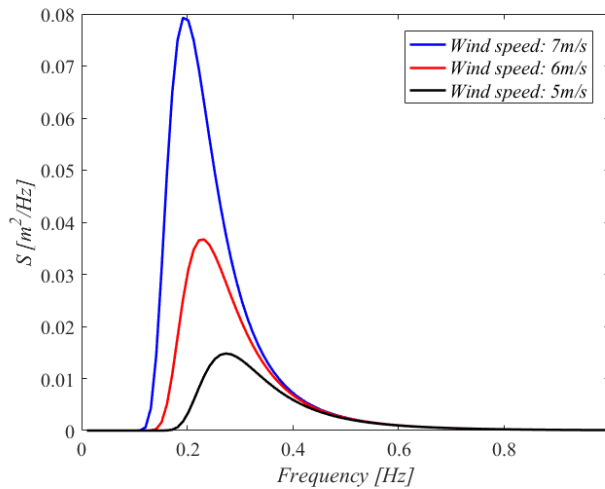


Figure 49: Pierson-Moskowitz spectrum. The amplitude of the spectrum increases as the wind speed rises

The wind speed influences the sharpness of the spectrum and provokes a slight shift of the resonance towards lower frequencies. For the sake of simplicity and generalisation (this section refers to more general bandlimited excitation and is not aimed to develop a theory for the sea waves excitation), the shape of the spectrum can be approximately assumed as a second-order filter, and the variation of the amplitude is related to a change of the damping of the filter.

In the following analysis, the base excitation of the energy harvester is generated by a second order filter, which is fed by a white noise. The transfer function of the filter is written as:

$$H_f(j\omega) = \frac{1}{-m_f\omega^2 + jc_f\omega + k_f} \quad (4.52)$$

The *PSD* of the output of the filter (or the input of the energy harvester) can be written as:

$$S_w = |H_f(j\omega)|^2 S_f \quad (4.53)$$

, where  $S_f$  is the white noise input of the filter. The parameters of the filter, in Table 4, are chosen such that the resonance matches with the natural frequency of the energy harvester:

Table 4: Parameters of the second order filter

<i>Parameter</i>	<i>Value</i>
$m_f [kg]$	1
$k_f [N/m]$	$4\pi^2$

The damping of the filter will be varied to make the input spectrum either sharper or broader. The equivalent load will then have to be updated according to the damping of the filter. No analytical methods will be used in this section to compute a closed-form solution for the equivalent load. The solutions for both nonlinear and linear load will be obtained from numerical integration and the equivalent linear load will be calculated by imposing the same variance of the output velocity.

As aforementioned, the damping ratio of the filter  $\zeta_f$  is varied. The mechanical damping  $c_m$  is constant and chosen such that the energy harvester behaves in an underdamped manner, ( $\zeta_m=0.016$ ). Nevertheless, the dynamics and, consequently, the harvested power can change depending on the damping of the filter, and therefore, we can have either a broadband filter (more damped) or a narrowband filter (less damped), which excites an underdamped energy harvester. For broadband filter, the damping ratio is set to  $\zeta_f=0.4$ , while for the narrow band filter we have  $\zeta_f=0.01$ . The output of the filter is shown for the two different damping ratios in Figure 50.

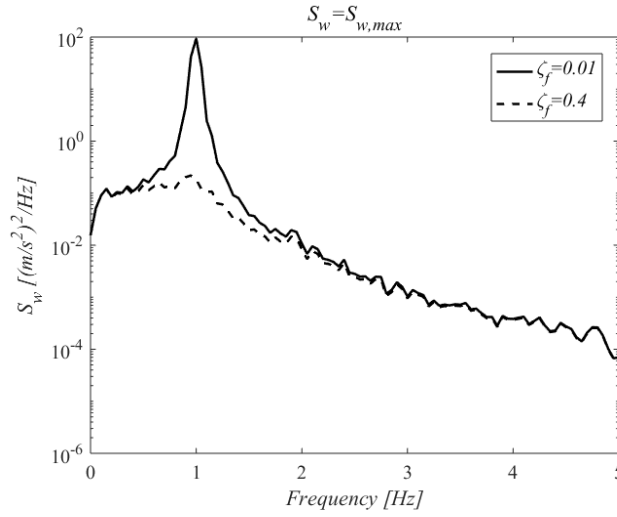


Figure 50: Output spectra of the filter for two damping ratios –  $\zeta_f=0.01$  (solid line),  $\zeta_f=0.4$  (dash line)

For  $\zeta_f=0.01$ , the nonlinear system is expected to behave similarly to the harmonic input, while  $\zeta_f=0.4$ , the bandwidth is much wider, similar to white noise or to a smooth first-order filter ( however, no analyses are carried out on first-order filters) and therefore the behaviour will be more similar to the white noise.

#### 4.10 Numerical linearisation

As stated previously, the results presented in this section are all obtained by numerical integration. Equation (4.20) still holds but the load is computed numerically. The equivalent load will be tuned so that the variance of the response is the same for the nonlinear and the equivalent linear system. It is assumed that the variance of velocity is equal to  $4.1(m/s)^2$  for  $\zeta_f=0.01$ , and  $0.132(m/s)^2$  for  $\zeta_f=0.4$ . The equivalent linear load will then be a function of both the input level  $S_w$  and the damping ratio of the filter  $\zeta_f$ . The parameters of the simulation are the same and listed in Table 3, where only the equivalent linear load changes. The numerical linearisation leads to the equivalent load reported in Table 5.

Table 5: Equivalent load as a function of the filter damping ratio

<i>Filter damping</i>	<i>Eq. linear load</i>
$\zeta_f=0.01$	$R_{l,eq}=1.18\Omega$
$\zeta_f=0.4$	$R_{l,eq}=26\Omega$

The harvesting forces, as shown in Figure 51 are referred to the cubic and the equivalent linear load, highlights that the nonlinearity is strong and therefore, it is expected that if the input level  $S_w$  reduces, the variance of the nonlinear harvester will not be linear.

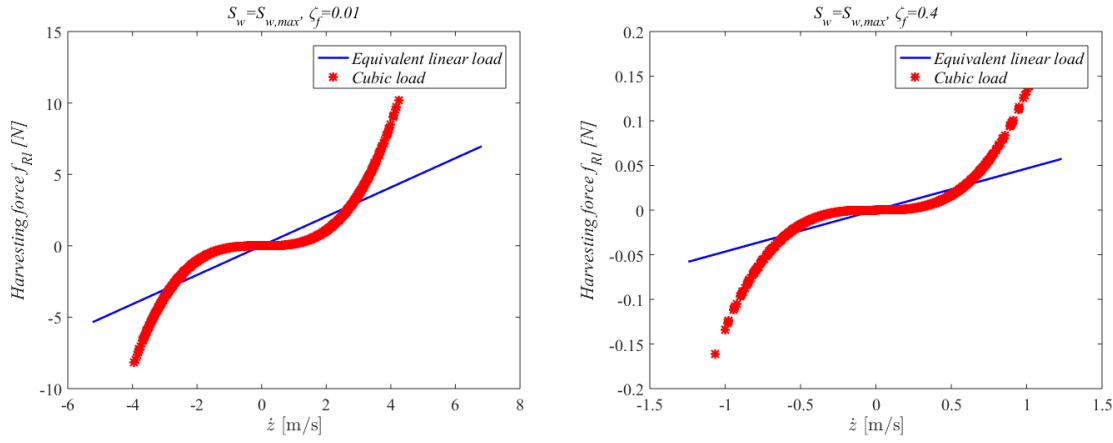


Figure 51: Harvesting force for the equivalent linear load (solid line) and cubic load (star markers) for  $S_w = S_{w,max}$ , and two values of damping of the filter  $\zeta_f = 0.01$  (left) and  $\zeta_f = 0.4$  (right)

By increasing the damping of the filter, the cubic force becomes smoother (Figure 51(right)) and, for example, within the range  $\pm 0.5$ , the effect of the nonlinearity is less strong.

For harmonic excitation, and white noise input, it was demonstrated that there exists an optimum load, which corresponds to the maximum achievable power. If the internal resistance is neglected, and the input excites a single frequency, it was found that  $R_{l,opt} = K_t^2 / c_m$  (for the given generator). A white input instead yields the paradoxical result; thus, the power is maximum when as the load tends to zero, as shown in Figure 45. It can be inferred that a bandlimited input results in a condition between these two. It is expected that as the damping of the filter reduces and the bandwidth becomes narrower, the optimum load gets closer to the optimum value computed for the harmonic input. Increasing the damping of the filter and broadening the frequency bandwidth reduces the optimum load, and the peak of harvested power gets closer to the y-axis. From the latter result, it can then be inferred that when the excitation is broadband, the use of a level dependent load is not an effective strategy to increase the power, because if the input is very broad, the peak of power will be very close to the y-axis and the optimum load will be nearly zero. Therefore, no adjustment of the load would be practically possible due to such a reduced margin of play. This is the reason why the level-dependent strategy is only pursued for narrow band input in the next sections.

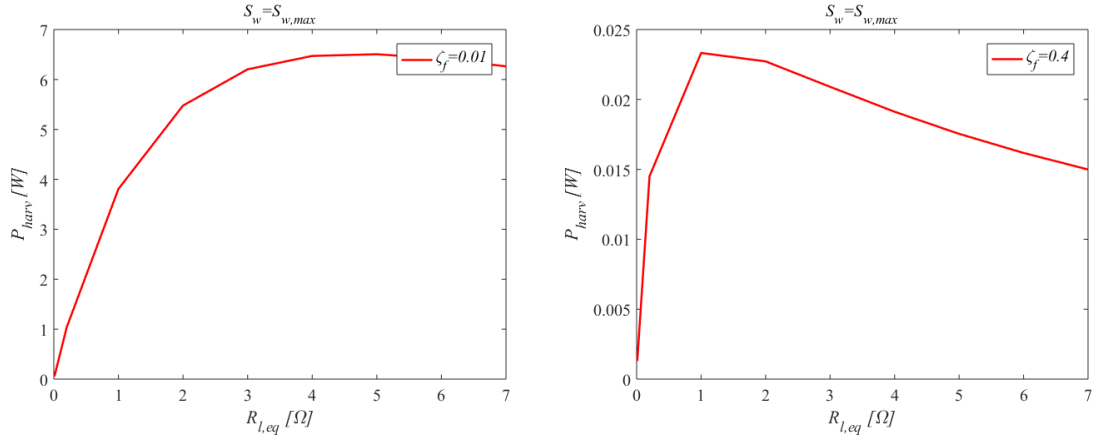
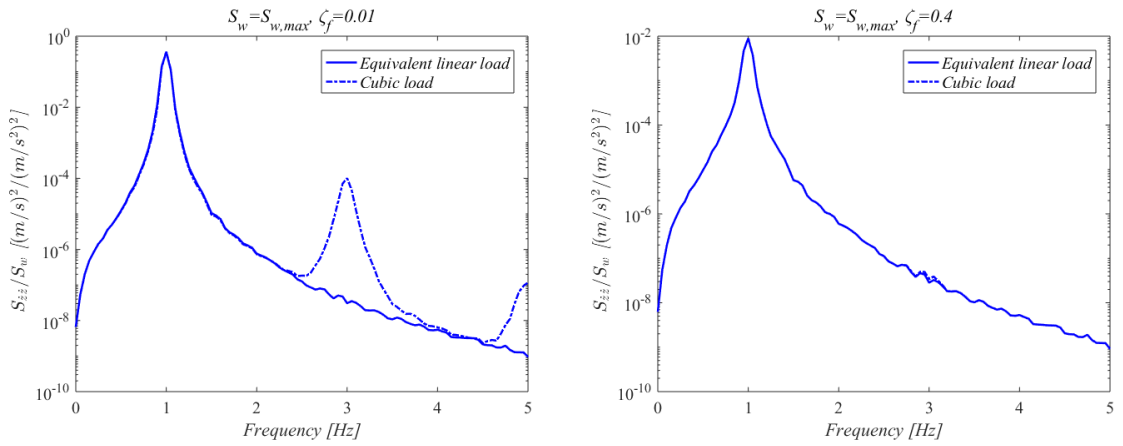


Figure 52: Average harvested power as a function of the electric load for  $\zeta_f=0.01$  (left) and  $\zeta_f=0.4$  (right)

If the damping ratio of the filter increases, the frequency bandwidth becomes wider and the energy spreads over a broader frequency range. This results in a system, which behaves in linear manner (Figure 53(top right bottom right)) like the case of white noise excitation. Instead, by reducing the damping ratio of the filter the response is more similar to what described in Chapter 3 for the harmonic excitation (Figure 53(top left, bottom left)).



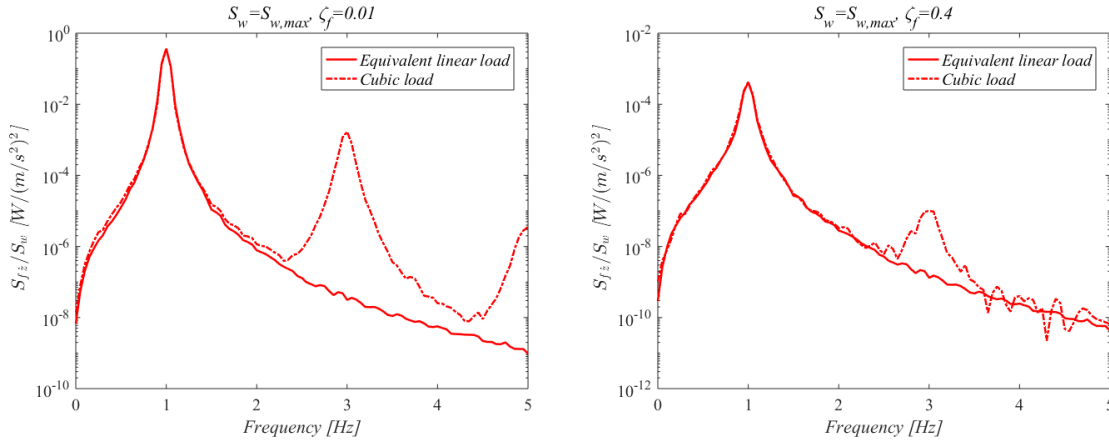


Figure 53: Power spectra of velocity (blue line, top) and cross spectrum of force and velocity (red line, bottom) for two values of the damping of the filter  $\zeta_f=0.01$ (left) and  $\zeta_f=0.4$ (right) - equivalent linear load (solid line) cubic load (dash dotted line) for  $S_w=S_{w,max}$

A narrow input concentrates the energy in a much smaller frequency range (around the natural frequency), and consequently, higher harmonic components appear due to the nonlinearity. It can be already said that, in terms of average harvested power, a cubic load is much more advantageous when the input is narrower because the contribution of the higher harmonics can be exploited. It can also be noticed that, unlike the previous section in which the equivalent linear solution (analytical) was lower than the numerical due to the assumption of the numerical method, here the cubic and the equivalent linear match perfectly also for a broad input because the linearisation was carried out numerically with no assumption on the probability distribution of the output. It might be reasonable to expect the same behaviour also in case of other types of nonlinear systems, such as Duffing's oscillators, in which the nature of a narrower excitation can generate higher harmonic components.

#### 4.11 Variation of the input level: level curve

The advantage of the cubic load is that at low input level, the response (either the relative displacement or the variance) is larger than a linear system because the damping force reduces. This aspect was shown for both harmonic and broadband excitation. Nevertheless, for white noise input, the increment of variance does not imply an improvement of the power. For a bandlimited input, the behaviour is in between and will be closer to the harmonic case as the damping of the filter reduces or closer to the white noise case if the damping of the filter increases. In Figure 54, the *PSD* of the output velocity and the cross spectrum between force and velocity is shown when the input is reduced up to a fifth of the maximum level  $S_{w,max}$ .

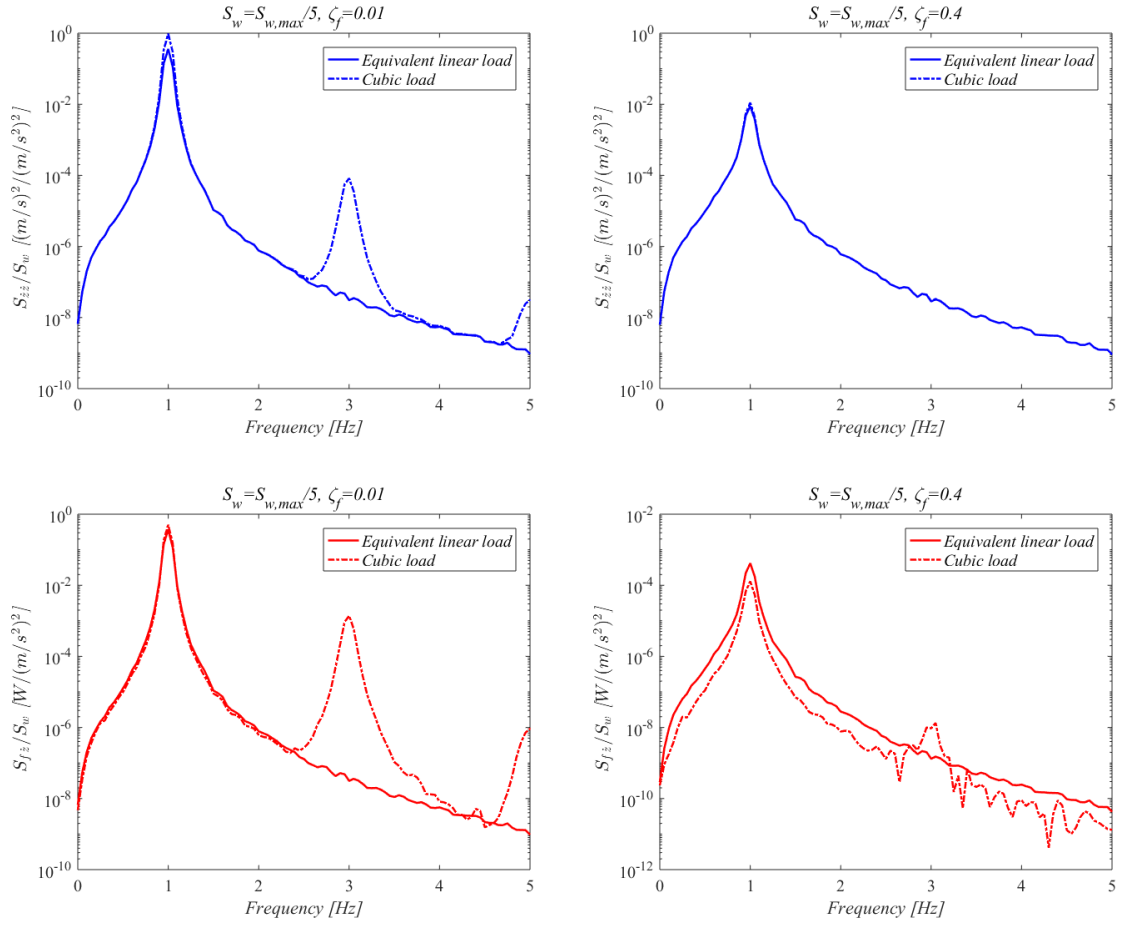


Figure 54: Power spectra of velocity (blue line, top) and cross spectrum of force and velocity (red line, bottom) for two values of the damping of the filter  $\zeta_f=0.01$ (left) and  $\zeta_f=0.4$ (right) - equivalent linear load (solid line) cubic load (dash dotted line) for  $S_w=S_{w,max}/5$

In case of  $\zeta_f=0.01$ , a cubic load generates a higher response  $S_{zz}$  at resonance and super harmonics such as the odd ones as typical of the cubic nonlinearity. Consequently, the variance will be larger than the linear system. The same result is achieved for  $S_{fz}$ , and, therefore harvested power is expected to be larger for such a value of damping of the filter. Such a narrow input has a similar and advantageous effect on both the response and the power as the harmonic input. Nevertheless, as the damping of the filter increases  $\zeta_f=0.4$  and the input becomes broader, the responses  $S_{zz}$  and  $S_{fz}$  show a similar behaviour to what was shown for white noise excitation. In particular, the higher harmonics are not excited (Figure 54(top right)), because the input energy is spread over a wider bandwidth and the system behaves globally in a linear manner. The effect of the nonlinearity is more evident in the  $S_{fz}$  where a third harmonic appears (Figure 54(bottom right)). However, the order of magnitude is very small and the difference between the cubic and the linear load can be considered as negligible.

The level curves of the variance of velocity and harvested power are plotted in Figure 55.

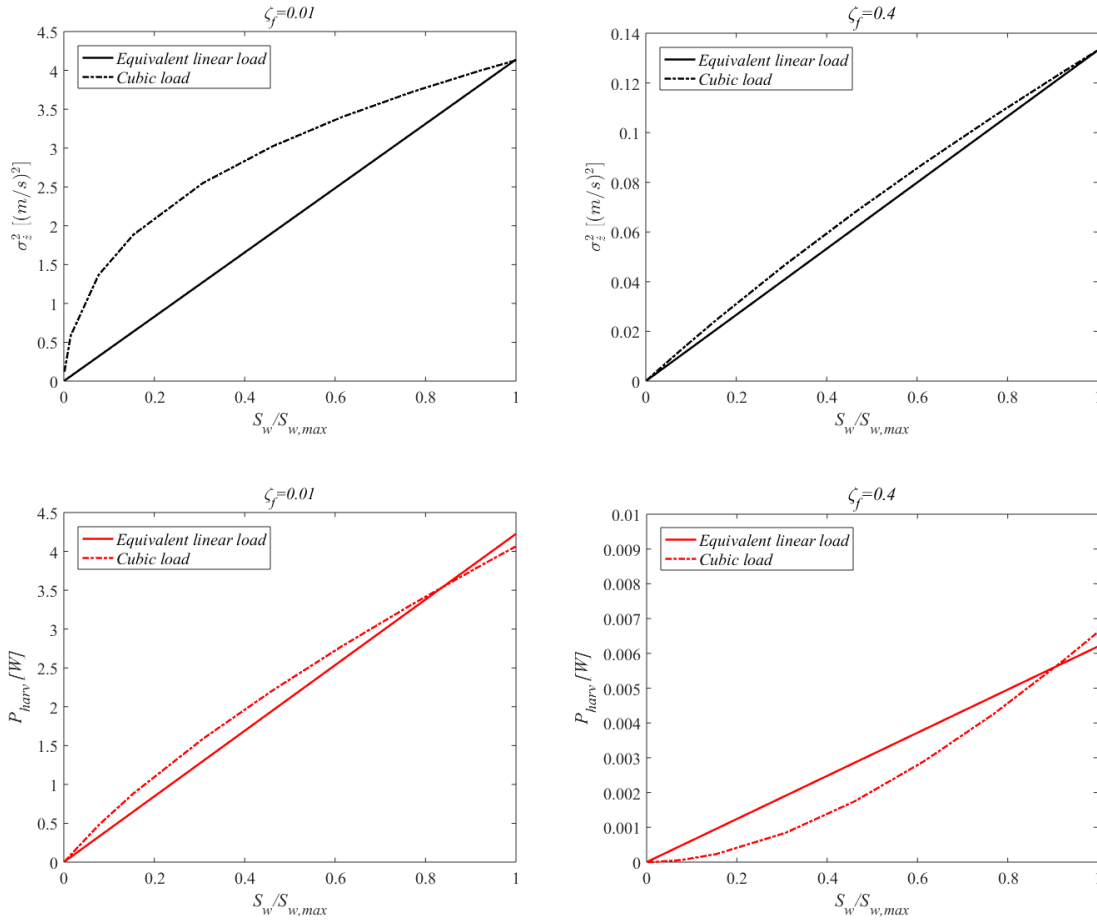


Figure 55: Level curves of the variance of velocity (black line, top) and average harvested power (red line, bottom) for two values of the damping of the filter  $\zeta_f=0.01$ (left) and  $\zeta_f=0.4$ (right) - equivalent linear load (solid line) cubic load (dash dotted line)

To confirm the results shown in Figure 54, the level curves state that by reducing the bandwidth of the input and concentrating the input energy around the resonance, a cubic load can be an advantageous solution to implement. However, if the input becomes wider (or the filter is more damped), then the nonlinear system does not show beneficial effect and is instead less effective than a linear system. Such a difference in Figure 55(bottom right) can be due to the fact that the excitation is not exactly a white noise but is more similar to a first-order filter.

#### 4.12 An alternative approach: the level-dependent load

In Chapter 3, a level-dependent load was considered as a strategy to increase the harvested power. By adjusting the load according to the input level, the device can always work at the optimum operating conditions, in particular when the harvester has a constraint on the throw. Throughout this chapter, we have noticed lots of similarities between the harmonic input and a narrow bandlimited input, and between the white noise and a broad bandlimited input. If the input is white or narrowband, it is meaningless to study the level-dependent load; either the power does not present any optimum load (white noise) or the optimum load has a very small range to play because is very close to zero.



Therefore, in this section, only the narrow bandlimited input is considered for the study of the level-dependent strategy. Thus, the damping ratio is  $\zeta_f=0.01$ . As shown in Figure 55, it was assumed that the variance is constrained and equal to  $4.1(m/s)^2$  at the maximum input level  $S_{w,max}$ . In Figure 56, the shunt load is plotted as a function of the input level

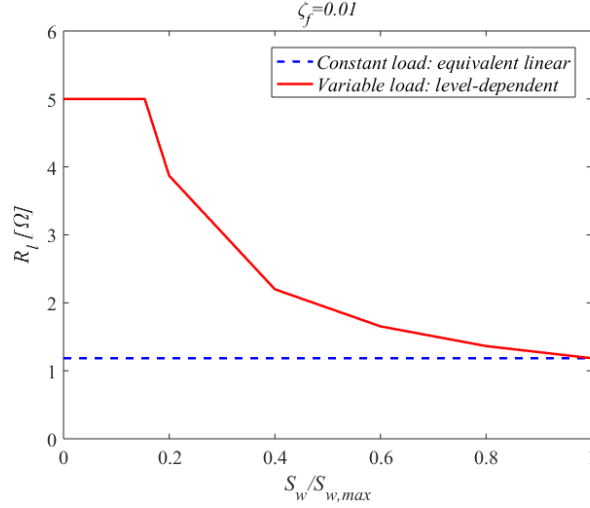


Figure 56: Shunt load as a function of the normalised input  $S_w/S_{w,max}$  - the red solid line is referred to the variable load, the blue dashed line is referred to the constant load

If the input reduces, the electric load is increased until the optimum load  $R_{l,opt}=5 \Omega$  shown in Figure 52, is achieved. The electric load is kept constant and the variance decreases linearly, as plotted in Figure 57(left).

As expected, this strategy produces a beneficial effect on the harvested power (Figure 57(right)) in the entire dynamics range compared to both linear and cubic load, as also shown in Chapter 3.

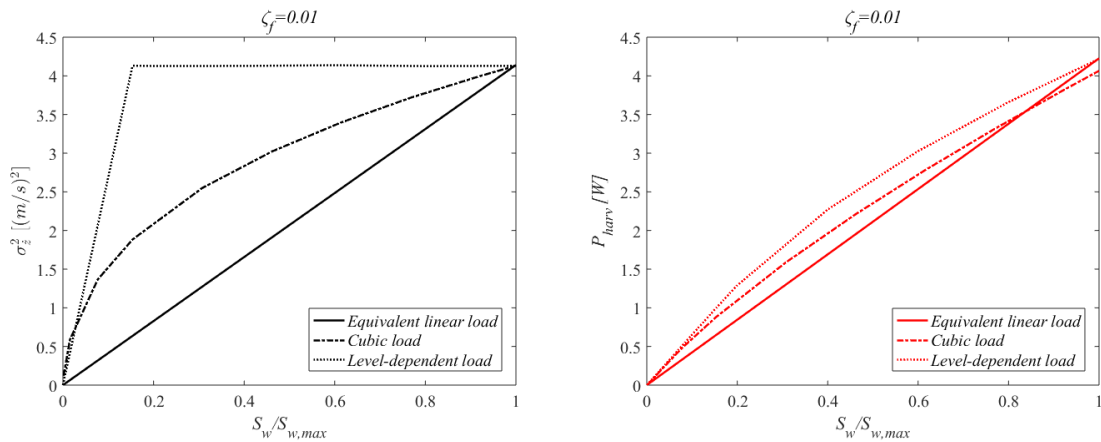


Figure 57: Level curves of the variance of velocity (left) and average harvested power (right) as a function of the normalised input  $S_w/S_{w,max}$  – equivalent linear load (solid line), cubic load (dash dotted line) and level-dependent load (dotted line)

It was demonstrated that the level-dependent load strategy is not only applicable to harmonic input but also to more practical situations. Here, a second-order filter was used but also other types of input

such as low pass or high pass filters can be considered; the important thing is that the resonance of the harvester falls within the frequency bandwidth of excitation.

### 4.13 Summary

The aim of this chapter was to analyse the response of an electromagnetic energy harvesting device subjected to Gaussian random excitation. The energy harvester was assumed to have a constraint on the probability of the output displacement, which is limited by the size of the device and the available volume. The numerical integration was compared to the analytical solution obtained by using the equivalent linearization method, whose main approximation relies on the assumption that the output of a nonlinear system is Gaussian. This assumption produces large errors when the system is highly nonlinear, and results in an underestimation of the variance (or in other words an overestimation of the damping). For white input noise, it was shown that the deliberate introduction of a nonlinear load enlarges the dynamic range of the variance but does not affect the average harvested power, which depends linearly on the input spectrum.

The chapter focused also on more practical bandlimited excitation. Assuming to model the sea waves signal as the output of a second-order filter excited by a white noise, the same analyses were carried out. The bandwidth of the filter was varied to simulate both narrow and broader input excitation. It was shown that when the damping of the filter is smaller than the mechanical damping of the structure, the results are similar to the harmonic excitation, and the introduction of a cubic load is beneficial for the average harvested power in the entire dynamic range of performance. On the opposite, when the input signal is broader, no benefits can be detected for the power, and the results are coherent with the analyses made for white noise input. Also, for narrow input, the level-dependent strategy was studied. It was proven that, like the harmonic case, a level dependent load can improve the average harvested power in electromagnetic devices with respect to both linear and cubic load.

## **Chapter 5: Design of an electromagnetic transducer energy harvester**

### **5.1 Introduction**

In this chapter, the design of a demonstrator of an electromagnetic energy harvesting device is presented [73]. The device will be used to validate some of the numerical results obtained in Chapter 3. In particular, it is aimed to demonstrate that a level-dependent load can increase the dynamic range of performance and improve the harvested power compared to a device with constant load. Since now on, the term ‘constant’ load will be used to identify the linear system in which the load is not varying with the input  $Y$ , instead the level-dependent load will be termed as ‘variable’. The device can be considered as a demonstrator, which is a proof of concept, rather than being a prototype for real applications, and therefore, the goal is not to design a device with the highest performance among commercial devices, but to demonstrate that the use of such a nonlinearity can increase the harvested power.

The device will be tested onto a shaker; therefore, the design of the demonstrator will depend on the performance of the actuator.

The first part of the chapter provides an example of energy harvesting device for marine application. The second part focuses on the dynamics of the harvester; by choosing the architecture of the device, for instance how the system vibrates (thus rotation or translation), the dynamic equation of motion of the device is derived using the Lagrangian method. The equation of motion will then be used in the second part of the chapter, which concentrates on the definition of the constraints in terms of maximum angular displacement and natural frequency. Using the analytical solution of the equation, mass, stiffness and geometrical properties are calculated by mean of a parametrical analysis. Having this information, a CAD model is built up and a set of drawings is drawn, which are used for the manufacturing stage.

### **5.2 Ball screw based energy harvesting device**

In this section, an example of energy harvester for marine application is described. The design was developed by Dr. M. Hendijanizadeh during his PhD, and it is published in [23,24]. However, the author and Dr. M. Hendijanizadeh collaborated in the estimation of the damping of the structure and the results are presented in this section.

The device is a ball screw based energy harvester, which is aimed to harvest energy from the vertical motion of a boat. The characteristics of the environmental vibration conditions, such as frequency

and input amplitude of the excitation, depend on the weather, boat speed, boat size and sea depth. In particular, it was seen that the frequency bandwidth of excitation is nearly narrow and the dominant component is around  $1\text{ Hz}$ . Therefore, for a first approximate analysis, the excitation is approximated by a harmonic function. To determine the excitation frequency and the amplitude of the input displacement, measurements were carried out in the English Channel. The fundamental harmonic component was found to be about  $f_{res}=0.8\text{Hz}$  and the maximum input amplitude  $Y_{max}=1\text{m}$ .

The base-excited harvester consists of a mass – spring system, in which the motion of the suspended mass is caused by the vertical oscillation of a boat; therefore, the vertical motion of the mass has to be transformed into a rotational motion, to drive the generator. The ball screw provides this transformation, and a low frequency vertical motion can be turned into a high frequency rotational motion. The design characteristics of the ball screw, in particular the lead, affect the efficiency of transforming a vertical motion into a rotational one. Since the power generated by the generator is a function of the rotational velocity, the ball screw has to be designed in such a way that the output power is maximised. A high frequency rotational motion can produce more power but, on the other side, the friction between the lead and the mass is larger. Therefore, the lead of the ball screw is parameter that has to be optimised to obtain the best compromise between high performance and low dissipative effects.

The new contribution of the author in this chapter is to introduce the effect of the static friction in the model proposed by Dr. M. Hendijanizadeh, and to analyse its effect on the response of the system.

Part of this collaboration is published in [55].

The energy harvester proposed by Dr. M. Hendijanizadeh is shown in Figure 58. It comprises a seismic mass, which moves upwards and downwards, two springs, and a ball screw, which couples the mechanical circuit to the electrical circuit and is utilised to convert linear motion of the mass to a rotational motion to drive a rotary generator placed on the top of the harvester.

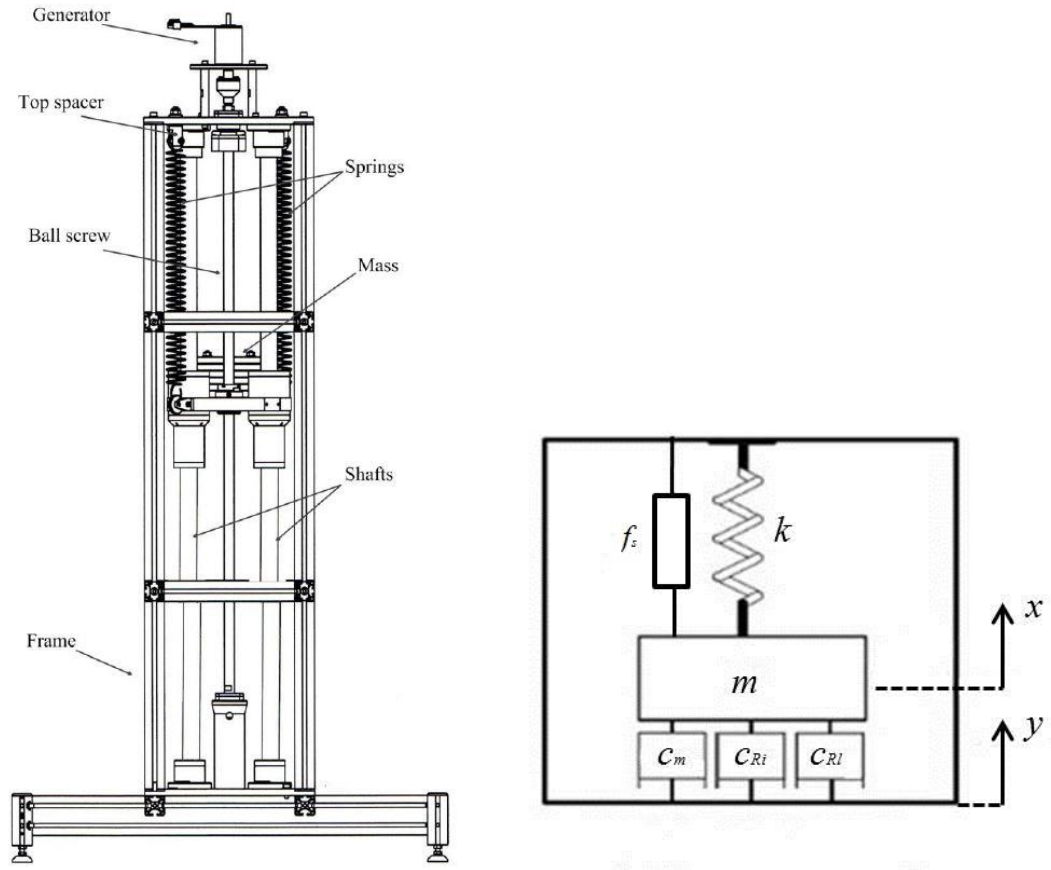


Figure 58: Energy harvester for boat's vertical motion (left) and free body diagram (right)

In addition to the original, parasitic static friction  $f_s$  is introduced in the free body diagram to simulate the dissipation provided by the ball screw.

The equation of motion can be written as follows,

$$M\ddot{z}(t) + \left(\frac{2\pi}{l}\right)^2 (c_m + c_{Rl} + c_{Ri})\dot{z}(t) + f_s \operatorname{sgn}(\dot{z}(t)) + kz(t) = -m\ddot{z}(t) \quad (5.1)$$

Where  $M = m + (2\pi/l)^2 (J_{b-s} + J_g + J_c)$  is the total mass, which comprises the suspended mass  $m$  and the inertia of the ball screw  $J_{b-s}$ , the generator  $J_g$  and the coupling shaft between the ball screw and the generator  $J_c$ .

The term  $(2\pi/l)^2$  transforms the equation from equilibrium of momenta to equilibrium of forces and it represents the analogue of a gear ratio when a gear box is used (for example in the next sections).

The term  $c_m$  corresponds to the mechanical viscous coefficient, and  $c_{Rl}$  and  $c_{Ri}$  are the electrical damping of the load resistance  $R_l$  and of the internal resistance  $R_i$  respectively, of a three-phase electrical circuit.

The only source of nonlinearity is the parasitic static friction  $f_s$ , and its effect is studied in this chapter. The elastic force is given by the product between the stiffness  $k$  and the relative displacement  $z=x-y$ .

The simulation parameters are given in Table 6

Table 6: Input parameters of the ball screw harvester

<i>Parameter</i>	<i>Value</i>
<i>Suspended mass <math>m</math> [kg]</i>	8
<i>Lead <math>l</math> [m]</i>	0.02
<i>Stiffness <math>k</math> [N/m]</i>	250
<i>Total moment of inertia <math>J</math> [kgm<sup>2</sup>]</i>	$4.9e-5$
<i>Max input displacement <math>Y_{max}</math> [m]</i>	1
<i>Max rel displacement <math>Z_{max}</math> [m]</i>	0.3
<i>Transduction coefficient <math>K_t</math> [Nm/A]</i>	0.0232
<i>Internal resistance of the coil <math>R_i</math> [<math>\Omega</math>]</i>	0.1

To evaluate the static friction of the energy harvester, a test was run by Dr. Hendijanizadeh and the author, which consists in marking two static equilibrium positions ( $x_1$ ,  $x_2$ ). Firstly, the suspended mass  $m$  was pushed down until the springs were stretched up to their maximum allowable limit and then released. The static equilibrium of the system at this stage can be written as follows

$$f_s + mg = kx_1 \quad (5.2)$$

, where  $x_1$  is the extension of the springs in this condition. Afterwards, the same procedure was followed but the mass was pushed up and then released. The static equilibrium condition is

$$f_s + kx_2 = mg \quad (5.3)$$

, where  $x_2$  is the extension of the springs in second condition.

By subtracting equation (5.2) and equation (5.3), it follows

$$2f_s = k(x_2 - x_1) \quad (5.4)$$

The distance between the two equilibrium positions  $x_2 - x_1$  was measured to be  $0.063m$  and, considering  $k=250$  N/m, the measured static friction is  $f_s=8.37N$ .

Before analysing the response of the system, it is necessary to determine the optimum condition in which the harvested power can be maximised. As shown in Chapter 3, for an harmonic excitation the optimum load is given as,

$$R_{l,opt} = R_i + \frac{K_t^2}{c_m} \quad (5.5)$$

The energy harvester is mounted onto a shaker and the generator terminals are connected to resistors, as shown in Figure 60 (left). The output signal was acquired by the accelerometers, one mounted upside down beneath the mass (1) and one placed on the base (2), as shown in Figure 60 (right). Once the signals are acquired, the relative acceleration can be computed by using equation (5.6).

$$\ddot{x} = \ddot{x}_1 - \ddot{x}_2 \quad (5.6)$$

The voltage across the terminals was measured with a voltmeter, and used to compute the harvested power, as

$$P_{ave} = \frac{E[v^2]}{R_l} \quad (5.7)$$

The experimental and the numerical results are shown in Figure 59.

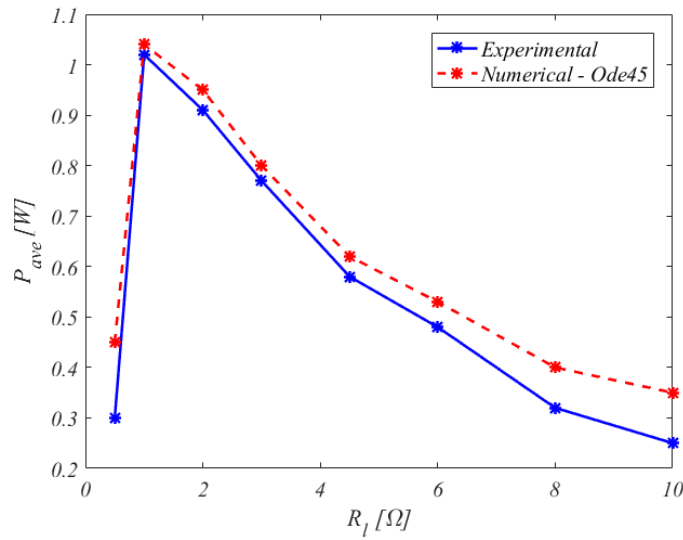


Figure 59: Average harvested power as a function of the load resistance - Experimental (dash red line) and numerical (blue solid line) results

The optimum load resistance, for which the power is maximised, is found be equal to  $1\Omega$ .

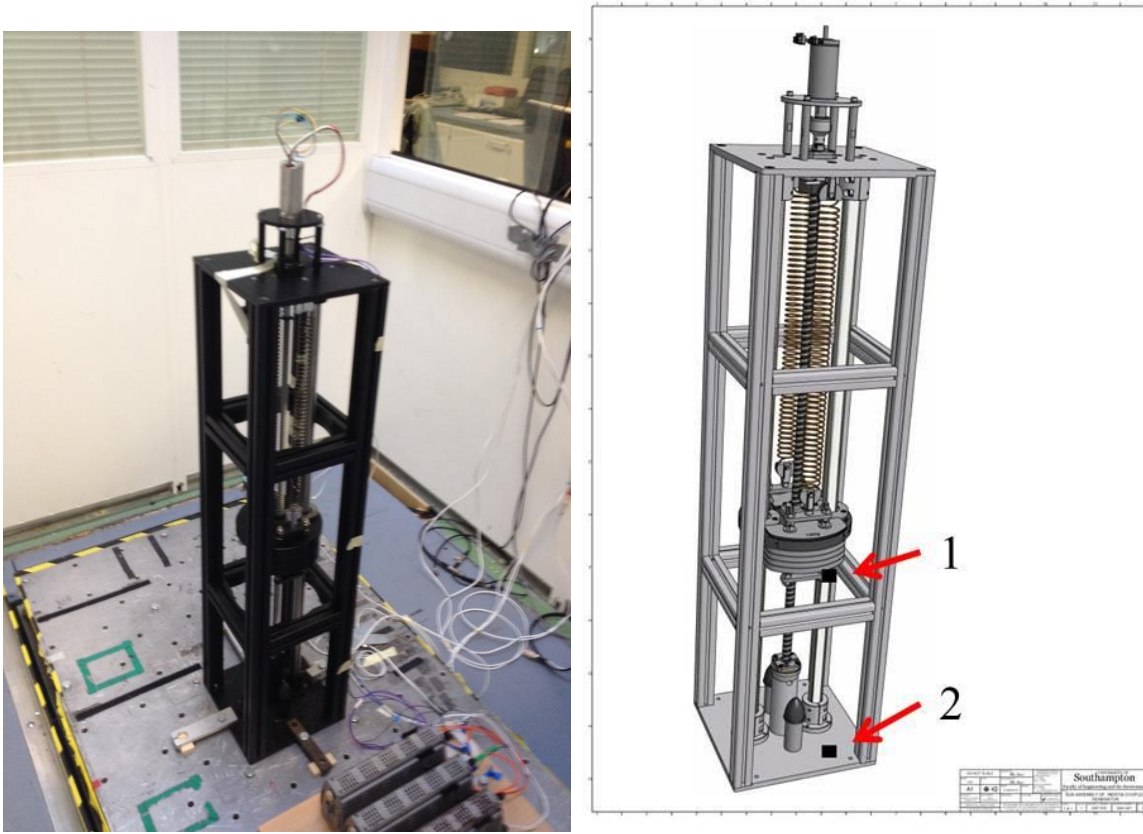


Figure 60: Experimental set up

To characterise the energy harvester, it is necessary to understand how it behaves when excited at resonance because, as shown in Chapter 3, the power harvester depends on the system response.

In order to obtain the frequency response functions, the experiments were conducted in two different operating conditions: open circuit (the electrical and the mechanical circuits are decoupled) and load circuit (the electrical and the mechanical circuits are coupled). A more detailed description will be given in Chapter 6.

A stepped test was conducted by maintaining the input acceleration as a constant at  $3m/s^2$ . This means that the relative transmissibility  $Z/Y$  is computed by varying both the frequency and the input amplitude of the displacement  $Y$  at same time.

For the open circuit condition, which consists in decoupling the electrical and the mechanical circuit ( $c_{Rl}=c_{Ri}=0$ ), the only contribution to the viscous damping is produced by the mechanical system  $c_m$ . By fitting the numerical frequency response function with the experimental one, an estimation of the viscous damping parameter  $c_m$  can be computed (Figure 61 (left)). Successful, the circuit is coupled and the fitting is carried on in load condition with  $R_l=0.5\Omega$ , as shown in Figure 61 (right).



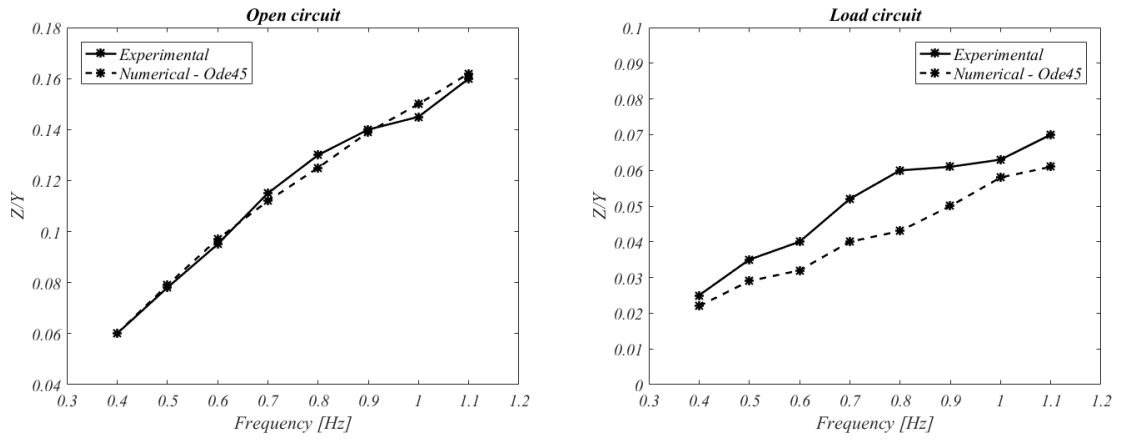


Figure 61 Relative transmissibility in frequency domain: open circuit (left) and load circuit (right)

As aforementioned, by fitting the numerical FRF with the experimental one, in open circuit, an estimation of  $c_m$  is obtained,  $c_m=0.0016Nms$ . It is to notice that there is a good agreement between the numerical and the experimental results, in particular in open circuit condition. When the load is attached, the results start diverging, perhaps due to the uncertainty on the load's resistors. In load conditions, the numerical solution seems to underestimate the solution. The average harvested power can be computed in frequency domain using equation (5.8), and plotted in Figure 62.

$$P_{ave} = \frac{1}{2} c_{Rl} \omega_n^2 Z^2 = \frac{1}{2} \frac{K_t^2 R_l}{(R_i + R_l)^2} \omega_n^2 Z^2 \quad (5.8)$$

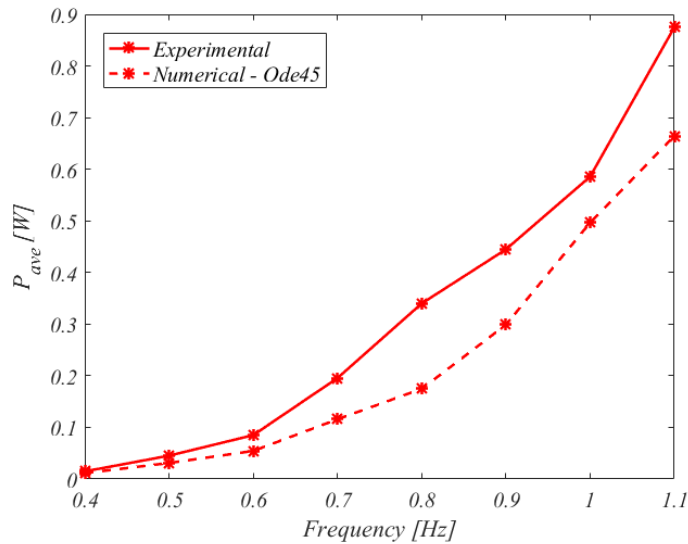


Figure 62: Average harvested power in frequency domain for  $R_l=0.5\Omega$

The design energy harvester manifests an overdamped behaviour, which results in a low performance in terms of harvested power (Figure 67). The presence of friction due to the ball screw reduces the

average power. Consequently, either a different mechanism of conversion of motion is implemented, such as a lead screw or a different design has to be provided. In the following, the author provides a new design of energy harvester, which will be used to demonstrate the higher performance of energy harvester with electrical nonlinearity.

### 5.3 System dynamics

The proposed energy harvesting device is shown in Figure 63. It consists of a mechanical system connected to a generator via a gearbox, whose specifications are reported in Appendix IV. The gearbox and generator are already available, and will not be part of the design process.

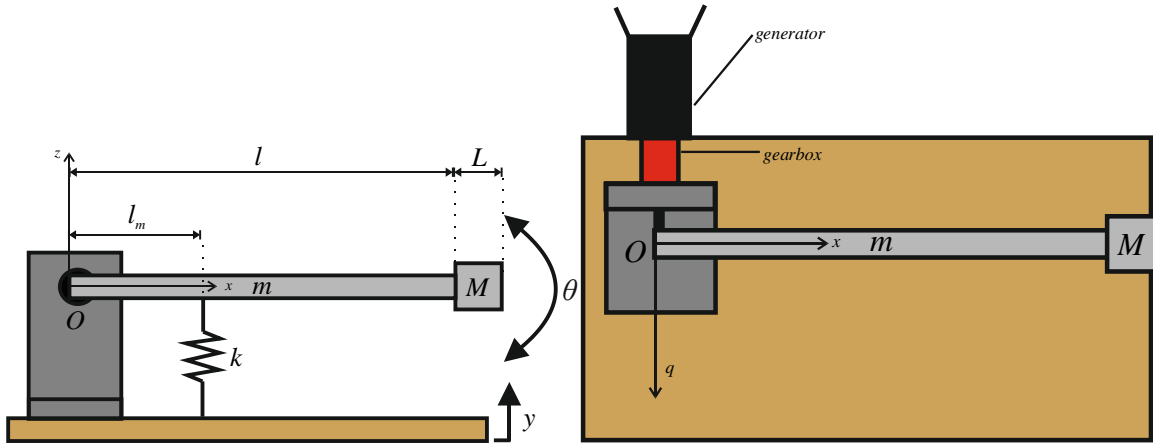


Figure 63: A schematic representation of the proposed energy harvesting device consisting of an oscillating beam connected to a DC generator through a gearbox – Frontal view (left), top view (right)

The mechanical system consists of an oscillating beam of mass  $m$  and length  $l$ , which, as aforementioned, is coupled with a gearbox and generator. A spring of stiffness  $k$  connects the beam to the ground and, on the right side, a lumped cuboid mass  $M$  and length  $L$  is screwed to the beam. The inertial reference system has the origin in  $O$  and it is constituted by the direction  $x$  along the beam,  $z$  perpendicular to the base and  $q$  directed along the axis of the generator. The distance between the spring and the rotation point of the beam  $O$  is called  $l_m$ . The gearbox is screwed to a flange, which, in turn is clamped to the base. Moreover, it is assumed that the inertia of the generator and the gearbox is negligible and the beam behaves as a rigid body. The centre of mass of system in relative coordinates can be computed with respect to the point  $O$  as:

$$|\bar{x}_{CM,O}| = \frac{m \frac{l}{2} + M \left( l + \frac{L}{2} \right)}{m + M} \quad (5.9)$$

If the proposed device is clamped onto a shaker, and an input displacement  $y$  is imposed, then the position of the centre of mass becomes, in absolute coordinates as:

$$\vec{r}_{CM} = |\vec{x}_{CM,O}|(\sin \theta \vec{i} + \cos \theta \vec{w}) + y \vec{i} \quad (5.10)$$

, where  $\vec{i}$  and  $\vec{w}$  are the versors along the vertical direction  $z$  and the axial direction  $x$ . However, only the dynamics in the  $z$  direction are considered, therefore, the components along the versor  $\vec{w}$  will be neglected hereafter. The velocity of the centre of gravity is obtained by taking the derivative of equation (5.10) with respect to time as follows:

$$\dot{\vec{r}}_{CM} = \left( |\vec{x}_{CM,O}| \dot{\theta} \cos \theta + y \dot{\theta} \right) \vec{i} \quad (5.11)$$

The acceleration at the centre of gravity is:

$$\ddot{\vec{r}}_{CM} = \left[ |\vec{x}_{CM,O}| (\ddot{\theta} \cos \theta - \dot{\theta}^2 \sin \theta) + \ddot{y} \right] \vec{i} \quad (5.12)$$

The kinetic energy  $T$  can be obtained considering the motion of the beam, but also the flange and the base, which are attached to the top end of the shaker,

$$T = \frac{1}{2} J_{CM} \dot{\theta}^2 + \frac{1}{2} (m + M) \dot{\vec{r}}_{CM}^2 + \frac{1}{2} (m_{DC} + m_{extra}) \dot{y}^2 \quad (5.13)$$

, where  $J_{CM}$  is the moment of inertia with respect to the centre of gravity, which can be calculated from equation (5.14),  $m_{DC}$  is the mass of the generator plus the gearbox and  $m_{extra}$  is the of the flange and the base.

$$J_{CM} = J_{beam,g} + m d_{g-CM}^2 + J_{mass,G} + M d_{G-CM}^2 \quad (5.14)$$

The terms  $J_{beam,g}$  and  $J_{mass,G}$  are the moments of inertia of the beam and the lumped mass with respect to their centres of gravity, and  $m d_{g-CM}^2$  and  $M d_{G-CM}^2$  are additional terms due to the fact that the point  $O$  does not coincide with the centres of gravity of the single components. Assuming that the beam is a rectangular parallelepiped and the lumped mass is cubic, the moment of inertia  $J_{CM}$  is then:

$$J_{CM} = \frac{m}{12} (l^2 + b^2) + m \left( x_{CM,O} - \frac{l}{2} \right)^2 + \frac{ML^2}{6} + M \left( \left( l + \frac{L}{2} \right) - x_{CM,O} \right)^2 \quad (5.15)$$

The potential energy is caused by the elastic deflection of the spring, and the gravity, and is computed as follows:

$$V = \frac{1}{2} k (l_m \sin \theta)^2 + (m + M) \vec{r}_{CM} \cdot g \vec{i} + (m_{DC} + m_{extra}) y g \vec{i} \quad (5.16)$$

, where  $g$  is the gravity acceleration and is  $9.81 m/s^2$ . In classical mechanics, any physical system is characterised by the Lagrangian function  $L_f$ , which summarises the dynamics of the entire system. The Lagrangian function  $L_f$  is defined as:

$$L_f = T - V \quad (5.17)$$

If, the system is also subjected to non-conservative forces, such as the damping force, then the so-called Rayleigh function  $R$  has to be considered.

$$R = \frac{1}{2} c_m \dot{\theta}^2 \quad (5.18)$$

, where  $c_m$  is the mechanical viscous damping. By applying the Lagrangian equation, the generalised coordinate  $\theta$

$$\frac{\partial}{\partial t} \left( \frac{\partial L_f}{\partial \dot{\theta}} \right) - \frac{\partial L_f}{\partial \theta} + \frac{\partial R}{\partial \dot{\theta}} = 0 \quad (5.19)$$

, and substituting equation (5.17) and (5.18) into equation (5.19), and assuming small oscillation (thus,  $\sin\theta \approx \tan\theta \approx \theta$  and  $\cos\theta \approx 1$ ) then the linearised equation of motion for the mechanical system becomes:

$$(J_{CM} + (m + M)x_{CM,O}^2) \ddot{\theta} + c_m \dot{\theta} + k l_m^2 \theta = - \left( m \frac{l}{2} + M \left( l + \frac{L}{2} \right) \right) (\ddot{y} + g) \quad (5.20)$$

For simplicity, the total moment of inertia is indicated with  $J$ . For the input  $y$ , the Lagrangian equation can be written as:

$$\frac{\partial}{\partial t} \left( \frac{\partial L_f}{\partial \dot{y}} \right) - \frac{\partial L_f}{\partial y} = 0 \quad (5.21)$$

Solving equation (5.21), it yields:

$$x_{CM,O} \ddot{\theta} = -M_{tot} (\ddot{y} + g) \quad (5.22)$$

, where  $M_{tot}$  is the total mass attached onto the shaker, and is defined as follows:

$$M_{tot} = m + M + m_{DC} + m_{extra} \quad (5.23)$$

From equation (5.22), the relation between the input of the shaker and the angular response can be studied, but it does not describe the equation of motion of the system, which, instead is derived from equation (5.20).

When a generator is coupled with the mechanical system and the gravity is neglected, as it does not contribute to the output power, then the equation (5.20) becomes:

$$(J_{CM} + (m + M)x_{CM,O}^2)\ddot{\theta} + c_m\dot{\theta} + kl_m^2\theta + K_t i = -\left(m\frac{l}{2} + M\left(l + \frac{L}{2}\right)\right)\ddot{x} \quad (5.24)$$

$$K_t i = (R_i + R_l)\dot{i} \quad (5.25)$$

, where  $R_i$  is the internal resistance due to the coil,  $R_l$  is the load,  $i$  is the current and  $K_t$  is the transduction coefficient. The effect of the inductance  $L$  of the generator is neglected on purpose, as at low frequency it does not contribute to the voltage. Expliciting the current  $i$ , in equation (5.25), and substituting into equation (5.24), we have:

$$J\ddot{\theta} + c_m\dot{\theta} + kl_m^2\theta + \frac{K_t^2}{R_i + R_l}\theta = -\left(m\frac{l}{2} + M\left(l + \frac{L}{2}\right)\right)\ddot{x} \quad (5.26)$$

, where  $J$  is the total moment of inertia with respect to the point  $O$ . Equation (5.26) describes the dynamics of the energy harvester for different load conditions assuming that the system is linear. However, it is well-known [74], that the gearbox can have a nonlinear response, in the form of parasitic friction. As shown in Chapter 3, the friction depends on the relative velocity and consequently on the input excitation. However, due to the difficulty of estimating a reliable friction coefficient, which will take place during the experiments, for simplicity, this aspect will be neglected throughout the design process and an equivalent viscous damping will be assumed.

## 5.4 Design process

In this section, the strategy to find the main parameters of the harvester is proposed. When designing an energy harvesting device, the first step is usually to study the characteristics of the vibration source. The type of excitation, which is characterised by the frequency content and the input level, influences the choice of the inertial and stiffness properties of the system as well as the response. As aforementioned, the proposed energy harvester is not aimed to operate in a real environment; it is therefore worth of briefly describing the performance of the shaker, since it has a direct consequence on the design process.

### 5.4.1 Characteristics of the excitation

In Chapter 3, it was shown that a harmonically excited energy harvesting device with a variable shunt load can increase the performance compared to a constant load. Therefore, the harvester is supposed to be harmonically excited and to obtain the best performance in terms of power it is necessary that the excitation frequency matches the natural frequency of the harvester. An electrodynamic shaker (Derritron type VP85) and a power amplifier (Gearing & Watson SS300) are used to generate base excitation.

The excitation frequency and the input level are not known. Nevertheless, some considerations are made to determine these parameters. The shaker has a wide region in which the transfer function between the acceleration provided and the input voltage is constant, and this is usually the desired region to operate. However, the performance of the shaker drops at low frequency, in which the stroke displacement is limited, and at high frequency, in which the force generated is limited. In addition the transduction mechanism of the energy harvester is, in this case, electromagnetic. Electromagnetic devices are commonly used in low-frequency applications where the displacement involved are large [5]; at high frequency, these systems are abandoned in favour of piezoelectric devices, characterised by a higher operative frequency bandwidth and small displacement, [6]. Moreover, the gearbox is generally not suitable for applications in which the excitation frequency is high, because of ‘rattling’ phenomena [75], which may damage the teeth. These considerations suggest us to choose a natural frequency of  $7.5\text{Hz}$ , which represents a good compromise between the performance of the shaker and the operating range of gearbox and generator.

To determine the maximum input level, a sinusoidal test was conducted at  $7.5\text{Hz}$ . A proof mass was clamped onto the shaker and the input, provided by the amplifier, was gradually increased until the saturation of the amplifier was achieved. The double integration of the signal acquired by the accelerometer on top of the shaker resulted in a displacement of  $12\text{mm}$  peak-to-peak. It is clear that this value is only a reference because a proof mass is a rigid with as no dynamics in the frequency range of interest. The maximum input level is expected to be lower than  $12\text{mm}$  because force transmitted from the harvester to the shaker will be larger than the proof mass due to the dynamics of the device. The maximum displacement provided is assumed to be  $8\text{mm}$  peak-to-peak. To ensure the shaker can provide enough input displacement, the total mass  $M_{tot}$  of the device, which comprises of the dynamic masses  $m$  and  $M$ , and the rigid masses  $m_{DC}$  and  $m_{extra}$ , is limited to  $3\text{kg}$ .

#### 5.4.2 Mechanical damping of gearbox and generator

The most difficult parameter to identify is the mechanical damping  $c_m$ , which includes the damping effect of each component. In this specific case, there are two main sources of viscous damping, such as the gearbox  $c_{gb}$  and the generator  $c_{DC}$ . It is assumed that the structural damping of the beam is negligible compared to the damping of the gearbox and the generator. To find a reasonable estimation of  $c_m$ , the output voltage of the free oscillations was measured, as shown in Figure 64. In this way, the quantity  $c_{gb}+c_{DC}$  is estimated. The output voltage  $V_{out}$  is proportional to the angular velocity as:

$$v_{out} = GK_t \dot{\theta} \quad (5.27)$$

, where  $G$  is the gear ratio.

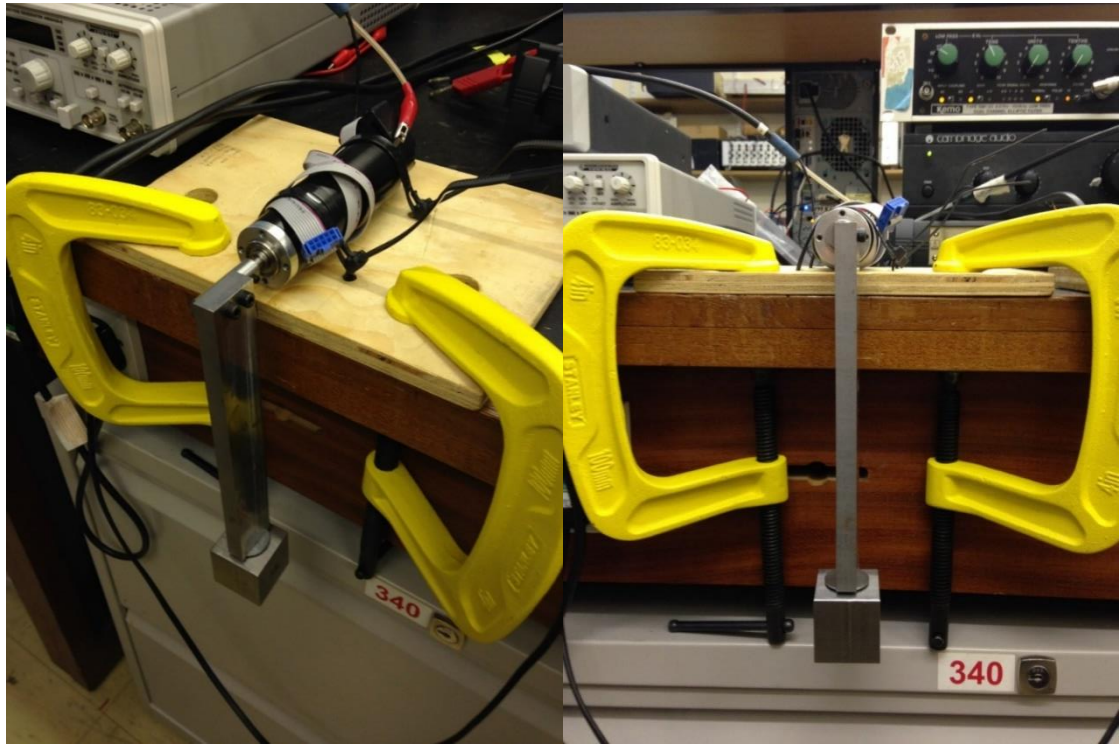


Figure 64: Set up for the measure of the viscous damping

Imposing an initial angular displacement, the absolute value of the free oscillations of the output voltage are shown in Figure 65. The output voltage tends quickly to zero as the velocity reduces due to the parasitic friction inside the gearbox. However, through the design stage, the device is assumed to behave linearly and the effect of the parasitic friction is neglected. Therefore, the value of viscous damping, which is estimating through the output voltage, is the sum of the viscous damping of the gearbox, the generator and also the parasitic friction. Consequently, it is an equivalent viscous damping.

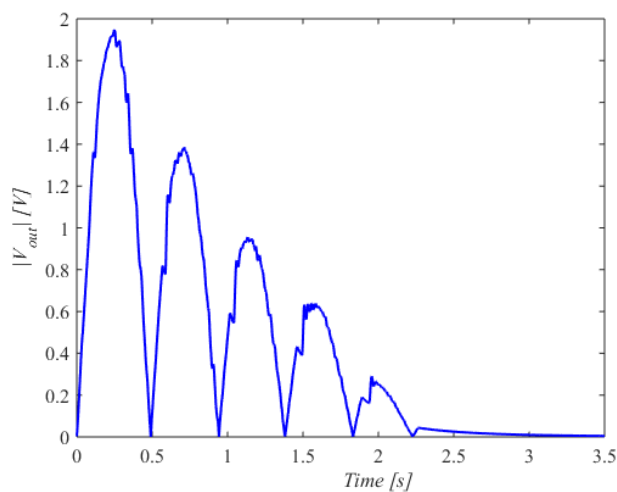


Figure 65: Absolute value of the output voltage vs time - free oscillations

To estimate the equivalent damping, an exponential fitting of the relative maxima of the output voltage is carried out. In Figure 66, the relative maxima are shown in blue star markers and the fitting

in dashed red line. It is clear that at high voltage levels the fitting is very close as the viscous damping dominates the response. As the amplitude decreases, the friction becomes more important and the exponential fitting function does not approximate perfectly the data. The exponent of the fitting function is:

$$v_{out}(t) = V_{out} e^{-\zeta_m \omega_n t} \cos(\omega_d t - \phi) \quad (5.28)$$

,  $\omega_d$  is the damped frequency.

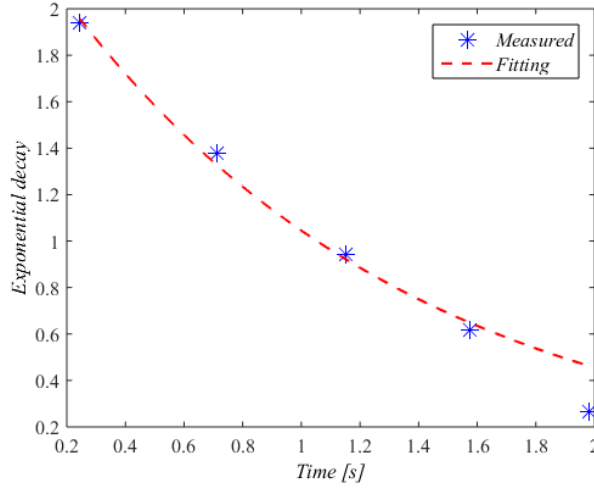


Figure 66: Exponential fitting of the relative maxima of the output voltage - experimental data (blue star markers) and numerical fitting (red dash line)

From the fitting, the damping ratio  $\zeta_m$  is found to be 0.83. The equivalent viscous damping can be computed as:

$$c_m = 2\zeta_m \omega_n J \quad (5.29)$$

, where  $J$  is the moment of inertia of the beam and the lumped mass, as shown in Figure 64. The equivalent viscous damping  $c_m$  of the gearbox and the generator is then 0.196 Nms/rad. Once the viscous damping is known a time domain fitting can be performed to check whether the estimated value for the damping  $c_m$  is acceptable at this early stage.



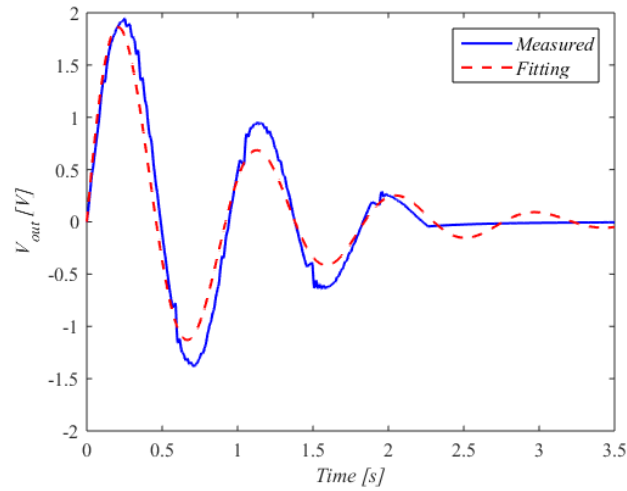


Figure 67: Output voltage vs time - experimental data (blue solid line) and numerical fitting (red dashed line) with an equivalent damping ratio of  $0.83$

From Figure 67, at a first glance, the equivalent damping seems to fit reasonably the experimental data at high voltage levels, but fails as the amplitude reduces. The second oscillation at  $1.2\text{ s}$  presents the highest difference in the amplitude with an error of  $0.25\text{ V}$ . This is due to the friction, which becomes more relevant as the amplitude reduces. Also, it can be noticed that the frequency of the fitting function is higher for the first two periods perhaps due to the geometric nonlinearity associated with the small angle assumption. Indeed, in a pendulum, if the initial condition imposed on the angular displacement is too large, then  $\sin\theta \neq \tan\theta \neq \theta$  and a nonlinear behaviour can be detected. However, as the oscillation reduces, this nonlinearity disappears. In the fitting, this phenomenon is not included as the equation was linearised. A difference of  $0.05\text{ Hz}$  can be detected on the natural frequency. Nevertheless, this nonlinearity will not be present in the final demonstrator because the oscillation will be maintained low, as described in the next sections.

### 5.4.3 Analytical parametrical analysis

The design process is aimed to define the geometrical and the mass properties, highlighted in Figure 63. The procedure to compute the parameters comprises of four steps, which are listed in order hereafter:

1. Defining the input of the analysis: the input data of the parametrical analysis are either measured, such as the input displacement  $y$  and the viscous damping  $c_m$ , or are provided by data sheet of components, such as the gear ratio  $G$  and the internal resistance  $R_i$  and the transduction coefficient  $K_t$  or are imposed, such as the density  $\rho$  of material;
2. Choosing the independent variables and selecting the lower and upper bounds for each parameter;
3. Constructing of a nonlinear algebraic system of equations, which relates the parameters;
4. Defining a criterion for the choice of the optimum solution;

The list of the steps represents the principle the Matlab code is built to perform the parametrical analysis. The parameters are provided in Table 7. In the column ‘Type’, it is indicated whether the parameter is measured (*M*), imposed arbitrarily (*I*), for example, it is chosen to use steel for the beam, therefore the density is imposed, or obtained from data sheet (*S*).

Table 7: Input parameters

<i>Parameter</i>	<i>Value</i>	<i>Type</i>
Density of the beam $\rho$ [kg/m <sup>3</sup> ]	8000	<i>I</i>
Mass of generator and gearbox $m_{DC}$ [kg]	0.5	<i>M</i>
Mass of flange, base, bolts, screws $m_{extra}$ [kg]	1.7	<i>I</i>
Natural frequency $f_n$ [Hz]	7.5	<i>I</i>
Viscous damping $c_m$ [Nms/rad]	0.196	<i>M</i>
Cross section, depth $a$ [m]	0.028	<i>I</i>
Cross section, height $b$ [m]	0.01	<i>I</i>
Input displacement $Y$ [m]	0.004	<i>M</i>
Transduction coefficient $K_t$ [Nm/A]	0.025	<i>S</i>
Internal resistance of the coil $R_i$ [ $\Omega$ ]	0.8	<i>S/M</i>
Gear ratio $G$	18	<i>S</i>
Position of the spring $l_m$	variable	<i>I</i>

For the ‘imposed (*I*)’ parameters, some considerations can be drawn. For example, it is assumed that the beam and the lumped mass are made of mild steel because it is cheap, easy to form and its properties are acceptable for many applications. The mass of the components such as the flange, the base, the screws and the bolt, which do not participate to the dynamics, is fixed arbitrarily.

The depth  $a$  and the height  $b$  are the characteristic dimensions of the cross section of the beam. They are fixed assuming that the stiffness along the vertical direction of motion must be much lower than that in the horizontal direction. Consequently, the flexural modes are considered to be higher than the rigid body motion and interaction is avoided between them. Depending on the position of the spring, the stiffness of the spring changes to maintain the natural frequency  $f_n$  a constant. Different simulations are run for different values of  $l_m$  to evaluate the best choice for the spring.

The second step is to define the independent variables and to determine reasonable bounds for the parameters to estimate. The axial length of the beam  $l$  and the length of the lumped mass  $L$  are assumed to be the independent variables, and consist of 12 equally-spaced values, as indicated in Table 8.

Table 8: Lower and upper bounds of the variable parameters

<i>Lower bounds</i>	<i>Parameter</i>	<i>Upper bounds</i>
0.1	Length of the beam $l$ [m]	0.24
0.01	Length of the lumped mass $L$ [m]	0.05
0.2	Mass of the beam $m$ [kg]	0.5
0.1	Lumped mass $M$ [kg]	0.35
1000	Stiffness $k$ [N/m]	10000

The upper bounds of the lengths of the beam and the lumped mass are chosen according to the size of the upper plate of the shaker. It is desired that the centre of gravity of the harvester falls within the area limited by the upper plate of the shaker, otherwise an overturning momentum can appear, which destabilises the device. The upper bounds of the two masses instead, are a result of the constraint on the total mass, which cannot exceed  $3kg$ .

The third step is to impose a set of equalities linking inputs and outputs. The equalities are given as,

$$m - \rho a b l = 0 \quad (5.30)$$

$$M - \rho L^3 = 0 \quad (5.31)$$

$$l_m - x_{CM} = 0 \quad (5.32)$$

$$k - \left( \frac{2\pi f_n}{l_m} \right)^2 J = 0 \quad (5.33)$$

Equation (5.30) and equation (5.31) link the lengths  $l$  and  $L$  to the mass of the beam  $m$  and the lumped mass  $M$  respectively. Equation (5.32) states that the spring is assumed to be attached at the centre of gravity of the system, however, this parameter will be varied. Equation (5.33) links the inertial and the stiffness properties of the system. The constraints are imposed as follows,

$$\begin{cases} M_{tot} = 3kg \\ 0.02 \leq \zeta_m \leq 0.65 \\ \Theta_{OC} \leq 6deg \end{cases} \quad (5.34)$$

, where  $\Theta_{OC}$  is the amplitude of the angular displacement at the natural frequency in open circuit (no load attached therefore no electrical damping), which can be written as:

$$\Theta_{OC} = \frac{\left( m \frac{l}{2} + M \left( l + \frac{L}{2} \right) \right) \omega_n Y}{c_m} \quad (5.35)$$

The maximum angular displacement will be achieved in open circuit because no electrical damping is present, and it is the most dangerous condition, especially for the spring, which is stretched and compressed at the maximum value.

Running the simulations for four ‘Case’, corresponding to different values of position of the spring  $l_m$  with respect to the centre of gravity, the analytical results are shown in Table 9.

Table 9: Results of the parametrical analysis for different 'Case'

	<b>Case 1</b>	<b>Case 2</b>	<b>Case 3</b>	<b>Case 4</b>
<b>Parameters</b>	$l_m=x_{cm}/2$	$l_m=x_{cm}$	$l_m=(x_{cm}+l)/2$	$l_m=l$
$m$ [kg]	0.4	0.4	0.4	0.4
$M$ [kg]	0.36	0.36	0.36	0.36
$l$ [m]	0.176	0.176	0.176	0.176
$L$ [m]	0.0355	0.0355	0.0355	0.0355
$k$ [N/m]	8160	2040	1580	1260
$M_{tot}$ [kg]	2.95	2.95	2.95	2.95
$\zeta$ [-]	0.12	0.12	0.12	0.12
$x_{cm}$ [m]	0.138	0.138	0.138	0.138
$\Theta_{OC}$ [deg]	6	6	6	6

The solutions in Table 9 represent the optimum solution in terms of power harvested for each 'Case' at the natural frequency.

As expected, the only parameter changing according to the position of the spring is the stiffness (the row is highlighted in red colour), because to maintain  $f_n$  constant, as  $l_m$  increases, the spring becomes softer. This can be inferred from the last equation of the system (5.30). Theoretically, all the solutions are acceptable as they are complied with the imposed constraints. To select the final solution, the deflection of the spring is calculated, to be sure that the compression does not reach values that can damage the spring.

The static deflection  $\delta_{st}$  is obtained from the static equilibrium position as:

$$M_{tot} g x_{CM} = k l_m \delta_{st} \quad (5.36)$$

The maximum dynamic deflection is the maximum displacement of the spring throughout a period of oscillation. From Table 9, the angular displacement  $\Theta_{OC}$  in open circuit is 6 deg, the maximum dynamic deflection due to this angular displacement can be calculated as:

$$\delta_{dyn} = l_m \sin \Theta_{OC} \quad (5.37)$$

In Table 10, the static and the dynamic deflection for each of the 'Case' is reported.

Table 10: Static and dynamic deflection for different 'Case'

	<b>Case 1</b>	<b>Case 2</b>	<b>Case 3</b>	<b>Case 4</b>
<b>Parameters</b>	$l_m=x_{cm}/2$	$l_m=x_{cm}$	$l_m=(x_{cm}+l)/2$	$l_m=l$
$\delta_{st}$ [m]	0.0018	0.0036	0.0041	0.0046
$\delta_{dyn}$ [m]	0.0069	0.0137	0.0156	0.0175

If the natural frequency maintained constant, the response of the system at resonance in terms of angular displacement does not depend on the stiffness or the position of the spring, as demonstrated in equation (5.35). Nevertheless, the deflection of spring changes. Using a linear spring in this application implies that for large angular displacement the spring bends. This may cause different undesired phenomena, such as an increment of the stiffness due to residual stresses or an introduction

of nonlinearity in the stiffness force. Therefore, ‘Case 3’ and ‘Case 4’ are neglected as they provide large deflections if compared to the free length of the spring, which will be around  $0.1m$ . However, attaching the spring close to the hinge implies a high stiffness, for example  $k=8160N/m$  for the ‘Case 1’. This may damage the device, because such a stiff spring would transmit high frequency vibrations to the gear shaft ( $6\text{ mm}$  of diameter). It is decided to attach the spring between the ‘Case 1’ and the ‘Case 2’. The position of the spring is fixed at  $l_m=0.077m$  and, consequently, the stiffness becomes  $k=6600\text{ N/m}$ . The dynamic deflection is  $0.0076\text{ m}$ , which means that is roughly the  $13\%$  of the free length of the spring  $0.1m$ . This value is to make sure that the lumped mass does not hit the wooden base during the motion.

Two types of spring can be selected for the system, such as cylindrical tension or compression springs. For the device proposed here, both can be suitable. The main advantage of a tension spring is that it is unlikely to buckle. Nevertheless, the application of such a spring would imply the use of a fixed frame all around the structure so that the other end of the spring can oscillate beyond the free length and can operate in a tension state, as shown in Figure 68.

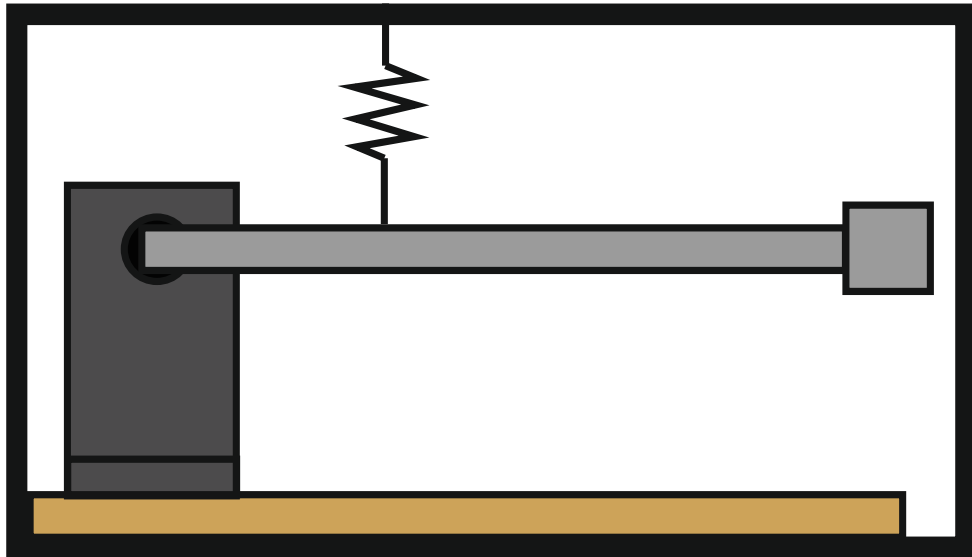


Figure 68: A schematic representation of the energy harvesting with tension spring

However, the extra weight associated with the frame is undesired and, therefore, the compression spring is used. The supplier is Lee Spring, and from the catalogue, a spring with end coils closed and ground is chosen, as their main property is to reduce the buckling. The specifications are provided in Table 11.

Table 11: Lee Spring specifications

<i>Part number</i>	<i>Outside diameter</i>	<i>Hole diameter</i>	<i>Wire diameter</i>	<i>Free length</i>	<i>Stiffness <math>k</math></i>
LC 092H 15 S	$0.0152\text{ m}$	$0.0158\text{ m}$	$0.0023\text{ m}$	$0.095\text{ m}$	$6750\text{ N/m}$

The stiffness has to be as close as possible to the computed value to ensure the resonance frequency is  $7.5\text{Hz}$ . Also the free length of the chosen spring fits perfectly with the imposed value of  $0.1m$ .

Once, the spring is chosen, it has to be verified that the buckling does not occur. The buckling is a function of the slenderness ratio, which is the ratio between the free length and the mean diameter. In this case, this ratio equals 6.13. In [76], from the buckling curve for compression spring, it turns out that buckling occurs when the deflection is of  $0.038m$ , which is 4.5 times higher than what occurs in this application, and, therefore, no buckling phenomenon is expected to take place.

## 5.5 Manufacturing process

The manufacturing process begins, when all the drawings (2D and 3D) are delivered to the manufacturer. In Figure 69, the CAD 3D model is shown. The manufacturer is the EDMC workshop of the University of Southampton. The manufactured device is expected to differ from the optimised device. The reason is that the dimensions of beams and bars are usually standardised and, in addition, the availability of materials is limited. Therefore, some of the parameters are very similar, but not equal to the result of the analytical parametrical analysis. Consequently, the design has to be slightly modified according to the availability of the workshop, even though the dynamic characteristics, such as the natural frequency, have to remain the same. The drawings are shown in Appendix III.

In Table 12, the manufacturing set of parameters is compared with the analytical results set of parameters and the CAD model is shown in Figure 69.

Table 12: Analytical and manufacturing set of parameters

<i>Parameters</i>	<i>Analytical</i>	<i>Manufacturing</i>
$m$ [kg]	0.4	0.435
$M$ [kg]	0.36	0.333
$l$ [m]	0.176	0.185
$L$ [m]	0.0355	0.0355
$l_m$ [m]	0.077	0.077
$b$ [m]	0.01	0.01
$a$ [m]	0.028	0.028
$k$ [N/m]	6750	6750
$M_{tot}$ [kg]	2.95	2.96
$\zeta$ [-]	0.12	0.11
$x_{cm}$ [m]	0.138	0.14
$f_n$ [Hz]	7.5	7.45
$\theta_{OC}$ [deg]	6	5.95

As shown in Table 12, there is a small difference between the analytical and the manufactured device.

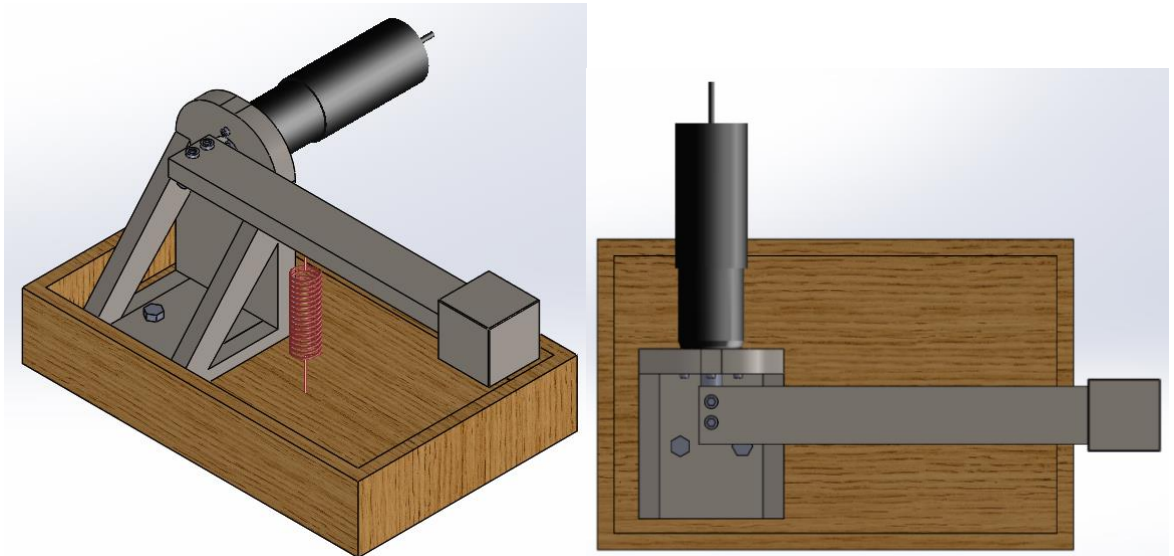


Figure 69: CAD model – isometric view (left) and upper view (right)

Once the manufacturing is completed and the manufacturing parameters (in Table 12) are known, the CAD can be updated and a finite element analysis can be run to verify if the first resonant frequency corresponds to  $7.5\text{Hz}$ , which is one of the input parameters (in Table 7) of the parametrical design.

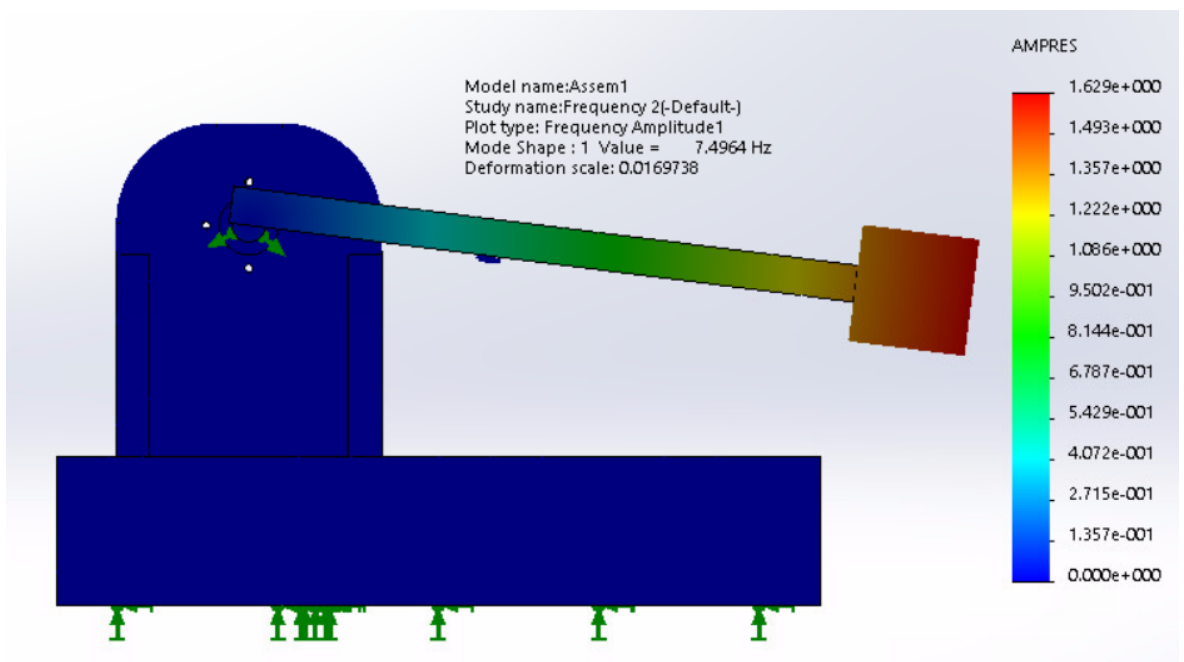


Figure 70: FEM of the energy harvester - the model shows that the parameters obtained from the design produces a first resonant frequency at  $7.5\text{ Hz}$

As shown in Figure 70, the FEM perfectly agrees with the parametrical study and predicts the first natural frequency at  $7.5\text{Hz}$ . The boundary conditions are imposed equal to the boundary conditions of the experiments, therefore the base is clamped onto the shaker, and the only degree of freedom is the rotation of the beam about the axis of the generator.

In Figure 71, the manufactured device is mounted onto the shaker and the set up for the experiments is prepared.

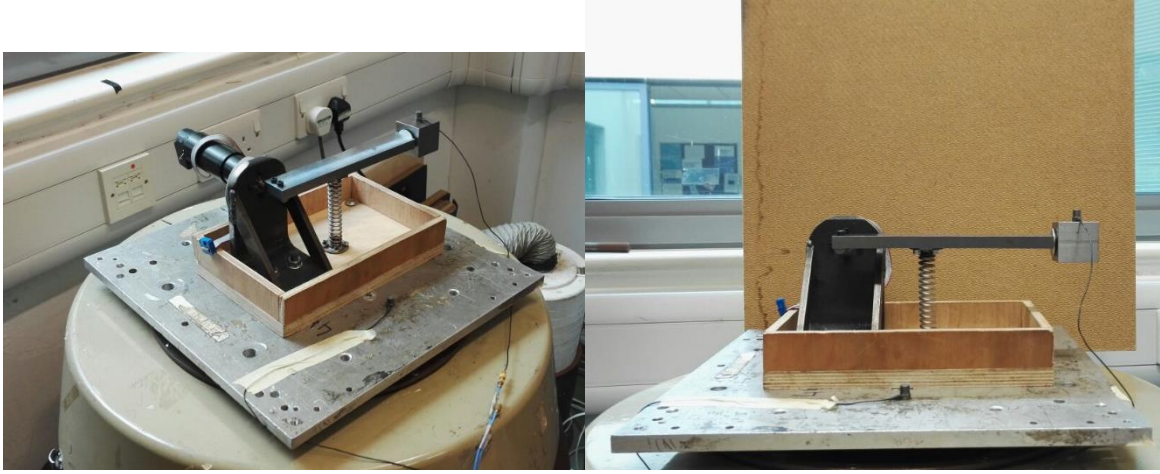


Figure 71: Manufactured device – isometric view (left), front view (right)

## 5.6 Optimum load of the harvesting device

In Chapter 3, that there exist an optimum load for which the harvested power is maximised. This characteristic allows the level-dependent strategy to be effective, especially when the input level is variable. However, in Chapter 3, the assumption of  $R_i=0$  was made, which is no longer valid now as the motor has an internal resistance of  $0.8\Omega$ . To be able to implement the level-dependant strategy, the optimum load has to be computed. In literature [23,24], if the harvester has a limited relative displacement and is harmonically excited, an analytical expression for optimum load can be obtained. In detail, if the energy harvester is excited at the maximum input level, then the relative displacement reaches the maximum acceptable value and a further increment of input cannot be followed by a further increment of the relative displacement. According to this, the power harvester can be written as:

$$P_{ave} = \frac{1}{2} G^2 \frac{K_t^2 R_l}{(R_i + R_l)^2} (\omega_n \Theta_{LC,max})^2 \quad (5.38)$$

, where  $\Theta_{LC,max}$  is the maximum angular displacement in load circuit (thus, when a load is attached) when  $Y=Y_{max}$ . By taking the derivative of equation (5.38) with respect to electric load  $R_l$ , and making it equal to zero, it results in:

$$\left. \frac{\partial P_{ave}}{\partial R_l} \right|_{\Theta=\Theta_{max}} = 0 \Rightarrow R_l = R_i \quad (5.39)$$



When a constraint on the maximum relative displacement is imposed, the optimum load has to be equal to the internal resistance to maximise the harvested power. If instead there is no constraint on the displacement, the harvested power becomes:

$$P_{ave} = \frac{1}{2} G^2 \frac{K_t^2 R_l}{(R_i + R_l)^2} (\omega_n \Theta_{LC})^2 \quad (5.40)$$

, where  $\Theta_{LC}$  is now not constant but equal to

$$\Theta_{OC} = \frac{(m l/2 + M(l + L/2)) \omega_n Y}{c_m} \quad (5.41)$$

. By taking the derivative of equation (5.40) with respect to electric load  $R_l$ , and making it equal to zero, it results in:

$$\left. \frac{\partial P_{ave}}{\partial R_l} \right|_{\Theta=\Theta_{max}} = 0 \Rightarrow R_l = R_i + \frac{K_t^2}{c_m} \quad (5.42)$$

, which is in agreement with the results found in literature. Although, from the theoretical point of view, the equation (5.42) differs from equation (5.39), practically in this case, they yield the same result. Indeed, the available generator has a low transduction coefficient and, consequently, the term  $K_t^2/c_m$  is small. By plotting in Figure 72, the harvested power as a function of the load equation (5.39) is confirmed and the optimum load is equal to the internal resistance  $0.8\Omega$ .

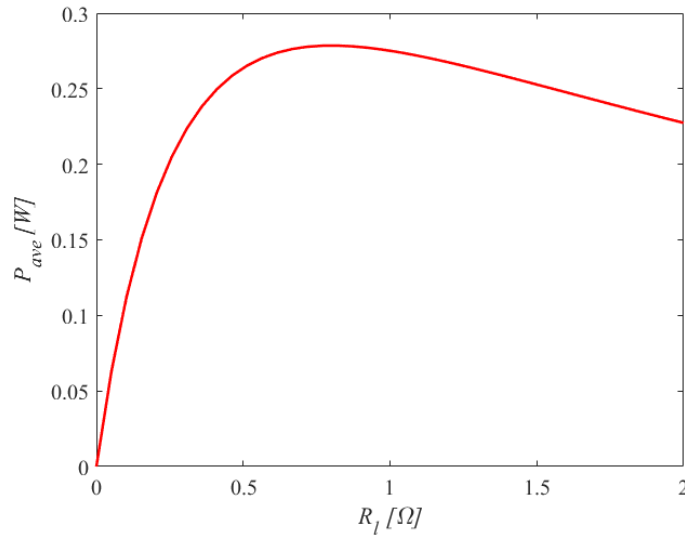


Figure 72: Average harvested power as a function of the shunt load when the input displacement is maximum

At the maximum input level  $Y_{max}$ , the harvester is complied with constraint on the maximum angular displacement  $\Theta_{OC}=6deg$ . This is because the parametrical design was done considering the worst-case scenario (when we have  $\Theta_{OC}$ ), which corresponds to have only mechanical damping and no

electrical damping due to the shunt. Therefore, we can always operate at the optimum load because the constraint are always satisfied. In case this will not be possible, the level-dependent load strategy can be applied. As an example, we assume that the maximum angular displacement has to be reduced from  $3.6deg$  to  $2.8deg$ . The amplitude of the angular displacement is shown in Figure 73.

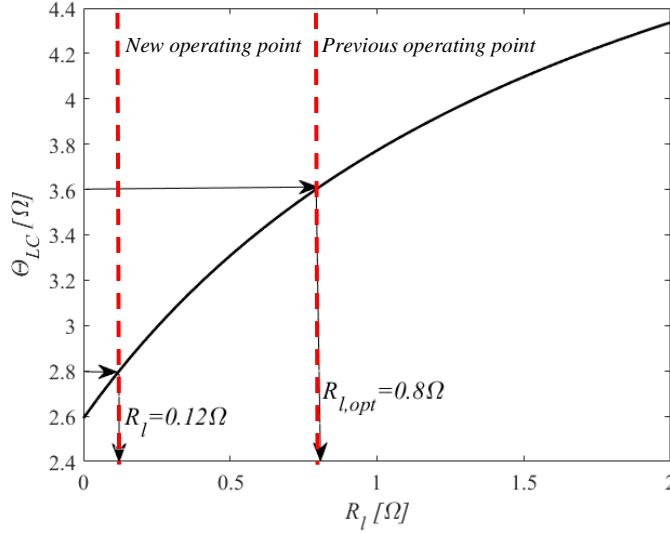


Figure 73: Angular displacement in load circuit as a function of the shunt load when the input displacement is maximum – by reducing the constraint on the maximum angular displacement from  $3.6deg$  to  $2.8deg$ , it can be noticed that the shunt load has to decrease up to  $0.12\Omega$

The new value of shunt load, which enable to be complied with the constraint of  $2.8deg$ , follows:

$$R_l = \frac{K_t^2 \Theta_{LC}}{\left[ m \frac{l}{2} + M \left( l + \frac{L}{2} \right) \right] \omega_n Y - \Theta_{LC} c_m} - R_i \quad (5.43)$$

The new value can be varied according to the input level, as show in Figure 74.

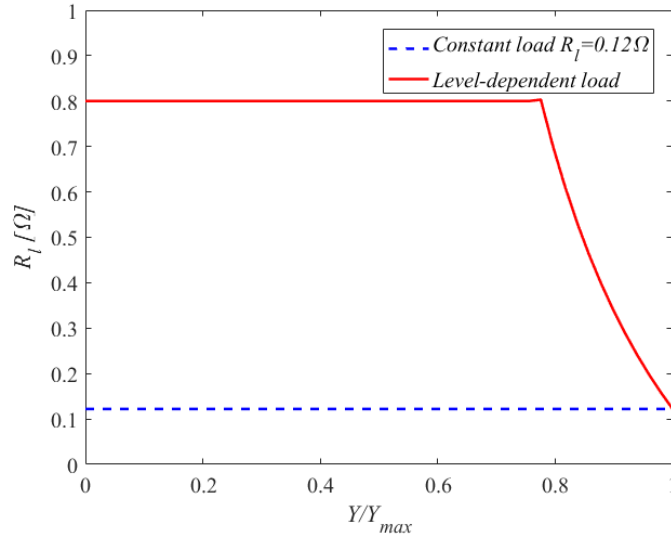


Figure 74: Shunt load as a function of the normalised input amplitude  $Y/Y_{max}$  - constant shunt (dashed blue line) and a level-dependent shunt (solid red line)

In Figure 75 (left), the effect of a level-dependent load is shown. The shunt load is adjusted until the optimum is achieved and then is maintain constant. The power, in Figure 75 (right), produced from a level-dependent load, has a different trend compared to what was shown in Chapter 3. The reason is that now an internal resistance was considered, which changes the shape of the power function.

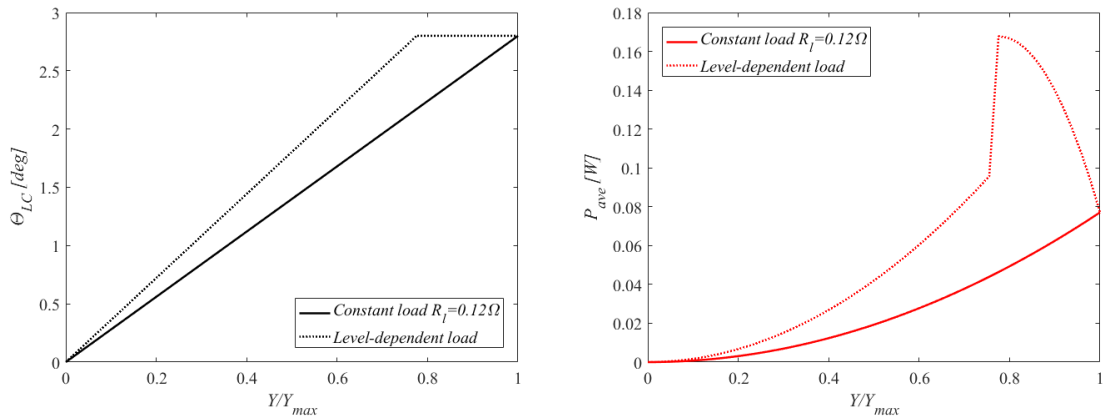


Figure 75: Level curves of the angular displacement  $\Theta_{LC}$  (left) and average harvested power  $P_{ave}$  (right) for a constant (solid line), and a variable (dotted line) load as a function of the normalised input amplitude  $Y/Y_{max}$

The power is no longer quadratic but is a function of the load and the input level at same time. The trend of the power function can be formalised as follows:

$$\begin{cases} P_{ave} \propto Y^2 \Leftrightarrow R_l = R_{l,opt} \\ P_{ave} \propto \frac{R_l}{(R_l + R_i)^2} \Leftrightarrow R_l < R_{l,opt} \end{cases} \quad (5.44)$$

## 5.7 Summary

In this chapter, the design process for the proposed energy harvesting device was described. The device consists of an oscillating beam sprung to the ground, which is coupled with a gearbox and a generator. An imposed base displacement induces the oscillation of the beam, which in turn, generates the rotation of the generator shaft. The generator produces output voltage, which is converted to harvested power. The device is aimed to be tested onto a shaker and, consequently, the design is influenced by practical limitations of the shaker, such as the amplitude of the base displacement and the frequency of excitation. Due to design constraints, for example the natural frequency, which has to match with the excitation frequency, and the maximum displacement of the beam to avoid buckling of the spring, the characteristics of the device (mass and stiffness properties) were optimised. The 3D model and the 2D drawings allowed the manufacturing of the energy harvester and the FEM showed good agreement with the parametrical study. The device is aimed to demonstrate that a level-dependent load can be more effective than a constant load. Therefore, at the end of the chapter, analytical results are shown, in which the angular displacement and the average harvested power of a system with a constant load and a level-dependent load are compared.

In the next chapter, the device will be tested and the advantage of a variable shunt load will be highlighted compared to a constant load.

## Chapter 6: Experimental tests on the energy harvesting device

### 6.1 Introduction

In this chapter, the experimental results of the manufactured energy harvesting device are presented [77]. The theoretical analysis in Chapter 3 showed that a variable shunt load could enlarge the range of performance of a harmonically excited energy harvester, in terms of the harvested power. If the device cannot operate at the optimum load due to the physical constraints, then the load is thought to be level-dependant, in order to adjust the amplitude of the angular displacement; in particular, the electric load increases as the input level reduces until the optimum load is achieved and the device becomes no longer level-dependant. The present chapter is aimed to characterise the behaviour of the device and qualitatively validate the numerical results in Chapter 5. A quantitative correlation between the experimental results and the analytical and numerical result is not carried out due to the strong dynamics of the gearbox, which has an effect on the dynamics of the harvester. It would require including into the model of the energy harvester, shown in Chapter 5, also a dynamic model of the gearbox. This aspect will be consider as part of future work.

The first part of this chapter focuses on the experimental set up and describes the equipment used. The second part investigates the presence of nonlinearity in the mechanical system when the electrical circuit is not coupled. In the third part, an electric load is attached across the terminals of the generator, and its effects on the dynamics of the device are described. The fourth part concentrates on validating the results obtained in Chapter 3, and a level-dependant load is implemented.

### 6.2 Experimental set up

The experiments are carried out at the Human Factor Research Unit at the University of Southampton as the they could supply the shaker for the base excitation. The set up for the test of the energy harvester consists of several devices, as listed in Table 13.

Table 13: Equipment used for the measurements

<i>Equipment</i>	<i>Model</i>	<i>Parameter</i>
<i>Shaker</i>	<i>Derritron Type VP85</i>	
<i>Amplifier</i>	<i>Gearing &amp; Watson SS 300</i>	
<i>Accelerometer 1 (installed on the beam)</i>	<i>B&amp;K Type 4375 V</i>	<i>Resonant frequency: 55 kHz Bandwidth: 0.1-16500 Hz Sensitivity: 0.325 pC/m/s<sup>2</sup></i>
<i>Accelerometer 2 (installed on the base)</i>	<i>B&amp;K Type 4375 V</i>	<i>Resonant frequency: 55 kHz Bandwidth: 0.1-16500 Hz Sensitivity: 0.322 pC/m/s<sup>2</sup></i>

<i>Charge amplifier (one for each accelerometer)</i>	<i>B&amp;K type 2635</i>
<i>Signal generator/Data acquisition system</i>	<i>LMS SCADAS Mobile SCM01 8 Channels</i>

The signal generator generates the voltage signal required, for example sine wave, which is sent to the power amplifier. The signal is amplified by a gain, which is maintained fixed for all the measurements (thus, the position of the knob does not change). The input signal is then fed into the shaker, which provides the base acceleration. Two charge accelerometers are mounted: one is attached onto the base, as shown in Figure 76(left), and it is called accelerometer 1, while the other is attached onto the lumped mass and is called accelerometer 2, and is shown in Figure 76(right). From the accelerometer 1, it will be possible to compute the input displacement of the shaker.



Figure 76: Accelerometer 1 attached onto the base (left) and accelerometer 2 attached onto the lumped mass (right)

The signal gained by each accelerometer is then sent to the charge amplifiers, which converts the signal into acceleration, velocity or displacement depending on the choice of the low pass filter. For the frequency bandwidth of interest, it is chosen to set the filter to ‘acceleration’ with cut-on frequency at  $1\text{Hz}$  and cut-off at  $1\text{kHz}$ . The acceleration ( $m/s^2$ ) is sent to the acquisition system, where it is displayed and saved. For the time domain acquisitions, 5 channels are usually used. The first channel records the output of the signal generator to verify that the required signal has the correct amplitude and frequency. The second channel records the output of the amplifier, which is the input of the shaker, to make sure the imposed gain does not change. This is very important to ensure the amplifier does not saturate. When the input voltage of the amplifier is too high, the amplifier may saturate, and the gain is automatically reduced. The accelerometers 1 and 2 are connected to the third and the fourth channels respectively. The fifth channel records the voltage across the electric resistance and is only used when it is in open or load condition. A schematic representation of the setup is shown in Figure 77.

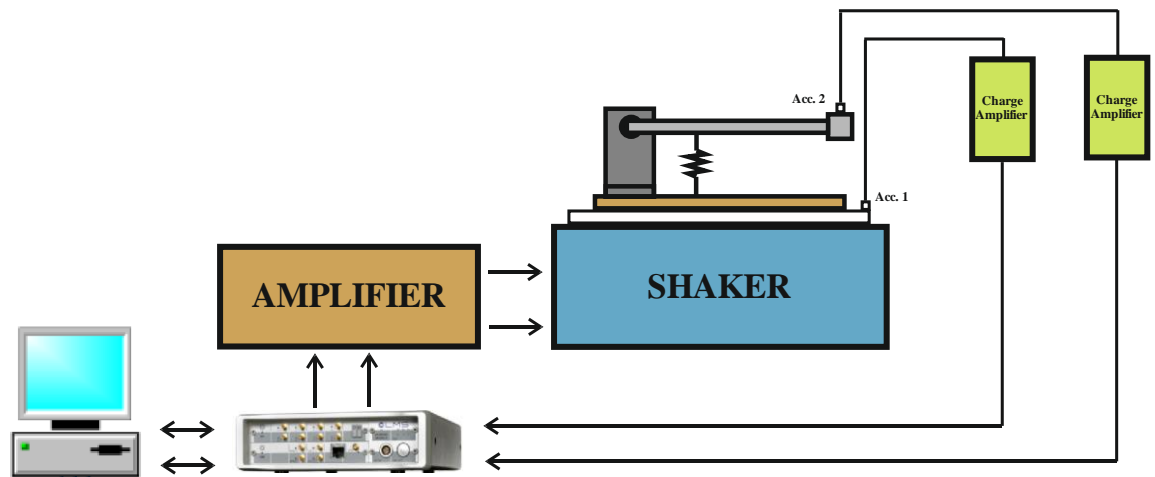


Figure 77: Schematic representation of the set up

It is assumed that the power harvested is equal to the power dissipated across an electrical resistor (load). Therefore, the harvesting process can only take place when a load is attached across the terminals of the generator. As a load, a digital potentiometer is provided, which enables to vary the value of the resistor by rotating the shaft at the top, as shown in Figure 78.

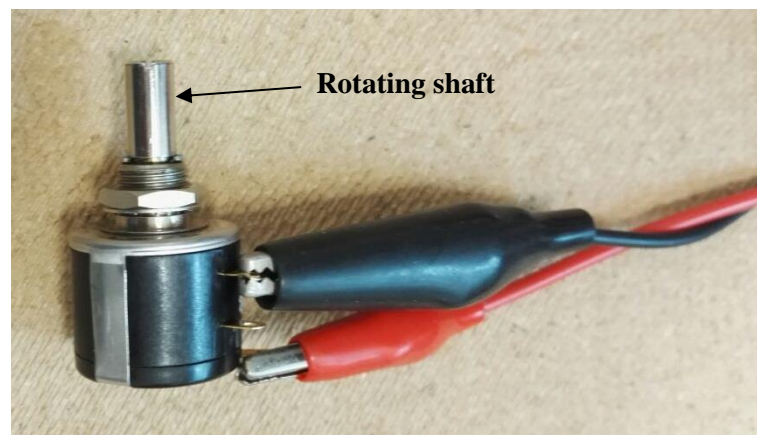


Figure 78: Load circuit condition, the terminals of the generator are connected to a digital potentiometer

This situation is called load circuit condition. Nevertheless, other two conditions are tested: open circuit and short circuit. In open circuit, Figure 79 (left), the harvested power is zero because the terminals of the generator are not connected to a load. As the circuit is open, the current does not flow, but still voltage can be measured across the terminals.

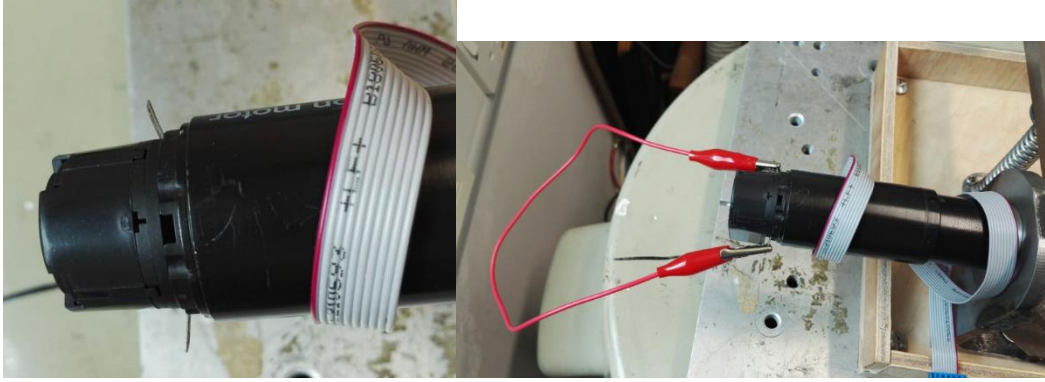


Figure 79: Open circuit condition (left), the terminals are not connected and short circuit (right) condition, a crocodile connects the terminals

The harvested power is zero also in short circuit, because a ‘crocodile’ directly connects the terminals and no load is interposed between them. In this case, the circuit is closed, and consequently, the current flows. Nevertheless, the voltage across the terminals is zero. This condition is shown in Figure 79(right).

The introduction of an electrical load introduces a certain amount of damping into the structure. Clearly, depending on the condition (open, short, load) described previously, the electrical damping changes. In load circuit, the electrical damping  $c_e$ , which is due to the internal resistance of the coil  $R_i$  and load resistance  $R_l$ , is:

$$c_e = \frac{K_t^2}{R_i + R_l} \quad (6.1)$$

In open circuit, the load resistance  $R_l$  can be assumed infinite, and consequently, equation (6.1) becomes:

$$c_e = 0 \quad (6.2)$$

In this situation, only the mechanical damping affects the dynamics. In short circuit, the load resistance is zero and equation (6.1) turns to be:

$$c_e = \frac{K_t^2}{R_i} \quad (6.3)$$

Short circuit condition is characterised by the largest amount of electrical damping. These considerations will be confirmed experimentally in section 6.4. In Table 14, the electrical quantities are summarised as a function of the operative conditions.



Table 14: Electrical quantities for the three operative conditions

<i>Operative condition</i>	<i>Load resistance <math>R_l</math></i> [ $\Omega$ ]	<i>Current <math>I</math> [A]</i>	<i>Voltage <math>V</math></i> [V]	<i>Electrical damping <math>c_e</math></i> [Nms]	<i>Harvested power</i> $P_{ave}$ [W]
<i>Open circuit</i>	$\infty$	0	$>0$	0	0
<i>Load circuit</i>	$>0$	$>0$	$>0$	$\frac{K_t^2}{R_i + R_l}$	$>0$
<i>Short circuit</i>	0	$>0$	0	$\frac{K_t^2}{R_i}$	0

In the next section, the presence of the nonlinearities is investigated. From the electrical point of view, the generator behaves in a linear manner, therefore, if nonlinearities appear, they are mainly due to the mechanical system. For this reason, this analysis will be carried out in open circuit.

### 6.3 Detection of nonlinearity in the open circuit

During the design stage, it was assumed that the device behaves in a linear manner. Nevertheless, it was pointed out that nonlinearities are present. Parasitic friction represents one of the main sources of loss when dealing with gearbox [74]. This type of nonlinearity, which was modelled in Chapter 3 as Coulomb friction, is complicated to identify with accuracy because it depends on the material, the contact between different parts, the presence of grease or oil, whose performance is, in turn, a function of the environment (for example, humidity and temperature). However, generally speaking, the parasitic friction, and consequently the nonlinearity, tends to increase at low velocities and decreases at high velocities where usually the friction is overcome by the viscous damping, and the system behaves in a linear manner. To detect the presence of friction, a random test is conducted at different input voltage levels and the absolute transmissibility is measured. The absolute transmissibility is defined here as the ratio between the accelerations measured by the accelerometer 2 (on the beam) and the accelerometer 1 (on the base). From the signal generator, an input random noise with a bandwidth of  $5-100\text{Hz}$  is imposed and a number of 40 averages is taken. The number of spectral lines is set to 2048, with a frequency resolution of  $0.0488\text{Hz}$ . The input voltage (output of the amplifier) is varied from  $0.075\text{V}$  to  $0.45\text{V}$ .

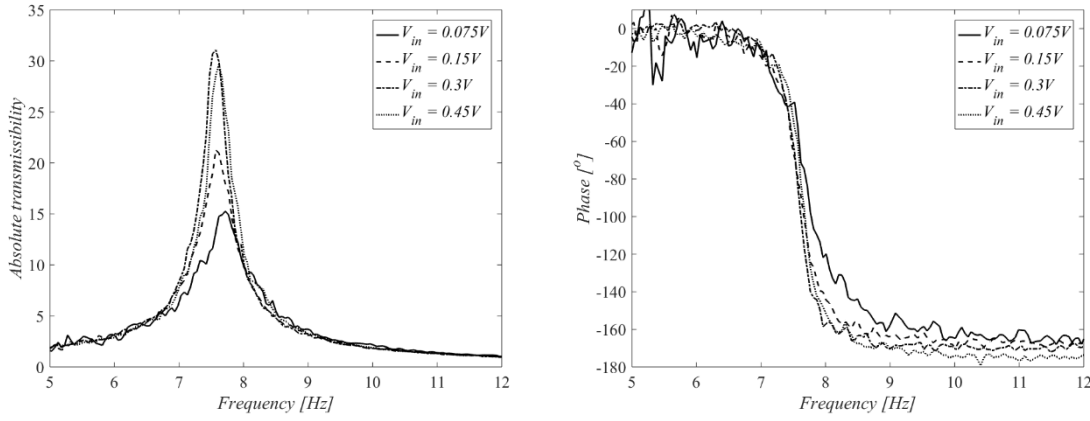


Figure 80: Absolute transmissibility (left) and phase (right) as a function of frequency for different input voltage levels - Presence of friction can be detected at low levels

As expected, when the input is low, the device is affected by the parasitic friction inside the gearbox, as shown in Figure 80(left). From  $0.075V$  to  $0.3V$ , the absolute transmissibility grows, because the effect of the friction decreases. For inputs higher than  $0.3V$ , the absolute transmissibility remains constant as the response becomes linear, and the main source of loss is the linear viscous damping.

From Figure 80(right), it is possible to compute the natural frequency. If it is assumed that the device is operating in a linear regime, for example considering the case  $V_{in}=0.3V$ , the natural frequency can be identified by using the -3dB method. The natural frequency  $f_n$  is found at  $7.57Hz$ . From Figure 80(left), the frequency  $f_r$  corresponding to the maximum amplitude can be obtained, thus  $f_r=7.57Hz$ . The frequency of the maximum peak  $f_r$  is related to the natural frequency  $f_n$  by the following formula

$$f_r = f_n \sqrt{1 - 2\zeta^2} \quad (6.4)$$

, therefore the damping ratio can be calculated  $\zeta_m=0.0491$ . The mechanical viscous damping is then  $0.0868Nms$ . This value of viscous damping is smaller than what estimated in Chapter 5. However, in Chapter 5, the damping was obtained from a free decay, and the fitting was for the response at low amplitude, which is obviously affected by friction. Therefore, the mechanical viscous damping was an equivalent value, taking into account also the friction at low levels of the response. Here, instead, the damping is computed for a high input level where the effect of friction is less apparent. Nevertheless, the system parameters identification, which is not part of the thesis, is added in Chapter 7 as part of future work.

The natural frequency obtained is slightly higher than what predicted in Table 12 ('Manufacturing' column). This increment can be due to an increment of the stiffness. Indeed, for manufacturing and mounting reasons, the spring had to be altered to enable the fastening with the beam and the base. In Figure 81, the spring is shown as it appears before and after the alteration.



Figure 81: Spring as it appears before (left) and after (central) the modifications and zoom of the welded coil (right) - the holes through the disc allow the fastening with screws

To fasten the spring, two discs were welded at the ends of the spring, in particular, at the outer coils (one at each end), as zoomed in Figure 81. This causes an increment of the stiffness [76], as the total number of coils decreases.

As the masses  $M$  and  $m$  and the lengths  $l$ ,  $L$ ,  $l_m$  are known, it is possible to compute the current value of the stiffness, such that the natural frequency is  $7.58\text{Hz}$  (and not  $7.45\text{Hz}$ ).

$$k = \left( \frac{2\pi f_n}{l_m} \right)^2 J \quad (6.5)$$

To have a natural frequency of  $7.58\text{Hz}$  the stiffness has to be  $k=7170\text{N/m}$ . The welding process has increased the stiffness of  $420\text{N/m}$  compared to the sheet value of the supplier.

## 6.4 Electrical coupling: optimum load

In Chapter 5, it was highlighted that the energy harvester should always operate at the optimum conditions. This means either working at the optimum load, for which the harvested power is maximised, or working at the maximum relative displacement without exceeding the physical limit of the device. Therefore, before validating the experimental effectiveness of the variable shunt load, in Chapter 3, the optimum load should be found. When a constraint on the maximum relative displacement is imposed, the optimum load, which maximises the harvested power, should be equal to the internal resistance of the coil, as discussed in literature [21,23,24] and in the previous chapter.

However, during the measurements, the output voltage across the load is recorded, and the averaged harvested power is computed by equation (6.6):

$$P_{ave} = \frac{E[v^2]}{R_l} \quad (6.6)$$

In addition, the output of the shaker is not controlled with a closed-loop feedback; for a harmonic output of the amplifier, the acceleration  $\ddot{y}$  at the base is not perfectly sinusoidal due to an interaction between the device and the shaker (Figure 82(top left and right)), and this interaction increases as the input voltage level increases. Also, the base, the generator and the flange, generates higher harmonic components, which are transmitted to the acceleration  $\ddot{x}$  and the output voltage, as shown in Figure 82(central left and right) and (bottom left and right). If the device is excited at the natural frequency with an input voltage of  $2.4V$ , from Figure 82(top left and right), the amplitude of the input base displacement can be computed. Taking the maximum of the FFT at the fundamental frequency ( $3.31m/s^2$ ) and dividing by  $\omega_n^2$ , the amplitude of the input displacement is  $0.0015m$ .

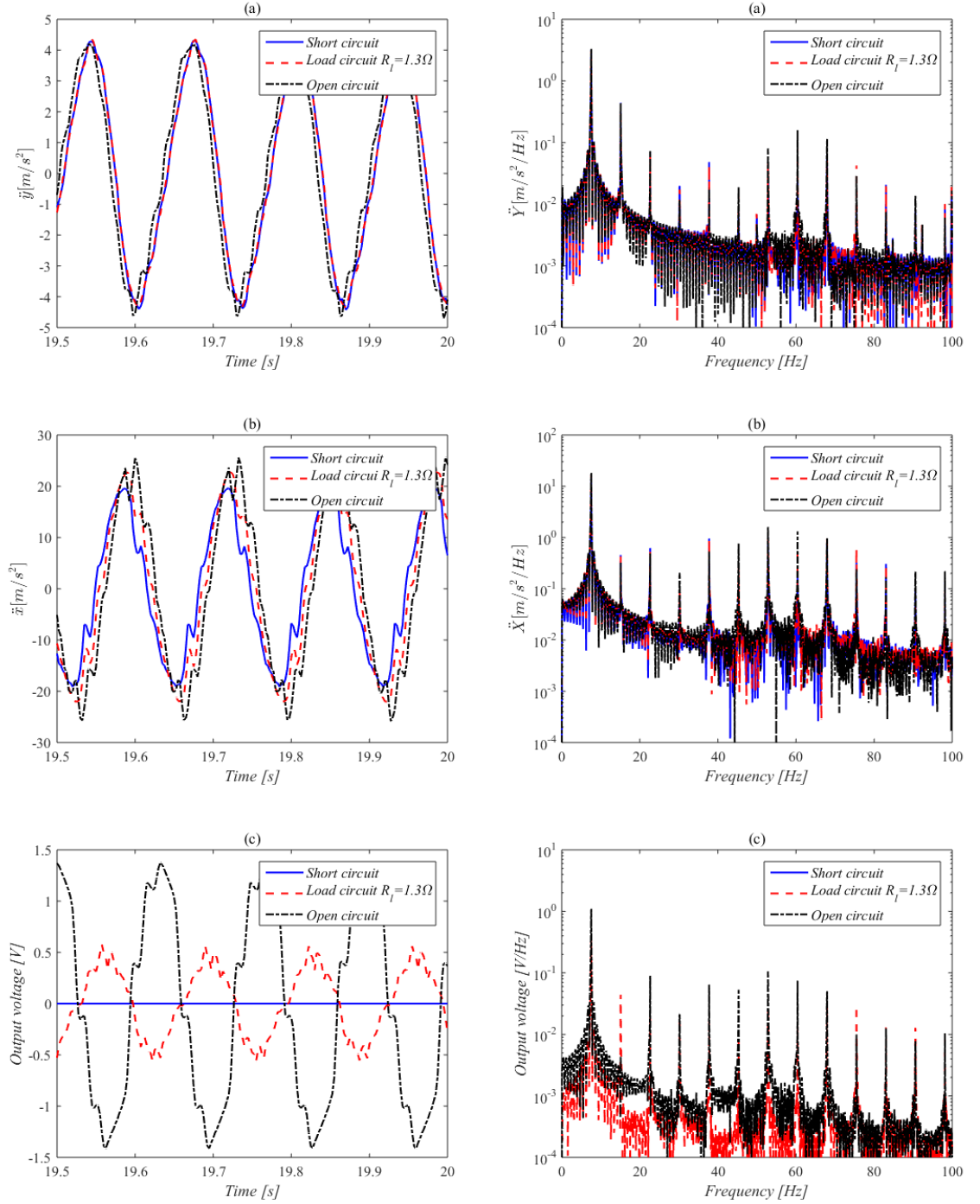


Figure 82: Acceleration  $\ddot{y}$  (top, left and right), acceleration  $\ddot{x}$  (central, left and right) and output voltage (bottom, left and right) in time and frequency domains for a fixed input voltage level (2.4V) and different operative conditions (short circuit, load circuit, open circuit)

The acceleration  $\ddot{x}$  and the output voltage increase as the load increases because the electrical damping reduces; this variation of electrical damping also causes a change in the phase, as clear in the time domain simulations in Figure 82(central left and right) and (bottom left and right).

The amplitude of the angular displacement  $\Theta$  is caused by the relative acceleration between the accelerometer 2 (on the beam) and the accelerometer 1 (on the base), as indicated in equation (6.7).

$$\ddot{z} = \ddot{z} - \ddot{y} \quad (6.7)$$

Integrating twice the relative acceleration with respect to time, the linear relative displacement  $z$  can be obtained. Obviously, the integration tends to reduce the higher frequency components, and consequently the time domain signal is less affected by higher harmonics. Once  $z$  is known, the angular displacement  $\theta$  in time domain can be obtained as:

$$\theta = a \sin \left( \frac{z}{l + L/2} \right) \quad (6.8)$$

The amplitude of linear relative displacement  $Z$  and the angular displacement  $\Theta$  are plotted in frequency domain in Figure 83.

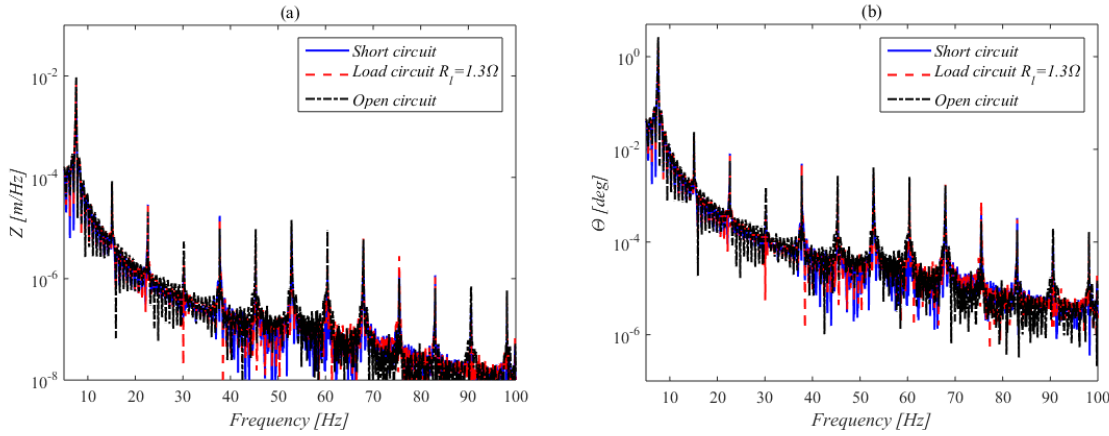


Figure 83: Linear relative displacement  $Z$  (left) and the angular displacement  $\Theta$  (right) in frequency domain for a fixed input voltage level (2.4V) and different operative conditions (short circuit, load circuit, open circuit)

It can be noticed in Figure 83 that the second harmonic at 15Hz (which is the largest among the others) is about two orders of magnitude smaller than the fundamental components, and consequently, its effect can be considered negligible.

Before implementing the variable shunt load, the optimum load should be found. To investigate the effect of electric load on the angular displacement, the output voltage and the harvested power, a set of harmonic tests is run with a fixed input voltage level and different values of  $R_l$ . The acquisition time is set to 20.54s and the sampling time is 0.0025s. The signals, such as the accelerations  $\ddot{x}$  and  $\ddot{y}$  and the output voltage, are recorded in time domain, for an input voltage of 2.4V. The FFT of such signals is computed, and only the amplitude of the fundamental components is considered.

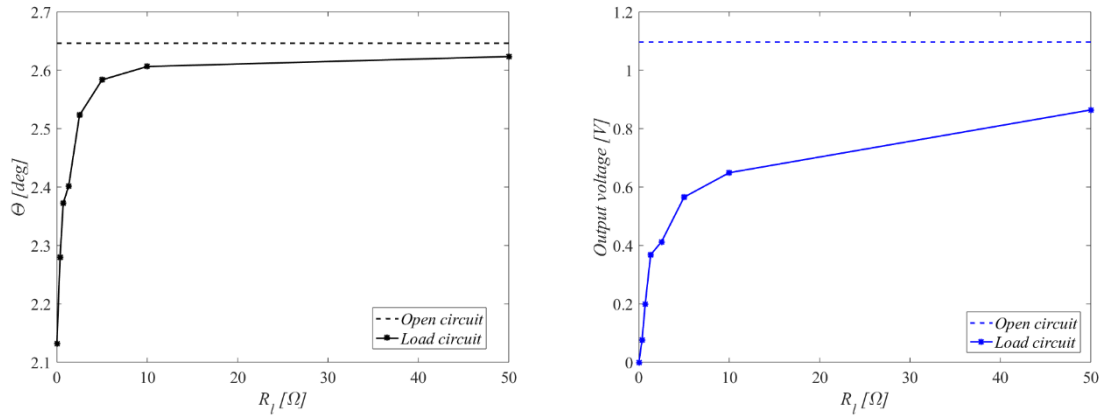


Figure 84: Amplitude of the angular displacement (left) and output voltage (right) as a function of the electric load – harmonic excitation at the natural frequency with input voltage at  $2.4V$

At a first glance, Figure 84(left) and (right) confirm the numerical results described in Chapter 3. According to Table 14, the amplitude of the response is the lowest in short circuit ( $R_l=0$ ) because the electrical damping is maximum, and tends to grow as the load increases. The open circuit condition is a limit condition for which  $R_l \rightarrow \infty$  and the electrical damping is zero. The same trend characterises the output voltage, as it is proportional to the angular velocity; nevertheless, in short circuit, the output voltage is zero because the terminals of the generator are directly connected.

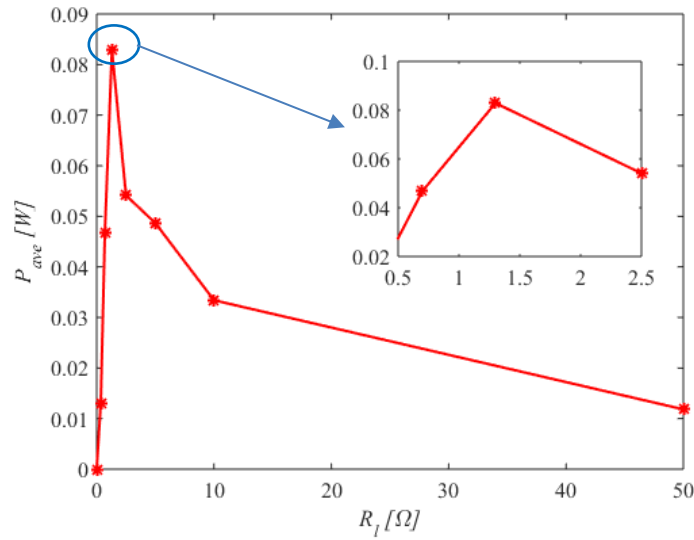


Figure 85: Average harvested power as a function of the electric load – harmonic excitation at the natural frequency with input voltage at  $2.4V$

Previously, it was pointed out that for such a device, the optimum load should correspond to the internal dissipation  $R_i$ . In Figure 85, the optimum load, which maximises the average harvested power is found at  $1.3\Omega$ , while the internal resistance is  $0.8\Omega$ . Such a difference might be due to two aspects; firstly, the optimum load for the current device would be equal to the internal resistance if and only

if the input is harmonic. In Figure 82, it was demonstrated that the input is not exactly sinusoidal but contains higher harmonics. Even though the higher harmonics have a small amplitude compared to the fundamental component, their effect may have caused a small disagreement between the experimental and the analytical value of the optimum load. Secondly, the resolution is not very high to ensure that the peak we found is the real absolute maximum point. However, due to the difficulty of passively tuning the digital potentiometer, the value obtained is assumed to be the maximum peak.

## 6.5 Variation of the input level

As proved in Chapter 3, the deliberate introduction of nonlinearity in the damping force increases the dynamic range of performance of an energy harvesting device. This concept can be applied to those environments in which the input level changes, for example the sea waves or rotating shaft.

Therefore, it is of primary importance to understand how the manufactured device behaves when subjected to a variable input level. The device is subjected to a harmonic excitation at the natural frequency.

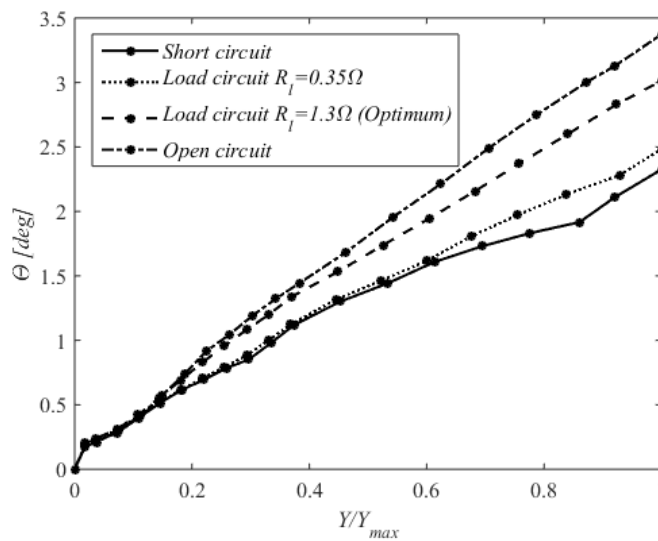


Figure 86: Level curves of the angular displacement  $\Theta$  for different loads such as short circuit (solid line),  $R_l=0.35\Omega$  (dotted line),  $R_l=1.3\Omega$  (dashed line), and open circuit (dash dot line) as a function of the normalised input amplitude  $Y/Y_{max}$

In Figure 86, the open and short circuit conditions represent a sort of lower and upper bound for the angular displacement, corresponding to the maximum and the minimum electrical damping, respectively. All the load conditions are constrained between these bounds. In a linear system, the dependence between input and output is linear and, consequently, these curves are straight lines, with different slope, depending on the load. For the present case of study, the device behaves in a linear manner until the input level is very low ( $Y/Y_{max}=0.02$ ), where a significant drop is evident. This decrement is due to the parasitic friction, which occurs at low input level, and causes the motion to



stop. In addition, it can be noticed that the angular displacement, in open circuit, is complied with the bounds imposed during the design process and shown in Table 12. At the maximum input level, the angular displacement was calculated to be  $6deg$ , while here is  $3.4deg$ . However, during the design stage, it was considered an input displacement of  $4mm$ , while through the experiments, for safety reason, an amplitude of  $2mm$  is achieved, therefore it was expected to have an output of about the 50% lower. Due to the proportionality between input and output, it can be assumed that if the device was excited with  $4mm$  of input displacement, the angular displacement would be  $6.8deg$  and larger than  $6deg$ . This difference is probably due to the fact that the friction was not considered, throughout the design stage. The same trend can be detected when observing the output voltage in Figure 87.

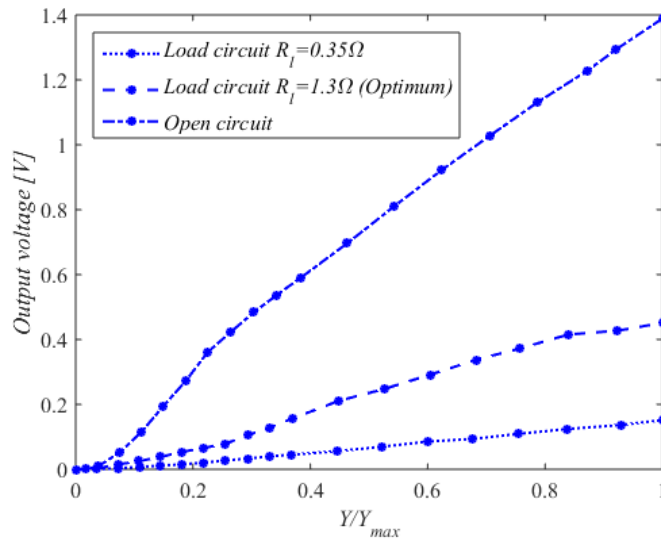


Figure 87: Level curves of the output voltage for different loads such as  $R_l=0.35\Omega$  (dotted line),  $R_l=1.3\Omega$  (dashed line), and open circuit (dash dot line) as a function of the normalised input amplitude  $Y/Y_{max}$  – the short circuit is not reported as the output voltage is zero

The output voltage is affected by the input level similarly to the angular displacement. The output voltage is proportional to the angular velocity, which, in turn, is linearly dependent on the input level. There is an increment of output voltage as the load increases; however, only by shunting a load across the terminals of the generator, the harvesting process power can begin.

In section 6.4, it was explained that the load circuit condition is the operating condition for energy harvesting. In addition, it was demonstrated experimentally, in Figure 85, that there exists an optimum value of the load, which maximises the harvested power. The average harvested power as defined in equation (6.6), is plotted in Figure 88, for two different loads of  $R_l=0.35\Omega$  and  $R_l=1.3\Omega$ .

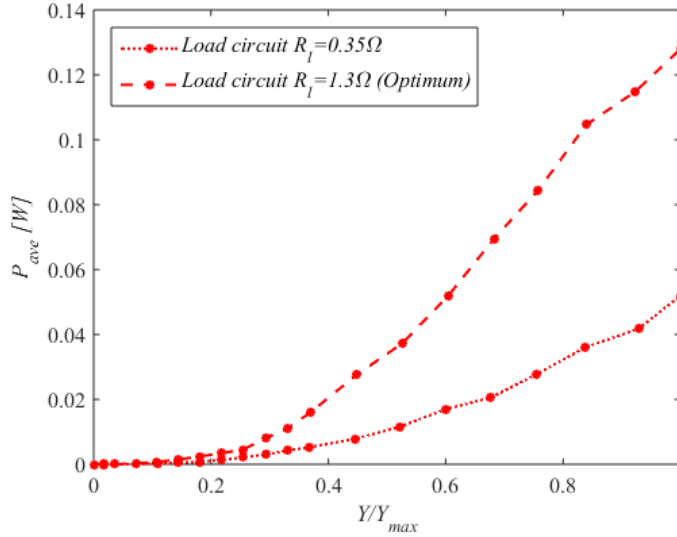


Figure 88: Level curves of the average harvested power for different loads such as  $R_l=0.35\Omega$  (dotted line),  $R_l=1.3\Omega$  (dashed line) as a function of the normalised input amplitude  $Y/Y_{max}$  – the short circuit and the open circuit are not reported as the power is zero

The average harvested power depends on the square of the angular displacement (and the derivatives of the angular displacement as clear from equation (6.6)). Consequently, it is a square function of the input displacement. The power generated by the optimum load is higher than any other load condition. However, in certain conditions, it is not possible to operate at the optimum load because it would imply the output response to exceed the physical limit of the device. In this conditions, the level-dependent load can be implemented.

## 6.6 Maximisation of the harvested power via variable shunt load

In Section 3.8, a new approach was proposed to improve the power for those situations in which the device has a limit on the maximum displacement. As the displacement is limited, operating at the optimum load may not be acceptable because this physical limit can be exceeded. Therefore, a normal strategy would consist of choosing another value of load such that the displacement is complied with the constraint. Even though this approach guarantees the correct functionality, the harvested power drops dramatically. If, for example, the angular displacement cannot exceed  $2.5deg$  at the maximum input  $Y_{max}$ , then it turns out that the load should be equal to  $0.35\Omega$ . In terms of average harvested power, operating at  $0.35\Omega$  causes a large decrement of power compared to the optimum load (see Figure 88). Here the load resistance is a level-dependant parameter, which is adjusted according to the input  $Y$  to maintain the maximum angular displacement  $\theta_{max}$ . In particular, when the input decreases, the load increases, as shown in Figure 90, so that the electrical damping reduces, and consequently, the response, in Figure 89, is kept at the maximum value  $\theta_{max}$ .

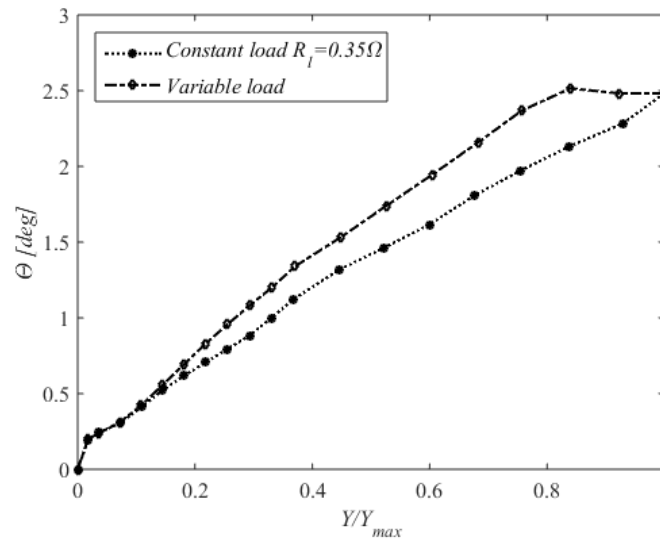


Figure 89: Level curves of the angular displacement  $\Theta$  for a constant (dotted line), and a variable (dotted line) load as a function of the normalised input amplitude  $Y/Y_{max}$

This procedure is carried out until the optimum load is achieved at  $Y/Y_{max}=0.82$ ; then, the load is no longer varied and the system reduces linearly with the input level, as shown in Figure 90.

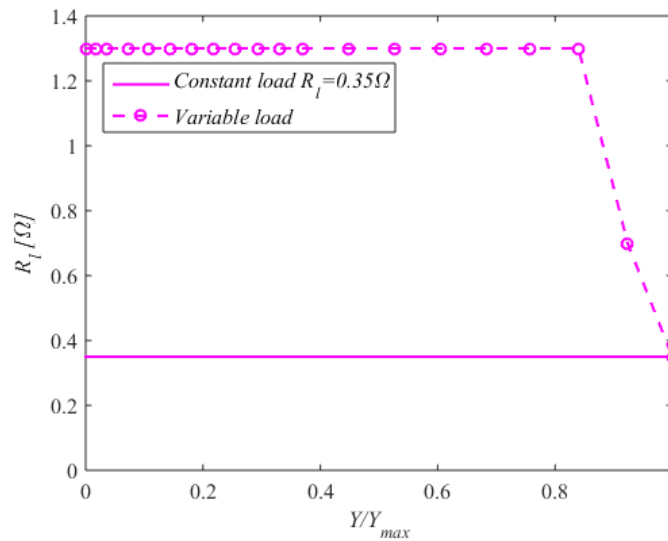


Figure 90: Shunt load as a function of the normalised input amplitude  $Y/Y_{max}$  at resonance - the magenta solid line is referred to the constant load, the magenta dash line is referred to the variable load – the load increases when the input reduces until the optimum load is achieved

The results predicted in Chapter 3 and Chapter 5 are qualitatively confirmed. If the input level reduces, the output voltage, in Figure 91, increases up to  $0.46V$ , which corresponds to the optimum. If the input level continues to reduce, the load is kept constant and the voltage decreases in a linear manner until the effect of friction becomes important around 0.3.

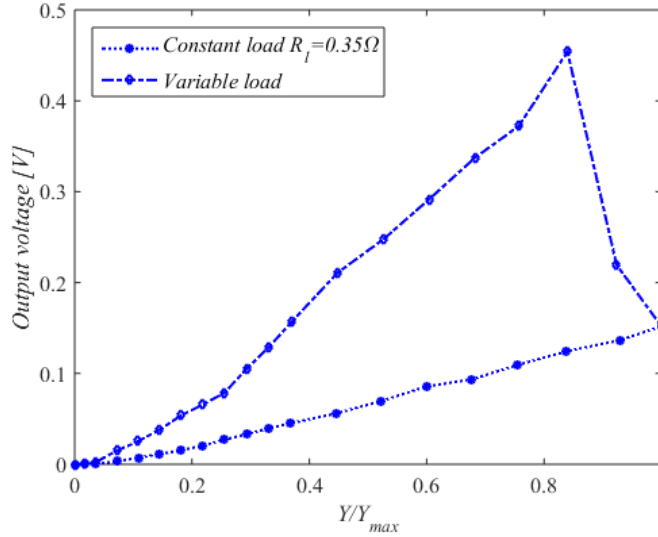


Figure 91: Level curves of the output voltage for a constant (dotted line), and a variable (dotted line) load as a function of the normalised input amplitude  $Y/Y_{max}$

The increment of the output voltage results in a larger amount of harvested power in the entire dynamic range, as confirmed experimentally in Figure 92. It can be seen that if the device has a physical constraint, the maximum power does not occur at the maximum input level. The maximum power achieved with a variable load is almost 2.5 times larger than the maximum power obtained adopting a constant load.

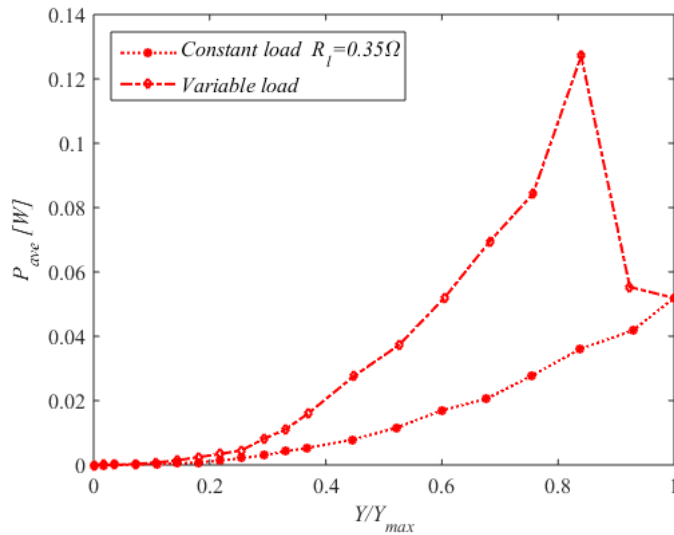


Figure 92: Level curves of average harvested power for a constant (dotted line), and a variable (dotted line) load as a function of the normalised input amplitude  $Y/Y_{max}$

It has been demonstrated experimentally that the proposed strategy can significantly improve the performance of an electromagnetic transducer energy harvesting device, for harmonic excitation. However, the procedure consisted of manually adjusting the value of the electric load according to the input. It is clear that in practice, energy harvesting devices should adapt autonomously themselves

to the environment using electromechanical solutions. The implementation of such a strategy is not part of this work, nevertheless, in the next Chapter 7, some solutions are discussed and explained as part of future work.

## 6.7 Summary

In this chapter, the experimental results carried out on the energy harvesting device were shown. Firstly, the mechanical behaviour of the energy harvester was observed; by exciting the device with random input at different input voltage level, a source of nonlinearity was detected. This nonlinearity was identified as parasitic friction its strength increased at low input. As predicted in Chapter 5, high level of friction could be expected when using mechanisms of conversion of motion such as gearbox.

The behaviour of the device was then analysed in operative conditions such as short circuit  $R_l=0$ , load circuit and open circuit  $R_l \rightarrow \infty$ . By varying the electric load, it was observed that the angular displacement and the output voltage increase and tend asymptotically to open circuit condition. Nevertheless, the average harvested power shows a maximum corresponding to an optimum load. As expected, the device behaves in a linear manner in almost the entire range of performance. The angular displacement and the output voltage grow linearly with the input displacement  $Y$ , while the harvested power depends on the square of the amplitude of displacement. The effect of friction is predominant at low input where a significant drop in the response and, consequently, in the output voltage and the harvested power can be seen.

The strategy to maximise the harvested power, explained in Chapter 3, covered the last part of the chapter. Making the load level-dependent, to operate at the maximum angular displacement, a significant improvement in both the output voltage and the harvested power in the entire dynamic range was observed. The numerical and analytical results presented in Chapter 3 and Chapter 5 were validated experimentally, which allow one to conclude that the proposed approach presents a valid and promising solution to improve the performance of such devices.

## Chapter 7: Conclusions and future work

### 7.1 Conclusions

This work has focused on improving the performance of an electromagnetic transducer energy harvesting devices. The device is assumed to be installed in an environment with a limited available volume, and consequently the size of the device is restricted. Therefore, the maximum relative displacement is a constraint imposed during the design process. Any type of electromagnetic energy harvester shows a peak/maximum in the power, which corresponds to an optimum electric load. The optimum power depends on the electrical characteristics of the generator and the mechanical damping. Nevertheless, tuning the energy harvester to operate at the optimum load can be in contrast with the constraint imposed. If the throw is limited and cannot exceed the available stroke, the harvester may not operate at the optimum condition since it cannot guarantee the constraint compliance. By deliberately introducing a source of nonlinearity in the electrical circuit, which is coupled to the mechanical side by means of a generator, the device can operate in its optimum condition. Both the linear and the nonlinear arrangements are compared so that under certain conditions (natural frequency and maximum input level) they have the same response and are complied with the imposed constraint. The nonlinearity in the damping can have different forms. A nonlinear resistance, in the form of cubic load and level-dependant load, was assumed such that voltage is no longer linearly proportional to the current. In addition, another source of unwanted nonlinearity was studied, namely the static friction, which is very common, especially in the gearbox and reciprocating mechanisms. The analytical formulation was derived for different sources of excitation such as harmonic and random, and the results were compared with those obtained from the numerical integration.

In Chapter 3, the effect of a cubic and a level-dependant load was studied for harmonically based-excited harvester. The device is modelled as a single-degree-of-freedom mechanical system, which is coupled with an ideal generator. Thus, the internal electrical dissipations due to the coil are not included.

A nonlinear load influences the responses of the device only at the natural frequency, as it introduces a nonlinearity in the damping force. The first strategy to increase the power was to use a cubic load, in which the current is proportional to the cube of the voltage across the resistor. The cubic damping is characterised by a higher response at resonance than a linear device, as the input excitation amplitude reduces. This causes the harvested power to improve, as the power is proportional to the square of the response. The second strategy consists of using a level-dependant load, which is able to adjust the damping as the input level varies. Using this strategy, the load is varied to make the harvester operates at the optimum conditions. The analytical and the numerical results demonstrate

that both the nonlinear arrangements can increase the harvested power when compared to a linear device.

In addition, the parasitic friction, in the form of Coulomb law, was introduced into the model. This is because typically, in mechanisms of conversion of motion, the effects of this dissipation cannot be neglected. Parasitic friction is effective at low velocity and, therefore, at low input levels where a sudden reduction of the performance of the device can be observed.

In Chapter 4, the behaviour of the device is studied for random inputs. In details, two input models such as Gaussian white noise and Gaussian band-limited, in the form of second-order filter, were used to excite the structure. For white input, the numerical integration was compared to the analytical solution obtained by using the equivalent linearisation method, whose main approximation relies on the assumption that the output of a nonlinear system is Gaussian. This assumption produces large errors when the system is highly nonlinear, and results in an underestimation of the variance (or in other words an overestimation of the damping). Also, it was demonstrated that the introduction of a cubic load does not improve the harvested power when compared to a linear load. The use of a second-order filter to model a band-limited excitation was justified by the fact that in some applications, such as sea waves, the input spectrum can be modelled using a second-order filter, at least at the early design stages. In addition, the input level changes with the wind velocity, which is a practical example of situation carried out in this thesis. The bandwidth of the filter was varied to simulate both narrow and broadband input excitation. It was shown that when the damping of the filter is smaller than the mechanical damping of the structure, the results are similar to the harmonic excitation, and the introduction of a cubic load is beneficial for the average harvested power in the entire dynamic range of performance. However, when the spectrum of the input signal is broader, no beneficial effect can be detected for the power, and the results are coherent with the results from white noise input. Also, for narrow input, the level-dependent strategy was implemented, providing a promising solution to increase the power when compared to a linear and a cubic load.

Chapter 5 presents the design of an electromagnetic transducer energy harvesting demonstrator, which is aimed to validate the second strategy (level-dependant load) proposed in Chapter 3. The mechanical system consists of an oscillating beam, sprung to the ground and coupled with a gearbox and a generator. Gearbox and generator were already available. An analytical parametrical analysis was adopted to find the mass and geometrical properties of the structure; an estimation of mechanical viscous damping was also conducted by measuring the free response of a beam attached to the gearbox and applying the logarithmic decrement. The design terminated with a 3D CAD model and 2D drawings, which allowed the manufacturer to build the structure.

In Chapter 6, the experiments conducted on the manufactured structure are presented. A first preliminary test on the mechanical structure put in evidence the presence of a nonlinearity, which takes place at low input level and affects the response at the natural frequency. This phenomenon is

due to the parasitic friction in the gearbox. The response of the device is obtained in three different operating conditions such as open circuit (no electric load across the terminals), short circuit (direct connection between the terminals) and load circuit. However, only load circuit allows the harvesting process. The electric load is then passively adjusted according to the input level to implement the level-dependent load, proposed in Chapter 3. The effect of a level-dependent load was compared to a constant load in terms of the output response and the power harvested. The experiments were in good agreement with the simulation presented in Chapter 3 and Chapter 5, and the results demonstrated that a level-dependant load could improve the performance of an energy harvesting device in the entire dynamic range.

## 7.2 Suggestions for future works

The research work presented here could be followed by exploiting a number of potential aspects, from both the numerical and experimental point of view, which are listed and discussed below.

### 7.2.1 Modelling

- Include the effect of inductance and capacitance: the work presented in Chapter 3 could proceed by modelling a more complete electrical circuit. The effect of an inductance and a capacitance on the electrical circuitry would be different from a resistor, which is demonstrated to affect the damping force only. In applications where the frequency of the excitation changes, having an inductance and a capacitance may help to track the excitation frequency by modifying the resonance of the device. In electromagnetic applications where the frequency is relatively low, the effect of inductance is not significant compared to the capacitance. In addition, from the experimental results, it was shown that the effect of the internal resistance of the generator is not negligible. In real applications, the internal resistance grows proportionally to the size of the generator, therefore, depending on the situation, it may have an important influence on the results. Consequently, a more complete model of the electromagnetic energy harvester is required including inductance, capacitance and internal resistance;
- Extend the analytical formulation to nonlinear harvester driven by random input: in Chapter 4, a random input was considered as a type of excitation. Nevertheless, only for white noise excitation, we were able to derive a close-form solution for the harvested power using a linearization method. Although this method is useful to predict the second-order statistics of a nonlinear system, it does not estimate the PDF, which is an important quantity for statistical information about the system states. It was shown that there are other methods such as the equivalent non-linearisation method, which allows one to obtain a good estimation of the PDF. Unfortunately this method only works for white noise input. A useful tool, which has become popular in structural dynamics in the last decades, is called Wiener series, which is



originates from the well-known Volterra series. Using the Wiener series, a close-form solution of the second-order and higher statistics can be obtained, for nonlinear systems driven by coloured noise. Due to the high computational time and the numerical errors caused by numerical integration, this aspect can be fundamental and included as part of future work;

### 7.2.2 Experiments

- Synthesising a nonlinear load: in Chapter 3, it was demonstrated that a cubic and a level-dependant load can improve the harvested power compared to linear devices, in the entire dynamics range. Furthermore, in Chapter 6, the effectiveness of a level-dependant load was demonstrated also experimentally. Nevertheless, the load was adjusted manually, which is obviously not the kind of strategy that a real prototype can rely on. Therefore, as part of future work, the next step could be to automatize the two proposed strategies. This can be done electronically for both the cubic and the level-dependant load by designing a circuit in which the current generated by the generator is fed into a block scheme (made with DSpace), where a nonlinear digital function can be implemented;
- Prototyping an energy harvesting device: as pointed out in this thesis work, the device, which has been built, is not a prototype, which means that it was not thought to operate in a real environment. Its main goal was to demonstrate specific properties of nonlinear systems, which can be an advantage for the energy harvesting. The application of reference is the sea waves, which present a narrow frequency bandwidth with variable input levels of the excitation. This characteristics of the spectrum makes the nonlinear load more effective than a linear one. The next step is to design a prototype for a specific environment. If the environment is the sea, then a device, which resonates within the frequency bandwidth of the excitation ( $0.15\text{--}0.4\text{Hz}$ ) has to be designed. The input has to be measured and used during the design process to optimise the parameters of the harvester such that the device operates at the optimal conditions;
- Model of gearbox: in Chapter 5, the design of the device was made assuming that the gearbox is not affecting the dynamics of the harvester. Its effect was only to increase a gain  $G$  (gear ratio) and the output voltage. However, during the experiments shown in Chapter 6, the dynamics were influenced by the gearbox, which is not designed to operate at the operating conditions for the conducted tests. For this reason, the correlation between numerical and experimental results was not performed but can be considered as part of future work;

## Publications

Parts of this work have been published as [49,73,77–79]:

- Maryam Ghandchi Tehrani, Luigi Simeone, Stephen Elliott, *Energy Harvesting using Nonlinear Damping*, ENOC Conference, Wien, 2014.
- L. Simeone, M.G. Tehrani, S.J. Elliott, *Nonlinear Damping in an Energy Harvesting Device*, ISMA Conference, Leuven, 2014.
- P.L. Green, M. Hendijanizadeh, L. Simeone, S.J. Elliott, *Probabilistic Modelling of a Energy Harvester*, Journal of Intelligent Material Systems and Structures, Accepted on 22<sup>nd</sup> January 2015.
- L. Simeone, M.G. Tehrani, S.J. Elliott, *Design of an electromagnetic-transducer energy Harvester*, RASD Conference, Southampton, 2016.
- L. Simeone, M.G. Tehrani, S.J. Elliott, *Maximisation of the harvested power via variable shunt load in a constrained energy harvesting device*, ISMA Conference, Leuven, 2016.

A journal paper is being prepared entitled “*Level-dependent load on a pendulum like energy harvester*”.

## Appendix I – Variance of linear systems (Lyapunov equation)

For stationary random processes, the covariance matrix  $C$  does not vary with time:

$$\dot{C} = 0 \quad (I.1)$$

, and consequently, the Lyapunov equation assumes the following form:

$$AC + CA^T = -GG^T \quad (I.2)$$

, where  $A$  is the state matrix,  $G$  is the column vector of the random input, and  $C$  is the covariance matrix which is a 2x2 matrix in which has the variance of the displacement and velocity on the diagonal and the cross correlations out of the diagonal. If we consider a single-degree-of-freedom system with mass  $m$ , stiffness  $k$  and damping  $c$ , equation 6.9 becomes:

$$\begin{bmatrix} 0 & 1 \\ -k/m & -c/m \end{bmatrix} \begin{bmatrix} \sigma_z^2 & R_{z\dot{z}}(0) \\ R_{\dot{z}z}(0) & \sigma_{\dot{z}}^2 \end{bmatrix} + \begin{bmatrix} \sigma_z^2 & R_{z\dot{z}}(0) \\ R_{\dot{z}z}(0) & \sigma_{\dot{z}}^2 \end{bmatrix} \begin{bmatrix} 0 & -k/m \\ 1 & -c/m \end{bmatrix} = \begin{bmatrix} 0 & 0 \\ 0 & -S_w \end{bmatrix} \quad (I.3)$$

Since the system is linear the state variable are uncorrelated, consequently the cross correlations out of the diagonal are zero. The variance of displacement is found to be:

$$\sigma_z^2 = \frac{mS_w}{2c\omega_n^2} \quad (I.4)$$

, and the variance of velocity is:

$$\sigma_{\dot{z}}^2 = \frac{mS_w}{2c} \quad (I.5)$$

## Appendix II – Gaussian integral

The following integral is called Gaussian integral:

$$\int_{-\infty}^{+\infty} e^{-x^2} dx = \sqrt{\pi} \quad (\text{II.1})$$

Since the Gaussian function is an even function, it holds:

$$\int_0^{+\infty} e^{-x^2} dx = \frac{\sqrt{\pi}}{2} \quad (\text{II.2})$$

It also holds:

$$\int_{-\infty}^{+\infty} e^{-\alpha x^2} dx = \frac{\sqrt{\pi}}{\sqrt{\alpha}} \quad (\text{II.3})$$

It is easy to compute the Gaussian-type integral, by computing the derivative of both the sides with respect to alpha as follows:

$$\int_{-\infty}^{+\infty} x^2 e^{-\alpha x^2} dx = -\frac{d}{d\alpha} \left( \frac{\sqrt{\pi}}{\sqrt{\alpha}} \right) = \frac{\sqrt{\pi}}{2\sqrt{\alpha^3}} \quad (\text{II.4})$$

And,

$$\int_{-\infty}^{+\infty} x^4 e^{-\alpha x^2} dx = \frac{d^2}{d\alpha^2} \left( \frac{\sqrt{\pi}}{\sqrt{\alpha}} \right) = \frac{3\sqrt{\pi}}{4\sqrt{\alpha^5}} \quad (\text{II.5})$$

In this case  $x = \mathfrak{X}$  and  $\alpha = 1/2\sigma_{\mathfrak{X}}^2$ , the integral to compute is:

$$E[\mathfrak{X}^4] = 3\sigma_{\mathfrak{X}eq}^4 \quad (\text{II.6})$$

### Appendix III – Equivalent non-linearisation

The method, consists in replacing, the nonlinear term (and for which a solution cannot be found) with another nonlinear function, which belongs to the class of generalised stationary potential, which is the broadest solvable class known to date, and includes a large class of linear and nonlinear systems [80]. The replacing function, used to approximate the nonlinearity, is equivalent to the replaced function in statistical sense. The solution, which is obtained, will be exact for the replacing system, but only approximate for the replaced system. The following equation of motion is hereafter considered:

$$m\ddot{z} + c_3 \dot{z}^3 + kz = m\ddot{z}(t), \quad (\text{III.1})$$

This equation can be replaced by the following equation where the cubic damping is substituted by another term,

$$m\ddot{z} + c_{eq}(H)\dot{z} + kz = m\ddot{z}(t) \quad (\text{III.2})$$

, where  $H$  represents the total conservative mechanical energy per unit of mass of the system (kinetic plus potential energy), and it can be defined as:

$$H = \frac{1}{2} \dot{z}^2 + \frac{1}{2} \omega_n^2 z^2 \quad (\text{III.3})$$

The method is based on the assumption that the total energy is conservative and constant. For such a class of systems, the joint probability density function can be computed as

$$p(z, \dot{z}) = A_0 e^{-\frac{2}{\pi m S_0} \int_0^H f(\eta) d\eta} H_y \quad (\text{III.4})$$

, where the function  $f(H)$  corresponds, in our case, to the equivalent damping coefficient  $c_{eq}(H)$ .

The equivalent damping function  $c_{eq}(h)$  is computed by considering the energy dissipation rate, averaged over time, where  $h$  is the conservative mechanical energy per unit of mass in one period.

$$c_{eq}(h) = \frac{E[c_3 \dot{z}^3 | h]}{E[\dot{z}^2 | h]} \quad (\text{III.5})$$

, where  $E[\cdot | h]$  is the conditional mean value, and represents the mean value, at the specific energy level  $h$ . The expectation (or mean value) has then to be evaluated for a specific value of the parameter  $h$ .

$$c_{eq}(h) = \frac{\frac{1}{2\pi} \int_0^{2\pi} (c_3 \mathfrak{E}^3 |h|)}{\frac{1}{2\pi} \int_0^{2\pi} (\mathfrak{E}^3 |h|)} = \frac{3}{2} c_3 h \quad (\text{III.6})$$

It is interesting to see, at this stage, which is the difference between the equivalent viscous damping, computed by this method, and the one estimated by the equivalent linearisation. In the following,  $c_{eq}$  is plotted as a function of the input excitation  $S_0$  for both the methods.

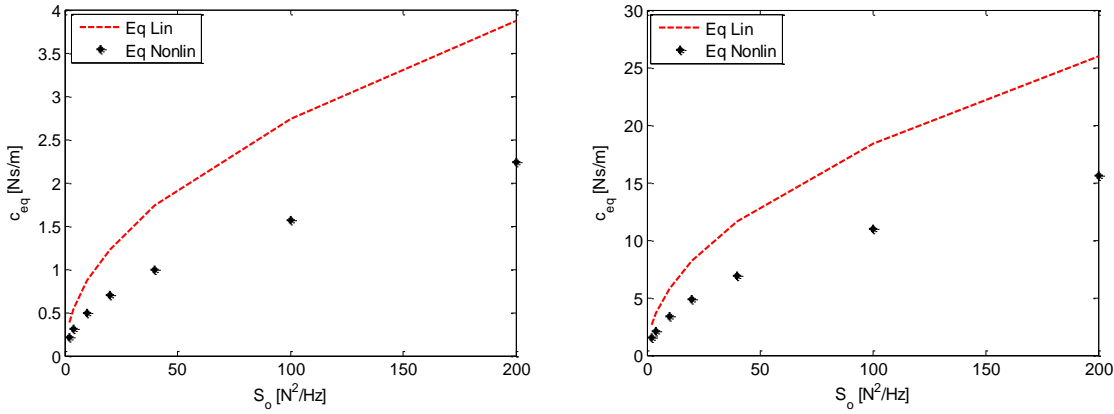


Figure III.1: Equivalent damping as a function of input level.  $c_3$  equal to: (left)  $0.1 \text{ Ns}^3/\text{m}^3$ , (right)  $4.5 \text{ Ns}^3/\text{m}^3$ ,  $c_{1eq} = 1.55 \text{ Ns/m}$

As shown in Figure , the estimation of the equivalent damping is different for the two methods.

The equivalent linearisation seems to overestimate the damping with respect to the equivalent non-linearisation. This is will be also confirmed when the spectrum of the power harvested will be calculated, in the next section. It is to expect that, as the equivalent linearisation overestimates the damping, the peak of the power, at resonance, will be lower than the equivalent nonlinearisation. It is also evident how the difference between these two methods gets lower as the input excitation decreases. In fact, the two approaches yield the same results, in terms of power spectrum of the output because the effect of the cubic nonlinearity is negligible at low level of excitation.

According to equation, the stationary joint *PDF* can be computed as:

$$p(z, \mathfrak{E}) = A_0 e^{-\frac{3c_3}{2\pi S} \left( \frac{1}{2} \mathfrak{E}^2 + \frac{1}{2} \omega_n^2 z^2 \right)^2} \quad (\text{III.7})$$

From equation III.7, it can be noticed that the state variable are statistically dependent and the distribution is not Gaussian. In Figure III.2, the equivalent non-linearisation (central) is in very good agreement with the cubic damping (left). The equivalent linearisation (right) fails to estimate the *PDF* because it assumes it Gaussian.

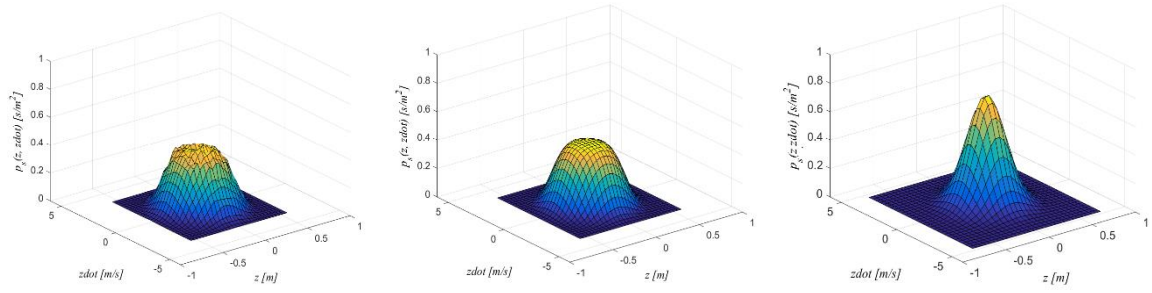


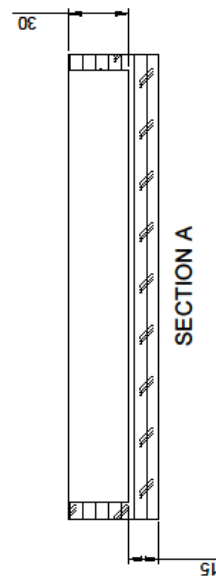
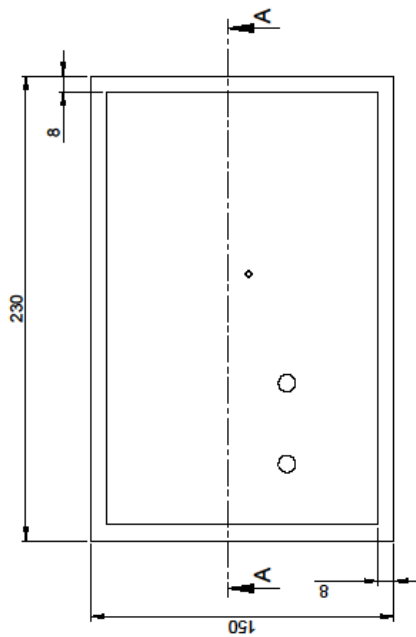
Figure III.2: Joint probability density functions. Numerical (left), equivalent non-linearisation (central), equivalent linearisation (right), for  $c_3=4.5Ns^3/m^3$  and  $S_w=100(m/s^2)^2/Hz$ ,  $c_{1eq}=1.55Ns/m$

The variance is also estimated and listed in Table III.1.

Joint Variance	Numerical	Equivalent nonlinear	Equivalent linear
$\sigma_z^2 [m^2]$	0.0428	0.0389	0.0345
$\sigma_{\dot{z}}^2 [m^2/s^2]$	1.58	1.54	1.36

As shown in Figure III.1, the equivalent linearization overestimates the variance. From Table III.1 the equivalent non-linearisation is closer to the numerical solution also in terms of variance.

# Appendix III – Drawings

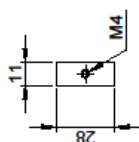
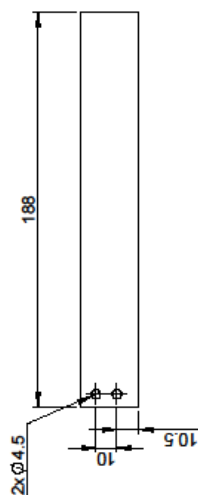


SECTION A

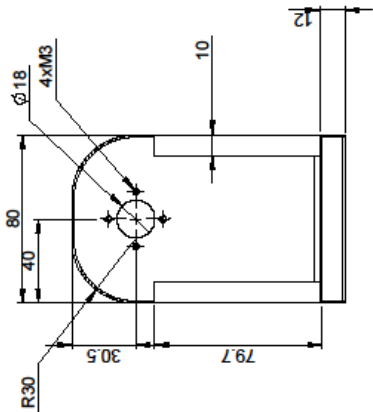
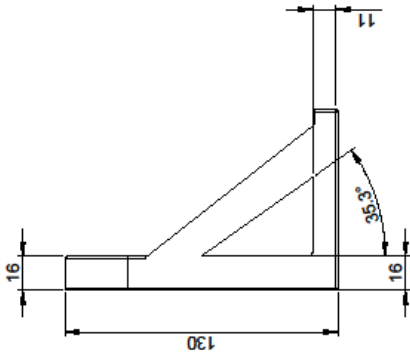
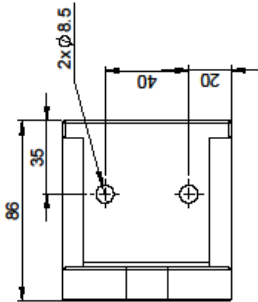
SOLIDWORKS Educational Product. For Instructional Use Only

DO NOT SCALE		DRAWN BY XXXX		UNIVERSITY OF <b>Southampton</b> Faculty of Engineering and the Environment	
A3	ISIRI	DESIGNED BY XXXX	DATE	TITLE	
PROJECT XXXX	SUPERVISOR XXXX	MATERIAL XXXX	SCALE 2:1	Base	
REMOVE ALL SHARP EDGES		THE INFORMATION CONTAINED IN THIS DOCUMENT IS THE PROPERTY OF THE UNIVERSITY OF SOUTHAMPTON		SHEET 1 of 1	
P IN COURTESY FRAME AMR		REVISION		A	




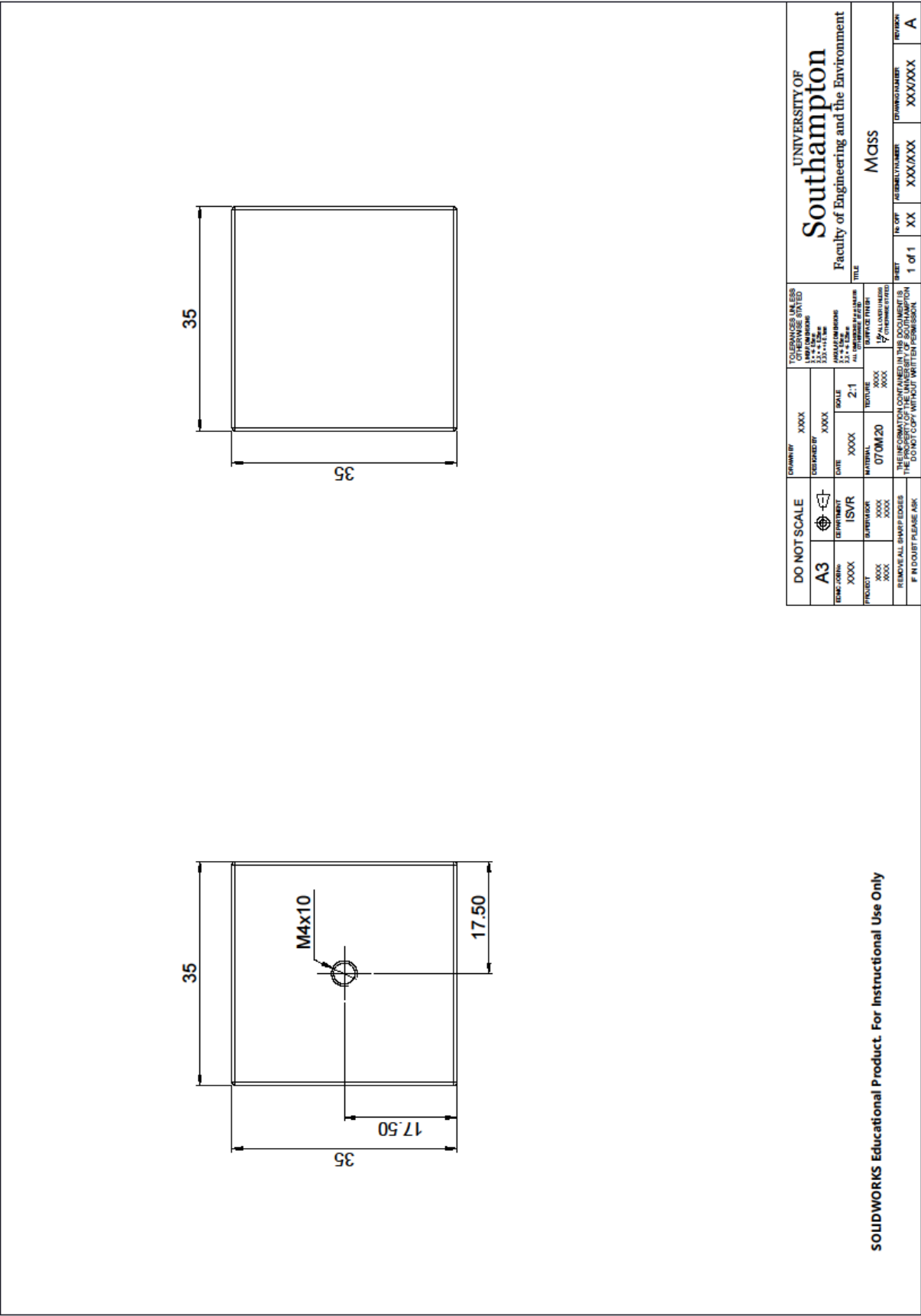
[illegible]

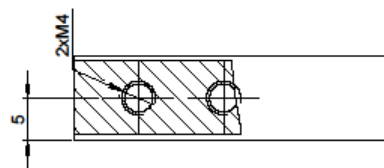
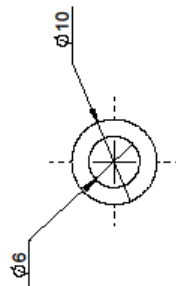
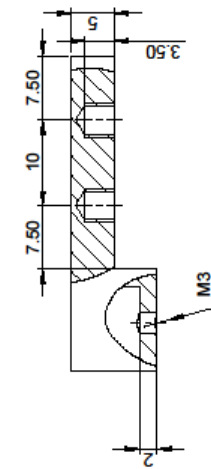
**SOLIDWORKS Educational Product. For Instructional Use Only**



SOLIDWORKS Educational Product. For Instructional Use Only

DO NOT SCALE		DRAWN BY		TOLERANCES UNLESS OTHERWISE STATED FRACTIONS DECIMALS 1:1 = 12.5mm 1:1 = 12.5mm 2:1 = 25mm 2:1 = 25mm 3:1 = 37.5mm 3:1 = 37.5mm		UNIVERSITY OF Southampton Faculty of Engineering and the Environment	
A3		DATE	SCALE	DATE	SCALE	FILE Flange	
XXXX	ISVR	XXXX	2:1	XXXX	XXXX		
XXXX	XXXX	XXXX	XXXX	XXXX	XXXX		
XXXX	XXXX	XXXX	XXXX	XXXX	XXXX		
REMOVE ALL SHARP EDGES IF IN DOUBT PLEASE ASK		THE INFORMATION CONTAINED IN THIS DOCUMENT IS THE PROPERTY OF THE UNIVERSITY OF SOUTHAMPTON DO NOT COPY WITHOUT WRITTEN PERMISSION		SHEET 1 of 1		REVISION A	



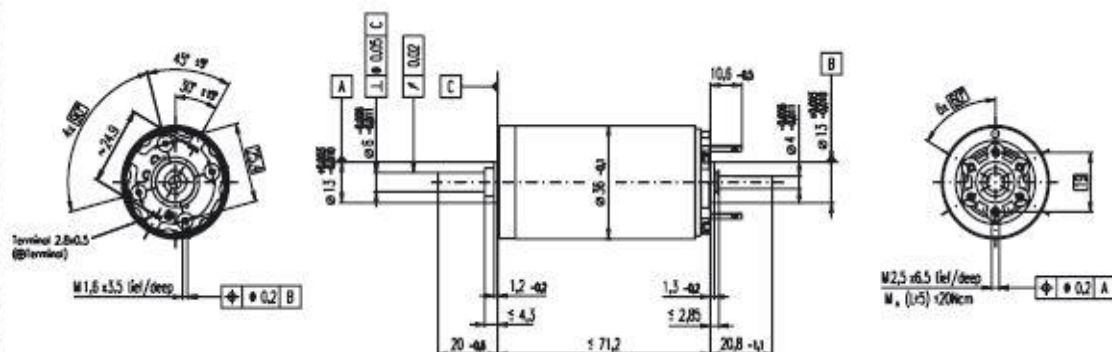


DO NOT SCALE		DRAWN BY	XXXX	TOLERANCES UNLESS OTHERWISE STATED	
A3	ISIRI	DATE	XXXX	UNLESS OTHERWISE STATED	UNLESS OTHERWISE STATED
XXXX	XXXX	SCALE	2:1	3.2 ± 0.1 mm	3.2 ± 0.1 mm
XXXX	XXXX	MATERIAL	Wood	6.3 ± 0.2 mm	6.3 ± 0.2 mm
XXXX	XXXX	TEXTURE	XXXX	12.5 ± 0.5 mm	12.5 ± 0.5 mm
XXXX	XXXX	FINISH	XXXX	25.0 ± 1.0 mm	25.0 ± 1.0 mm
REMOVE ALL SHARP EDGES	REMOVE ALL SHARP EDGES	FINISH	XXXX	50.0 ± 1.5 mm	50.0 ± 1.5 mm
IF IN DOUBT PLEASE ASK	IF IN DOUBT PLEASE ASK	FINISH	XXXX	100.0 ± 2.0 mm	100.0 ± 2.0 mm
SOLIDWORKS Educational Product. For Instructional Use Only		UNIVERSITY OF Southampton		Faculty of Engineering and the Environment	
		TITLE		Support	
		SHEET		1 of 1	
		IN QTY		XX	
		ASSEMBLY NUMBER		XXXXXX	
		DRAWING NUMBER		XXXXXX	
		REVISION		A	

# Appendix IV – Generator and gearbox

## RE 36 Ø36 mm, Graphite Brushes, 70 Watt

maxon DC motor



M 1:2

- Stock program
- Standard program
- Special program (on request!)

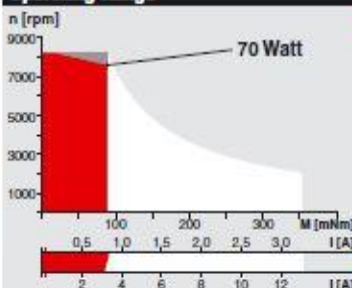
### Order Number

Motor Data		118797	118798	118799	118800	118801	118802	118803	118804	118805	118806	118807	118808	118809	118810
1 Assigned power rating	W	70	70	70	70	70	70	70	70	70	70	70	70	70	70
2 Nominal voltage	Volt	18.0	24.0	32.0	42.0	42.0	48.0	48.0	48.0	48.0	48.0	48.0	48.0	48.0	48.0
3 No load speed	rpm	6610	6210	6790	7020	6340	6420	5220	4320	3450	2830	2290	1780	1420	1180
4 Stall torque	mNm	730	783	832	865	786	785	627	504	403	326	258	198	158	127
5 Speed / torque gradient	rpm / mNm	9.23	8.05	8.27	8.19	8.14	8.25	8.41	8.65	8.67	8.90	8.96	9.17	9.21	9.51
6 No load current	mA	153	105	89	70	61	55	42	33	25	20	15	12	9	7
7 Starting current	A	28.6	21.5	18.7	15.3	12.6	11.1	7.22	4.80	3.06	2.04	1.30	0.784	0.501	0.334
8 Terminal resistance	Ohm	0.628	1.11	1.71	2.75	3.35	4.32	6.65	10.00	15.7	23.5	36.8	61.3	95.8	144
9 Max. permissible speed	rpm	8200	8200	8200	8200	8200	8200	8200	8200	8200	8200	8200	8200	8200	8200
10 Max. continuous current	A	3.18	2.44	1.99	1.59	1.44	1.27	1.03	0.847	0.679	0.556	0.445	0.346	0.277	0.226
11 Max. continuous torque	mNm	81	88.8	88.5	89.8	90.4	90.1	89.8	89.0	89.2	88.8	88.1	87.3	87.2	85.8
12 Max. power output at nominal voltage	W	123	125	146	157	129	131	84.9	56.4	36.0	23.9	15.2	9.09	5.78	3.82
13 Max. efficiency	%	84	85	86	86	86	86	84	82	81	79	77	75	72	72
14 Torque constant	mNm / A	25.5	36.4	44.5	56.6	62.6	70.7	86.9	105	131	160	198	253	315	380
15 Speed constant	rpm / V	375	263	215	169	152	135	110	90.9	72.7	59.8	48.2	37.8	30.3	25.1
16 Mechanical time constant	ms	6	6	6	6	6	6	6	6	6	6	6	6	6	6
17 Rotor inertia	gcm <sup>2</sup>	60.2	67.7	65.2	65.4	65.6	64.6	63.3	61.5	61.3	60.3	59.2	57.8	57.5	55.7
18 Terminal inductance	mH	0.10	0.20	0.30	0.49	0.60	0.76	1.15	1.68	2.62	3.87	5.96	9.70	15.10	21.90
19 Thermal resistance housing-ambient	K / W	6.4	6.4	6.4	6.4	6.4	6.4	6.4	6.4	6.4	6.4	6.4	6.4	6.4	6.4
20 Thermal resistance rotor-housing	K / W	3.4	3.4	3.4	3.4	3.4	3.4	3.4	3.4	3.4	3.4	3.4	3.4	3.4	3.4
21 Thermal time constant winding	s	38	43	41	41	41	41	40	39	39	38	37	36	36	35

### Specifications

- Axial play 0.05 - 0.15 mm
- Max. ball bearing loads
  - axial (dynamic) 5.6 N
  - not preloaded 2.4 N
  - radial (5 mm from flange) 28 N
  - Force for press fits (static) (static, shaft supported) 110 N
  - 1200 N
- Radial play ball bearing 0.025 mm
- Ambient temperature range -20 ... +100°C
- Max. rotor temperature +125°C
- Number of commutator segments 13
- Weight of motor 350 g
- 2 pole permanent magnet
- Values listed in the table are nominal. For applicable tolerances see page 43. For additional details please use the maxon selection program on the enclosed CD-ROM.
- ⚠ Tolerances may vary from the standard specification.

### Operating Range



### Comments

- Recommended operating range
- Continuous operation  
In observation of above listed thermal resistances (lines 19 and 20) the maximum permissible rotor temperature will be reached during continuous operation at 25°C ambient.  
= Thermal limit.
- Short term operation  
The motor may be briefly overloaded (recurring).
- 118804 Motor with high resistance winding
- 118797 Motor with low resistance winding

### maxon Modular System

**Planetary Gearhead**  
Ø32 mm  
0.75 - 4.5 Nm  
Details page 219

**Planetary Gearhead**  
Ø32 mm  
1.0 - 6.0 Nm  
Details page 220

**Planetary Gearhead**  
Ø32 mm  
0.4 - 2.0 Nm  
Details page 222

**Planetary Gearhead**  
Ø42 mm  
3 - 15 Nm  
Details page 224

Recommended Electronics:  
ADS 50/5 page 259  
ADS 50/10 page 259  
ADS E 50/5, 50/10 page 260  
EPOS 24/5 page 271  
MIP 50 page 273  
Notes page 17

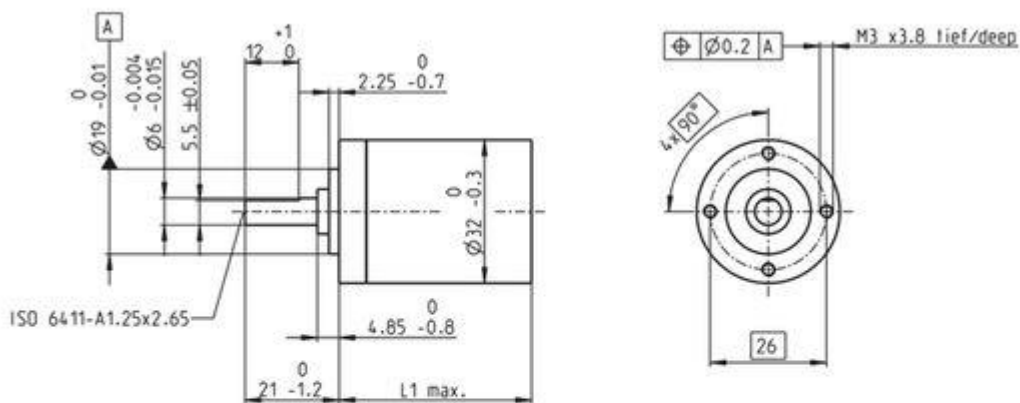
**Encoder MR**  
256 - 1024 CPT,  
3 channels  
Details page 239

**Encoder HEDS 5540**  
500 CPT,  
3 channels  
Details page 242

**Encoder HEDL 5540**  
500 CPT,  
3 channels  
Details page 244

**DC-Tacho DCT**  
Ø22 mm  
0.52 V  
Details page 252

## Technical illustrations



Dimension drawing

Information: Drawings are not to scale.

## General information

Gearhead type	GP
Outer diameter	32 mm
Version	A

## Gearhead Data

Reduction	18 : 1
Absolute reduction	624/35
Max. motor shaft diameter	4 mm
Number of stages	2
Max. continuous torque	2.25 Nm
Max. intermittent torque	3.4 Nm
Direction of rotation, drive to output	=
Max. efficiency	75 %
Average backlash no load	0.8 °
Mass inertia	0.8 gcm <sup>2</sup>
Gearhead length (L1)	36.3 mm
Max. transmittable power (continuous)	79 W
Max. transmittable power (intermittent)	120 W

## Technical Data

Radial play	max. 0.14 mm, 5 mm from flange
Axial play	max. 0.4 mm
Max. radial load	140 N, 12 mm from flange
Max. axial load (dynamic)	120 N
Max. force for press fits	120 N
Max. continuous input speed	6000 rpm
Max. intermittent input speed	6000 rpm
Recommended temperature range	-20...+100 °C
Extended temperature range	-35...+100 °C
Number of autoclave cycles	0

## Product

Weight	160 g
--------	-------

## List of References

- [1] S. Tornincasa, M. Repetto, E. Bonisoli, F. Di Monaco, Optimization of magneto-mechanical energy scavenger for automotive tire, *J. Intell. Mater. Syst. Struct.* 0 (2011) 1–10. doi:10.1177/1045389X11430741.
- [2] S. Tornincasa, M. Repetto, E. Bonisoli, F. Di Monaco, Energy harvester for vehicle tires: Nonlinear dynamics and experimental outcomes, *J. Intell. Mater. Syst. Struct.* 23 (2012) 3–13. doi:10.1177/1045389X11430739.
- [3] Y.M. Chen, Y.J. Peng, Thermal energy harvesting aware routing for wireless body area network in medical healthcare system, *Appl. Mech. Mater.* 394 (2013) 482–486. doi:10.4028/www.scientific.net/AMM.394.482.
- [4] a Kansal, M.B. Srivastava, An environmental energy harvesting framework for sensor networks, *Low Power Electron. Des.* 2003. ISLPED '03. Proc. 2003 Int. Symp. (2003) 481–486. doi:10.1109/LPE.2003.1231958.
- [5] S.P. Beeby, R.N. Torah, M.J. Tudor, P. Glynn-Jones, T. O'Donnell, C.R. Saha, S. Roy, A micro electromagnetic generator for vibration energy harvesting, *J. Micromechanics Microengineering*. 17 (2007) 1257–1265. doi:10.1088/0960-1317/17/7/007.
- [6] S.P. Beeby, M.J. Tudor, N.M. White, Energy harvesting vibration sources for microsystems applications, *Meas. Sci. Technol.* 17 (2006) R175. doi:10.1088/0957-0233/17/12/R01.
- [7] R.L. Harne, Concurrent attenuation of, and energy harvesting from, surface vibrations: experimental verification and model validation, *Smart Mater. Struct.* 21 (2012) 35016. doi:10.1088/0964-1726/21/3/035016.
- [8] S. Roundy, P.K. Wright, J. Rabaey, A study of low level vibrations as a power source for wireless sensor nodes, *Comput. Commun.* 26 (2003) 1131–1144. doi:10.1016/S0140-3664(02)00248-7.
- [9] H.S. Rauschenbach, *Solar Cell Array Design Handbook*, First, Springer Netherlands, Dordrecht, (1980). doi:10.1007/978-94-011-7915-7.
- [10] J.B. Lee, Z. Chen, M.G. Allen, A. Rohatgi, R. Arya, Miniaturized high-voltage solar cell array as an electrostatic MEMS power supply, *J. Microelectromechanical Syst.* 4 (1995) 102–108. doi:10.1109/84.465125.
- [11] M. Stordeur, I. Stark, Low Power Thermoelectric Generator - self-sufficient energy supply

- for micro systems, 16th Int. Conf. Thermoelectr. (1997) 575–577.
- [12] M. Umeda, K. Nakamura, S. Ueha, Energy Storage Characteristics of a Piezo- Generator using Impact Induced Vibration, *Jpn. J. Appl. Phys.* 36 (1997) 3146–3151.
  - [13] a Erturk, D.J. Inman, An experimentally validated bimorph cantilever model for piezoelectric energy harvesting from base excitations, *Smart Mater. Struct.* 18 (2009) 25009. doi:10.1088/0964-1726/18/2/025009.
  - [14] F. Goldschmidtboeing, P. Woias, Characterization of different beam shapes for piezoelectric energy harvesting, *J. Micromechanics Microengineering.* 18 (2008) 104013. doi:10.1088/0960-1317/18/10/104013.
  - [15] T. Sterken, P. Fiorini, K. Baert, G. Borghs, R. Puers, Novel design and fabrication of a MEMS electrostatic vibration scavenger, *PowerMEMS 2004.* (2004) 18–21.
  - [16] E.O. Torres, G. a. Rincón-Mora, Electrostatic energy-harvesting and battery-charging CMOS system prototype, *IEEE Trans. Circuits Syst. I Regul. Pap.* 56 (2009) 1938–1948. doi:10.1109/TCSI.2008.2011578.
  - [17] X. Tang, L. Zuo, Simulation and Experiment Validation of Simultaneous Vibration Control and Energy Harvesting from Buildings Using Tuned Mass Dampers, *Am. Control Conf.* 11794 (2011) 3134–3139.
  - [18] A. Gupta, J. a. Jendrzeczyk, T.M. Mulcahy, J.R. Hull, Design of electromagnetic shock absorbers, *Int. J. Mech. Mater. Des.* 3 (2006) 285–291. doi:10.1007/s10999-007-9031-5.
  - [19] J. Falnes, A review of wave-energy extraction, *Mar. Struct.* 20 (2007) 185–201. doi:10.1016/j.marstruc.2007.09.001.
  - [20] C.B. Williams, R.B. Yates, Analysis Of A Micro-electric Generator For Microsystems, 1995. doi:10.1109/SENSOR.1995.717207.
  - [21] N.G. Stephen, On energy harvesting from ambient vibration, *J. Sound Vib.* 293 (2006) 409–425. doi:10.1016/j.jsv.2005.10.003.
  - [22] P.L. Green, Nonlinear energy harvesting, University of Sheffield, PhD thesis, (2012).
  - [23] M. Hendijanzadeh, Design and optimisation of constrained electromagnetic energy harvesting devices, University of Southampton, PhD thesis, (2014).
  - [24] M. Hendijanizadeh, M. Moshrefi-Torbati, S.M. Sharkh, Constrained Design Optimization of Vibration Energy Harvesting Devices, *J. Vib. Acoust.* 136 (2013) 21001. doi:10.1115/1.4025877.



- [25] M. Zilletti, Self-tuning vibration absorbers, University of Southampton, PhD thesis, (2011).
- [26] M. Hendijanizadeh, S.M. Sharkh, S.J. Elliott, M. Moshrefi-Torbati, Output power and efficiency of electromagnetic energy harvesting systems with constrained range of motion, *Smart Mater. Struct.* 22 (2013) 125009. doi:10.1088/0964-1726/22/12/125009.
- [27] P.I. Ro, W. Shim, S. Jeong, Robust friction compensation for submicrometer positioning and tracking for a ball-screw-driven slide system, *Precis. Eng.* 24 (2000) 160–173. doi:10.1016/S0141-6359(00)00030-1.
- [28] Franz-Josef Elmer, *Nonlinear Dynamics*, website, (1998).
- [29] M. Cattani, I.L. Caldas, S.L. de Souza, K.C. Iarosz, Deterministic Chaos Theory: Basic Concepts, *Rev. Bras. Ensino Física.* 39 (2016). doi:10.1590/1806-9126-RBEF-2016-0185.
- [30] J. Guckenheimer and Ph. Holmes, *Nonlinear Oscillations, Dynamical Systems, and Bifurcations of Vector Fields*, (1983).
- [31] S.H. Strogatz, *Nonlinear Dynamics and Chaos*, (1994).
- [32] M. Umeda, K. Nakamura, S. Ueha, Analysis of the Transformation of Mechanical Impact Energy to Electric Energy Using Piezoelectric Vibrator, *Jpn. J. Appl. Phys.* 35 (1996) 3267–3273. doi:10.1143/JJAP.35.3267.
- [33] L. Gu, C. Livermore, Impact-driven, frequency up-converting coupled vibration energy harvesting device for low frequency operation, *Smart Mater. Struct.* 20 (2011) 45004. doi:10.1088/0964-1726/20/4/045004.
- [34] B.P. Mann, N.D. Sims, Energy harvesting from the nonlinear oscillations of magnetic levitation, *J. Sound Vib.* 319 (2009) 515–530. doi:10.1016/j.jsv.2008.06.011.
- [35] M.F. Daqaq, Response of uni-modal duffing-type harvesters to random forced excitations, *J. Sound Vib.* 329 (2010) 3621–3631. doi:10.1016/j.jsv.2010.04.002.
- [36] R.L.H. and K.W. Wang, A review of the recent research on vibration energy harvesting via bistable systems, *Smart Mater. Struct.* 22 (2013) 23001. doi:10.1088/0964-1726/22/2/023001.
- [37] R. Masana, M.F. Daqaq, Relative performance of a vibratory energy harvester in mono- and bi-stable potentials, *J. Sound Vib.* 330 (2011) 6036–6052. doi:10.1016/j.jsv.2011.07.031.
- [38] B. Zaghari, E. Rustighi, M. Ghandchi-tehrani, MOVIC2014 Experimental study on harvesting energy from a parametrically excited system, (2014) 1–13.
- [39] M. Ghandchi Tehrani, S.J. Elliott, Extending the dynamic range of an energy harvester

- using nonlinear damping, *J. Sound Vib.* 333 (2014) 623–629.  
doi:10.1016/j.jsv.2013.09.035.
- [40] F. Di Monaco, M. Ghandchi Tehrani, S.J. Elliott, E. Bonisoli, S. Tornincasa, Energy harvesting using semi-active control, *J. Sound Vib.* 332 (2013) 6033–6043.  
doi:10.1016/j.jsv.2013.06.005.
- [41] R.S. Langley, A general mass law for broadband energy harvesting, *J. Sound Vib.* 333 (2014) 927–936. doi:10.1016/j.jsv.2013.09.036.
- [42] L.M. Miller, E. Halvorsen, T. Dong, P.K. Wright, Modeling and experimental verification of low-frequency MEMS energy harvesting from ambient vibrations, *J. Micromechanics Microengineering*. 21 (2011) 45029. doi:10.1088/0960-1317/21/4/045029.
- [43] W.J. Pierson, L. Moskowitz, A proposed spectral form for fully developed wind seas based on the similarity theory of S. A. Kitaigorodskii, *J. Geophys. Res.* 69 (1964) 5181–5190.  
doi:10.1029/JZ069i024p05181.
- [44] E. Sarrouy, *Analyse globale de systemes mecaniques non lineaires. Application a la dynamique des rotors*, Ecole Centrale Lyon, (2008).
- [45] B.B. Ali H. Nayfeh, *Applied Nonlinear Dynamics: Analytical, Computational, and Experimental Methods*, 1995. doi:10.1002/9783527617548.
- [46] D.O. David A Cox, John Little, *Ideals, Varieties, and Algorithms: An Introduction to Computational Algebraic Geometry and Commutative Algebra*, Springer, New York, (2010).
- [47] F. Rouillier, Solving Zero-Dimensional Systems Through the Rational Univariate Representation, *Appl. Algebr. Eng. Commun. Comput.* 9 (1999) 433–461.  
doi:https://doi.org/10.1007/s002000050114.
- [48] H.J. Möller, H.M., Stetter, Multivariate polynomial equations with multiple zeros solved by matrix eigenproblems, *Numer. Math.* 70 (1995) 311–329. doi:10.1007/s002110050122.
- [49] L. Simeone, M.G. Tehrani, S.J. Elliott, M. Hendijanizadeh, Nonlinear damping in an energy harvesting device, in: *Proceedings of the International Conference on Noise and Vibration Engineering (ISMA)*, Leuven (2014).
- [50] M.A. Karami, D.J. Inman, Equivalent damping and frequency change for linear and nonlinear hybrid vibrational energy harvesting systems, *J. Sound Vib.* 330 (2011) 5583–5597. doi:10.1016/j.jsv.2011.06.021.
- [51] J.M. Jan A. Sanders, Ferdinand Verhulst, *Averaging Methods in Nonlinear Dynamical Systems*, (2007).

- [52] K. Worden, G.R. Tomlinson, *Nonlinearity in Structural Dynamics*, IOP Publishing Ltd, (2001). doi:10.1887/0750303565.
- [53] I. The MathWorks, roots, (n.d.).
- [54] I. The MathWorks, ode45, (n.d.).
- [55] P.L. Green, M. Hendijanizadeh, L. Simeone, S.J. Elliott, Probabilistic modelling of a rotational energy harvester, 27 (2016) 528–536. doi:10.1177/1045389X15573343.
- [56] M.G. Tehrani, S.J. Elliott, Inverse design of nonlinearity in energy harvesters for optimum damping, in: RASD (2016), Southampton.
- [57] A.G. Thompson, C.E.M. Pearce, An Optimal Suspension for an Automobile on a Random Road, (1979). doi:10.4271/790478.
- [58] B. Mohraz, A study of earthquake response spectra for different geological conditions by bijan mohraz, 66 (1976) 915–935.
- [59] T. Lafont, N. Totaro, A.L. Bot, Review of statistical energy analysis hypotheses in vibroacoustics, *Proc. R. Soc. A Math. Phys. Eng. Sci.* 470 (2014). doi:10.1098/rspa.2013.0515.
- [60] R.N. Iyengar, P.K. Dash, Study of the Random Vibration of Nonlinear Systems by the Gaussian Closure Technique, *J. Appl. Mech.* 45 (1978) 393. doi:10.1115/1.3424308.
- [61] T.K. Caughey, Equivalent Linearization Techniques, *J. Acoust. Soc. Am.* 34 (1962) 2001. doi:10.1121/1.1937120.
- [62] R.A. Ibrahim, A. Soundararajan, H. Heo, Stochastic Response of Nonlinear Dynamic Systems Based on a Non-Gaussian Closure, *J. Appl. Mech.* 52 (1985) 965. doi:10.1115/1.3169176.
- [63] M.N. Noori, A. Saffar, H. Davoodi, A comparison between non-gaussian closure and statistical linearization techniques for random vibration of a nonlinear oscillator, *Comput. Struct.* 26 (1987) 925–931. doi:10.1016/0045-7949(87)90109-X.
- [64] T.K. Caughey, Derivation and Application of the Fokker-Planck Equation to Discrete Nonlinear Dynamic Systems Subjected to White Random Excitation, *J. Acoust. Soc. Am.* 35 (1963) 1683. doi:10.1121/1.1918788.
- [65] A. Jahedi, G. Ahmadi, Application of Wiener-Hermite Expansion to Nonstationary Random Vibration of a Duffing Oscillator, *J. Appl. Mech.* 50 (1983) 436. doi:10.1115/1.3167056.
- [66] N.N.B. Nikolai Mitrofanovich Krylov, *Introduction to non-linear mechanis*, Princeton

university press, Princeton, (1949).

- [67] R.C. Booton, Nonlinear control systems with random inputs, IRE Trans. Circuit Theory. 1 (1954) 9–18. doi:10.1109/TCT.1954.6373354.
- [68] S.J. Elliott, G.M. Tehrani, R.S. Langley, Nonlinear damping and quasi-linear modelling, Philos. Trans. R. Soc. A Math. , Phys. Eng. Sci. 373 (2015) 1–22. doi:10.1098/not.
- [69] F. Rüdinger, S. Krenk, Spectral density of an oscillator with power law damping excited by white noise, J. Sound Vib. 261 (2003) 365–371. doi:10.1016/S0022-460X(02)01183-5.
- [70] S. Krenk, J.B. Roberts, Local Similarity in Non-linear Random Vibration, 66 (1999) 225–235. doi:10.1115/1.2789151.
- [71] S.M. A. Fasana, Meccanica delle vibrazioni, Clut, Torino, (2006).
- [72] C. Aime, Transfer Function, 64 (1974) 1129–1132.
- [73] E.S. Simeone, L. Ghandchi Tehrani M., Design of an electromagnetic-transducer energy harvester, in: RASD, Southampton, (2016).
- [74] C.M.C.G. Fernandes, P.M.T. Marques, R.C. Martins, J.H.O. Seabra, Gearbox power loss . Part II : Friction losses in gears, Tribology Int. 88 (2015) 309–316. doi:10.1016/j.triboint.2014.12.004.
- [75] T. Sakai, T., Doi, Y., Yamamoto, K., Ogasawara, Theoretical and Experimental Analysis of Rattling Noise of Automotive Gearbox, (1981). doi:10.4271/810773.
- [76] Harold Carlson, Spring Designer's Handbook, Marcel Dekker Inc, New York, (1978).
- [77] L. Simeone, M.G. Tehrani, S.J. Elliott, Maximization of the power harvested via variable shunt load in a constrained energy harvesting device, in: Proceedings of the International Conference on Noise and Vibration Engineering (ISMA), Leuven (2016).
- [78] P. Green, M. Hendijanizadeh, L. Simeone, S. Elliott, Probabilistic modelling of a rotational energy harvester, J. Intell. Mater. Syst. Struct. (2015) 1045389X15573343-. doi:10.1177/1045389X15573343.
- [79] E.S. Simeone, L. Ghandchi Tehrani M., Energy Harvesting using Nonlinear Damping, in: ENOC Conf., Wien, (2014).
- [80] TK Caughey, Response of Nonlinear Systems to Random Excitation, (1953).

